Universität der Bundeswehr München
Fakultät für Luft- und Raumfahrttechnik
Institut für Strömungsmechanik und Aerodynamik

Development and assessment of volumetric particle tracking approaches for the analysis of flows in confined geometries

Dipl.-Ing. Thomas Fuchs

Vollständiger Abdruck der bei der
Fakultät für Luft- und Raumfahrttechnik
der Universität der Bundeswehr München
zur Erlangung des akademischen Grades eines

Doktors der Ingenieurwissenschaften (Dr.-Ing.)

genehmigten Dissertation

Vorsitzender: Prof. Dr. rer. nat. Michael Pfitzner
1. Berichterstatter: Prof. Dr. rer. nat. Christian J. Kähler
2. Berichterstatter: Prof. Dr. Fulvio Scarano

Diese Dissertation wurde am 19.09.2018 bei der Universität der Bundeswehr München, 85577 Neubiberg eingereicht und durch die Fakultät für Luft- und Raumfahrttechnik am 07.03.2018 angenommen.

Tag der Prüfung: 17.04.2018

ACKNOWLEGMENTS

There are too many people I would like to say thank you for their contribution to this work. Thus, the following list of people is certainly not complete which I apologize for. First of all, I would like to thank Christian Kähler for giving me the opportunity to work on my thesis project at his institute. With the excellent equipment and the supportive environment it was a pleasure to pursue the project goals. Furthermore, I would like to thank Fulvio Scarano for reviewing this thesis. His contribution to the field of particle imaging is exceptional and therefore I am honored for his effort he put in the evaluation.

I always enjoyed going to work and that is to a great part the merit of my coworkers. We had a great atmosphere and whenever it was necessary there was a helping hand. Special thanks go to Rainer Hain, since he solved all kinds of problems for me and could help me out when I did not know how to go on. His contribution to the success of my thesis cannot be overestimated.

Finally, I want to thank my family, my son, my wife, and my parents, for showing me that work is not the most important thing in life. They helped me to put problems into perspective and also to overcome frustrating situations when something did not work out as it should have.

TABLE OF CONTENTS

Page

LIST OF FIGURES vii
SYMBOLS xi
ABSTRACT / KURZFASSUNG 1
1 Introduction 3
1.1 Motivation and background 3
1.1.1 Out of focus particle imaging 3
1.1.2 Holographic imaging 9
1.1.3 Tomographic imaging 9
1.1.4 3D-PTV and Shake-The-Box 11
1.2 Thesis outline 12
2 Single camera techniques 15
2.1 Astigmatism PTV 15
2.1.1 Particle image formation 16
2.1.2 Image preprocessing 19
2.1.3 Particle image geometry determination 19
2.1.4 Calibration and particle location determination 21
2.1.5 Measurement uncertainty 25
2.2 *In situ* calibrated defocusing PTV for wall-bounded measurement volumes 28
2.2.1 Image preprocessing 29
2.2.2 Particle image diameter determination 29
2.2.3 *In situ* calibration and particle location determination 31
2.2.4 Benchmark measurement: Tomographic PTV 34
2.2.5 Measurement uncertainty 37
2.3 Concluding remarks 45
3 Multi-camera techniques 47
3.1 Stereoscopic 3D-PTV 48
3.1.1 Calibration and particle location determination 48
3.1.2 Measurement uncertainty 50
3.2 Measurement of Tesla turbine rotor flow 55
3.2.1 Experimental set-up 56
3.2.2 Non-intrusive calibration 57
3.2.3 Flow field 62
3.3 Astigmatic 3D-PTV 63
3.3.1 Principle 63
3.3.2 Calibration and particle location determination 65
3.3.3 Measurement uncertainty 67
3.4 3D-PTV using a tomographic predictor 68

3.4.1 Principle 70
3.4.2 Synthetic data set 71
3.5 Measurement of turbulent boundary layer flow 74
3.5.1 Experimental set-up 74
3.5.2 Flow fields – comparison between time-resolved and double-frame tracking 75
3.6 Concluding remarks 76
4 Conclusion and Outlook 79
LIST OF REFERENCES 83

LIST OF FIGURES

Figure Page

1.1 (top) Defocusing imaging concept. (bottom) Astigmatic imaging concept, where cylindrical optics are introduced into the optical path (figures adopted from Segura (2015)). . . . 5
1.2 Particle image intensity distribution depending on the location of the particle relative to the focal plane. At the same absolute distance ($z_1 = |z_2|$) from the focal plane, the particle images have the same diameter of the first diffraction ring. . . . 6
1.3 Signal to noise ratio (SNR) and the measurement depth for defocusing imaging (left) and astigmatic imaging (right). . . . 7
1.4 3D-PTV principle . . . 13

2.1 Intensity coded pinhole/particle images in the central plane. Note that the intensity is inverted and that the intensity scaling differs between the images. Particle/pinhole images show an asteroid shaped diffraction pattern, a high SNR provided. . . . 17
2.2 Intensity coded pinhole/particle images in the focal plane and well beyond. Note that the intensity is inverted and that the intensity scaling differs between the images. Near the focal planes, the particle images form thin lines. Beyond the focal planes, the axis lengths increase in both directions. . . . 18
2.3 Overview of the image preprocessing steps . . . 20
2.4 Principle of APTV particle image edge location determination . . . 21
2.5 Intensity inverted grey-scale image of a pinhole matrix section with known distances, Δx and Δy, between the pinholes . . . 22
2.6 Macroscopic APTV calibration principle: First, the axis ratio values are fitted with surface splines at every z location. Second, a calibration curve for the $\boldsymbol{X} = (X, Y)$ sensor location of a pinhole image is established, using a line spline fit, where the z location is denoted by the axis ratio, a_X/a_Y, of the particle image. . . . 23
2.7 Calibration function for a specific $\boldsymbol{X} = (X, Y)$ sensor location. Both the minimum and maximum values of the axis ratio, a_X/a_Y, denote focal planes. The focal plane distance is $\Delta z_{\mathrm{fp}} \approx 25$ mm. . . . 24
2.8 Principle of uncertainty estimation . . . 26
2.9 Particle z location uncertainty . . . 27
2.10 Intensity inverted, color-coded grey scale image of astigmatic particle images as seen in the "motionless" flow analysis . . . 27
2.11 Defocused particle images and their approximated z locations in a channel with a depth of 1 mm . . . 30

2.12 Defocusing PTV particle image edge determination scheme 31
2.13 Peak locking analysis for using the maximum intensity as the particle image edge (a) and with an adaptive intensity threshold (b) 32
2.14 Working principle of the adaptive threshold for the particle image edge location determination: the solid lines denote the thin-plate spline fit and the adaptive threshold SNR with and without adaptive threshold. 33
2.15 Particle image diameter over z 34
2.16 Particle image diameter over displacement 35
2.17 Wall particle image diameter determination 35
2.18 Wall particle image diameter surface fit 36
2.19 Overview of *in situ* calibration steps 36
2.20 Flow experiment for the measurement uncertainty determination: two parallel glass plates with a distance of 1 mm. 38
2.21 Defocusing PTV set-up 39
2.22 Tomographic PTV set-up 39
2.23 Measured velocity profiles in a 2×2×1 mm^3 section of the measurement volume for defocusing PTV (a) and tomographic PTV (b) 41
2.24 Intensity distributions of cuts through three defocused particle images with different diameters 42
2.25 Measurement uncertainty of the main flow velocity u, in x direction 44
2.26 For a planar Poiseuille flow the velocities in y and z direction are supposed to be zero. Thus, the standard deviations of the measured displacements in these directions provide a measure for the displacement uncertainty. 45

3.1 Stereoscopic 3D-PTV set-up 51
3.2 Measured velocity profiles in a 2×2×1 mm^3 section of the measurement volume using 3D-PTV. 52
3.3 Measurement uncertainty of the main flow velocity u in x direction 54
3.4 For a planar Poiseuille flow the velocities in y and z direction are supposed to be zero. Thus, the standard deviations of the measured displacements in these directions provide a measure for the respective displacement uncertainty. 56
3.5 Experimental set-up of Tesla turbine rotor flow measurements 58
3.6 Test rig for flow field measurements in a Tesla rotor 59
3.7 Non-intrusive calibration principle 60
3.8 Non-intrusive calibration target 61
3.9 Residual of calibration fit error for camera 1, (left) plane z_0 = 0 mm, (right) plane z_1 = 1 mm 62
3.10 Radial velocity distribution at the radius r = 52.125±0.125 mm. 64
3.11 standard deviation of the displacement in z direction 64
3.12 Sketch of the qualitative accuracy improvement of the particle z location estimation using astigmatic 3D-PTV compared to single camera APTV. At β = 90°, the uncertainty is equal for x and z. 65

3.13 From the sensor locations $\boldsymbol{X}_1 = (X_1, Y_1)$ and $\boldsymbol{X}_2 = (X_2, Y_2)$ of the corresponding particle images, the particle locations, $\boldsymbol{x} = (x, y, z)$, are determined using third order polynomial mapping functions (capital letters denote image/sensor coordinates; lowercase letters denote physical coordinates). 66
3.14 Particle location scheme using stereoscopic APTV. Single camera APTV gives an initial estimate of the particle locations for both cameras. Thus, particle images are matched using the location information with a search radius in space. Particles are then located more accurately employing the stereoscopic view. 67
3.15 Error of the pinhole location reconstruction calculated at every pinhole matrix z position. For the y coordinate the location error is the lowest, while the z uncertainty is the highest (measurement volume size: 40×40×25 mm^3). . . . 69
3.16 Principle of combined tomographic 3D-PTV. The tomographic reconstruction is used the predict the sensor locations of corresponding particle images and to detect ambiguities. Case 1 shows a unique particle image correspondence. In case 2 an ambiguity is shown, where a particle image is associated with two spatial particle coordinates. 71
3.17 The fraction of correctly estimated particle locations, i.e. they are located within one voxel radius from the true particle locations (CA = combined tomographic 3D-PTV; RF = reference data) 72
3.18 The fraction of ghost particles compared to the number of true particles (CA = combined tomographic 3D-PTV; RF = reference data) 73
3.19 Uncertainty of the spatial particle location determination 74
3.20 Effective amount of particles per pixel 75
3.21 Schematic of the experimental set-up for the turbulent boundary layer measurement 76
3.22 Mean flow velocities, binned in wall-normal direction with a bin width of 0.02 mm. Following constants are used: $\kappa = 0.41$ and $\beta = 5.0$. 77
3.23 Reynolds stresses, binned in wall-normal direction with a bin width of 0.02 mm for the combined approach (TR-PTV = time-resolved PTV; DF-PTV = double-frame PTV). 78

SYMBOLS

Superscripts

T	transposed
i, j, k	order of polynom

Subscripts

ast	astigmatism
cyl	cylindrical
fp	focal plane
i	quantity related to the camera i or the data point i
j	quantity related to the data point j
max	maximum
n	number of data points
pin	pinhole
ppp	particle per pixel
s	step
sph	spherical
τ	quantity related to Gaussian fit peak width
X, Y	quantity related to the sensor X, Y coordinate
x, y, z	quantity related to the physical x, y, z coordinate

Acronyms

2D	two-dimensional
3D	three-dimensional
3D-PTV	three-dimensional particle tracking velocimetry
APTV	astigmatism particle tracking velocimetry
CFD	computational fluid dynamics
cw	continuous wave
DEHS	Di-ethyl-hexyl-sebacate
DF-PTV	double-frame particle tracking velocimetry
DPTV	defocusing particle tracking velocimetry
FOV	field of view
LDA	laser Doppler anemometry
LOS	line of sight
MART	multiplicative algebraic reconstruction technique
MLOS	multiplicative line of sight
Nd:YAG	neodymium-doped yttrium aluminum garnet
pH	potential of hydrogen
PIV	particle image velocimetry
PTV	particle tracking velocimetry

RMS	root mean square
sCMOS	scientific complementary metal oxide semiconductor
SNR	signal to noise ratio
STB	Shake-The-Box
TR-PTV	time-resolved particle tracking velocimetry

ABSTRACT

Fuchs, Thomas. Dr. Ing, Universität der Bundeswehr München, 07.03.2018. Development and assessment of volumetric particle tracking approaches for the analysis of flows in confined geometries. Professor: Prof. Dr. rer. nat. Christian J. Kähler.

Particle-based flow visualization has long been practiced in flow diagnostics to gain insights into the fluid physics. Ludwig Prandtl's water tunnel experiments of aerofoils are well-known to this day (see Prandtl (1936) and Willert & Kompenhans (2010)). Due to their huge prospects, particle imaging methods have been subject to extensive research, in order to enhance the methods from pure qualitative diagnostics to comprehensive quantitative flow analysis tools. Today, particle imaging techniques along with numerical techniques are the key technologies for capturing three-dimensional (3D) flow fields and adjacent quantities. However, the required multi-camera set-ups are cumbersome, complex, and very costly and therefore limit the applicability. It is the purpose of this research to simplify particle-based 3D flow measurement techniques such that the range of applications can be broadened. A special attention is drawn to challenging measurement environments, with difficult optical access, vibrations, contamination, fluctuating seeding densities, and limited space for equipment.

To address the aforementioned requirements, the astigmatism particle tracking velocimetry (APTV) technique, well-established in microfluidics, was developed further, to meet the challenges of macroscopic flow measurements. The APTV method targets applications in compressor, turbine, combustion, and engine research, as well as volumetric flow velocimetry in wind tunnel facilities with high mass flow rates.

Furthermore, the three-dimensional particle tracking velocimetry (3D-PTV) approach was refined to meet the specific challenges, which occur in double-pulse systems in a stereoscopic imaging set-up. For densely seeded flows, a combined tomographic 3D-PTV processing approach is introduced targeting at the measurement of complex flow fields with strong velocity gradients, while providing a high spatial resolution without requiring a time-series of recordings.

All the mentioned measurement technique developments are based on robust processing procedures and are therefore suitable for flow velocimetry in industrial environments.

KURZFASSUNG

Strömungsvisualisierung mithilfe von Partikeln wurde seit den Anfängen der Strömungsuntersuchungen eingesetzt. Ludwig Prandtl's Profiluntersuchungen im Wasserkanal sind auch heute noch wohlbekannt (siehe Prandtl (1936) und Willert & Kompenhans (2010)). Aufgrund ihres großen Potentials wurde intensiv im Bereich der partikelbasierten Strömungsmessmethoden geforscht um diese Methoden von qualitativen Visualisierungsverfahren zu quantitativen Messverfahren weiterzuentwickeln. Heute bilden par-

tikelbasierte Strömungsmessmethoden zusammen mit numerischen Methoden die Schlüsseltechnologien zur Bestimmung drei-dimensionaler Strömungsfelder und dazugehöriger Messgrößen. Die erforderlichen Mehr-Kamera Messsysteme sind jedoch sehr komplex und kostenintensiv, wodurch die Anwendbarkeit eingeschränkt wird. Im Zuge dieser Arbeit sollen weniger komplexe volumetrische Strömungsmessmethoden weiterentwickelt werden, um den Anwendungsbereich dieser Methoden zu erweitern. Der Fokus liegt dabei vor allem auf den Einsatz der Messtechnik in schwierigen Messumgebungen mit begrenztem optischen Zugang, Vibrationen, Verschmutzung, schwankenden Seedingdichten und begrenztem Raum für die Ausrüstung.

Um diesen Herausforderungen gerecht zu werden, wurde die Astigmatismus Particle Tracking Velocimetry (APTV) Methode, welche in der Mikrofluidik schon erfolgreich eingesetzt wird, für makroskopische Anwendungen weiterentwickelt. Der Fokus der APTV Anwendungen liegt dabei auf der Verdichter-, Turbinen-, Verbrennungs- und Motorenforschung, sowie volumetrischer Strömungsmessungen in Windkanälen mit hohen Massenströmen.

Zudem wurde die 3D-PTV Messmethode auf die speziellen Gegebenheiten bei Doppel-Puls Messungen mit einer stereoskopischen Kamerakonfiguration angepasst. Für Messungen bei höheren Seedingdichten wurde eine tomographische Prädiktor Methode entwickelt, welche optische Tomographie und die 3D-PTV Methode kombiniert. Diese Methode dient zur Messung komplexer Strömungsfelder mit starken Geschwindigkeitsgradienten, bei gleichzeitig hoher räumlicher Auflösung ohne zeitliche Auflösung der Aufnahmen.

Die zuvor erwähnten Messmethodenentwicklungen basieren auf robusten Auswerteprozeduren und eignen sich daher besonders für Strömungsmessungen im industriellen Umfeld.

1 Introduction

1.1 Motivation and background

Fluid dynamics has a much stronger impact on our lives than it is immediately apparent. The availability of energy is inevitable to provide growth and wealth to an increasing number of humans. Energy efficiency is a key to meet this challenge, since it enables us to save fossil resources as well as natural resources (land etc.), which both have a finite availability and both are costly. At the same time the environmental impact of ever increasing energy consumption needs to be limited. Improved aerodynamics of gas, steam, and wind turbines, and of course also of vehicles, trains, and airplanes can contribute significantly to the protection of the environment. This list can be extended by more efficient heat transfers and chemical reactions, using improved flow control.

Particle imaging techniques contribute significantly to the technological progress. These techniques provide insights to the flow physics, which is valuable in fundamental research, such as the turbulent boundary layer research, as well as in industrial applications, for instance to improve the efficiency of a compressor stage. The validation of computational fluid dynamics (CFD) codes is another important task being handled by particle imaging techniques. Starting from single point measurement techniques such as laser Doppler anemometry (LDA), the emergence of planar particle image velocimetry (PIV) in conjunction with digital imaging and processing established particle imaging as a powerful tool in flow analysis.

Improvements of the imaging, the data storage, and the evaluation hardware, together with extensive research in the field of particle imaging, led to the appearance of 3D velocimetry techniques. Volumetric flow information can help to fully utilize potential efficiency gains by providing a comprehensive understanding of the flow physics. This applies for flows, where the scales are smaller than the typical light sheet thickness, which yields around 1 mm, of planar PIV and stereoscopic PIV. Furthermore, 3D techniques can measure larger domains more efficiently, since it is not necessary to relocate laser sheets or to refocus the cameras, as it is necessary for planar approaches. Instead, instantaneous volumetric information can be achieved. Nowadays, a variety of capable volumetric particle imaging techniques is available, as outlined in the following.

1.1.1 Out of focus particle imaging

In terms of their simplicity, robustness, and cost efficiency, 3D single camera particle imaging techniques are advantageous compared to multi-camera methods. Among the

single camera methods, defocusing and astigmatic imaging are straightforward approaches with a similar principle. Both capture out of focus particles, i.e. the particles are not located in the focal plane, to deduce their depth location along the optical axis. To find this location, defocusing simply employs the amount of particle image blurring, increasing with distance of the illuminated particle to the focal plane, as illustrated in the upper part of Fig. 1.1. A particle closer to the focal plane forms a smaller blur on the sensor, whereas a particle further away yields a larger blur.

Introducing cylindrical optics into the light path of an optical system, induces astigmatic aberrations. The astigmatism leads to elliptically shaped particle images, since a second focal plane appears (Hain & Kähler (2006) and Cierpka et al. (2010)). As illustrated in Fig. 1.1 (bottom), a particle located close to the focal plane F_{xz} has a small blur (a_X) along the sensor X coordinate, whereas the Y axis length, a_Y, appears elongated. The opposite behavior applies close to the focal plane F_{yz}: a_X is large and a_Y small. The z coordinate of a particle is deduced from the shape of the elliptical particle images. Why it is advantageous to use astigmatic imaging over defocusing is answered in a few paragraphs, after some implementations of the defocusing techniques were introduced.

Defocusing imaging

Willert & Gharib (1992) proposed a macroscopic defocusing approach using a three-pinhole aperture with an off-axis position of the pinholes. They proved the principle by investigating a vortex ring impinging on a wall. With the pinhole aperture, particle images appear as triplets on the sensor, where the separation between the triplets relates the particle location to its distance to the reference plane, i.e. the focal plane.

The approach was later adopted for the measurement of a two-phase bubbly flow by Pereira et al. (2000), while this application employed three cameras, each with a single pinhole. This was necessary due to the size of the measurement volume, requiring a large lateral displacement between the pinholes, which is not feasible using a single camera. Pereira & Gharib (2002) provided a more detailed description of the two-phase flow measurement approach. A comprehensive theoretical description of the three-pinhole defocusing principle was given by Kajitani & Dabiri (2005), extended with an improved definition of the measurement volume by Grothe & Dabiri (2008).

To resolve particle image overlaps with increasing seeding density due to imaging particles as particle image triplets, Tien et al. (2008) developed a color-coded defocusing imaging implementation. Since every image of a triplet has its specific color, it is easier to distinguish, which triplets belong together. Furthermore, their approach features a back-light volume illumination to enhance the signal to noise ratio (SNR). In defocusing applications, low SNRs, due to the out of focus imaging impaired with using a pinhole mask, are significant drawbacks of the technique, especially in large measurement volumes. The three-pinhole approach has also been applied for microscopic particle imaging by Yoon & Kim (2006), Pereira et al. (2007), and Tien et al. (2014), among others.

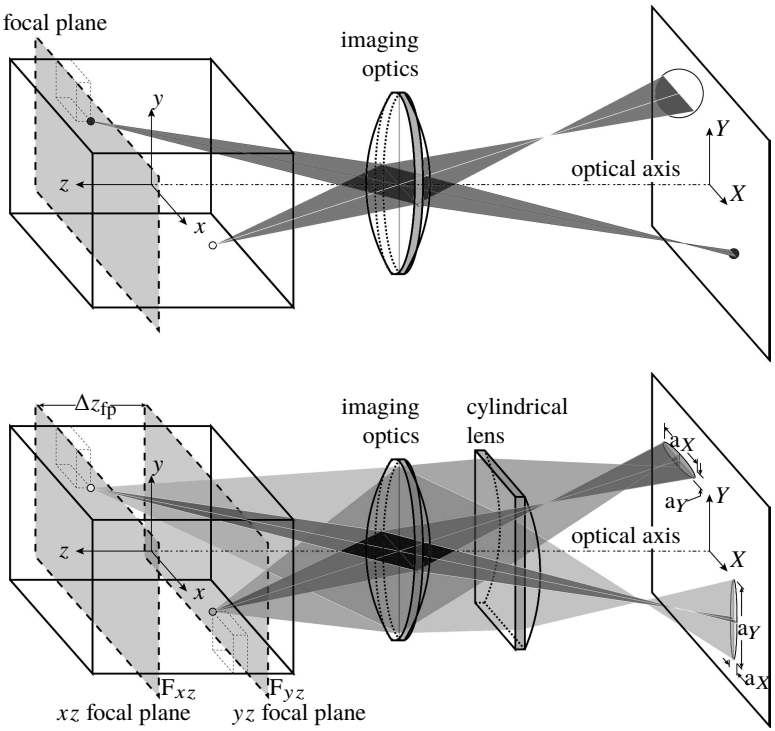

Figure 1.1: (top) Defocusing imaging concept. (bottom) Astigmatic imaging concept, where cylindrical optics are introduced into the optical path (figures adopted from Segura (2015)).

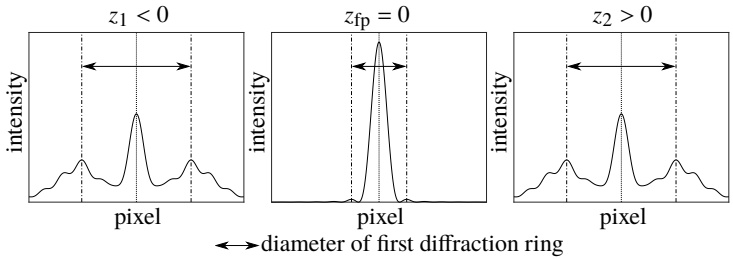

Figure 1.2: Particle image intensity distribution depending on the location of the particle relative to the focal plane. At the same absolute distance ($z_1 = |z_2|$) from the focal plane, the particle images have the same diameter of the first diffraction ring.

However, defocusing particle imaging can also be employed by simply relating the diameter of the first diffraction ring of the particle image to the particle depth location without placing a mask in front of the camera sensor as shown by Stolz & Köhler (1994) and Murata & Kawamura (1999). This works as follows: A particle imaged in the focal plane yields an intensity distribution on the sensor being referred to as Airy disk. Figure 1.2 (center) shows this distribution, where a distinct peak is visible and also the first diffraction ring, denoted by a slight increase of the intensity away from the image center. Normally, this first diffraction ring of an in focus particle is not visible on the sensor, since its intensity is not sufficiently high. Furthermore, the sensor pixel sizes are too large to resolve this pattern, such that a Gaussian intensity distribution is a more suitable model for the particle images. However, if a particle is imaged further away from the focal plane, the first diffraction ring becomes more distinct, as shown in Fig. 1.2 (left), allowing for the use of the particle image diameter to determine particle depth location. Moreover, the optical system in a defocusing set-up is symmetric along the optical axis with respect to the focal plane. Thus, a particle image has the same appearance if it is imaged at the same distance from the focal plane nearer or closer to the camera sensor (compare Figs. 1.2 (left) and (right)).

The diffraction ring approach has less problems with low SNRs and is capable of measuring macroscopic flows in domains with measurement depths in the millimeter range, as outlined by Fuchs et al. (2016d). The latter approach can also be combined with an *in situ* calibration procedure, as introduced by Fuchs et al. (2016c). Lin et al. (2008) introduced an annular aperture that can be used to establish doughnut-like particle images in order to improve the processing of overlapping particle images.

However, the defocusing approach has some drawbacks, limiting its applicability. One is that the region close to focal plane cannot be used to measure the particle depth location, since the first diffraction cannot be resolved anymore. This comes along with the fact

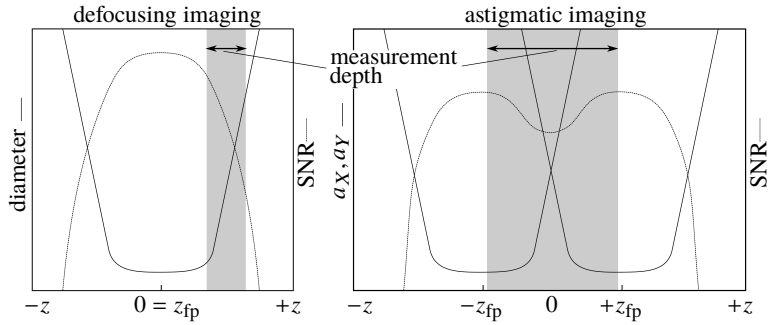

Figure 1.3: Signal to noise ratio (SNR) and the measurement depth for defocusing imaging (left) and astigmatic imaging (right).

that the change of the diameter over z is too small close to the focal plane, as illustrated qualitatively in Fig. 1.3 (left). Thus, the region with a high SNR cannot be employed for the measurements. Another drawback is that the measurement volume can only be located on either side of the focal plane, since the focal plane region cannot be used as outlined before. Furthermore, due to the symmetry of the imaging system it is not possible to tell if a particle is located at a certain distance nearer or further away relative to the focal plane. The particle images have the same diameter. Altogether, the measurement depth of a defocusing system is strongly limited, as indicated by the grey area in Fig. 1.3 (left).

Astigmatic imaging

Unlike defocusing, astigmatic imaging offers a very homogenous distribution of the SNR along the measurement volume depth, as shown qualitatively in Fig. 1.3 and outlined in Cierpka & Kähler (2012). Close to the focal planes, where either axis length of the elliptical particle image has its minimum, the SNR has the highest values. The SNR decreases towards the center between the focal planes, while still having a similar magnitude compared to the two focal plane regions. Due to the homogenous SNR distribution, the particle location determination uncertainty is similar along the measurement depth. This is due to the fact that the location uncertainty is significantly influenced by the SNR, since the particle image axis lengths a_X and a_Y can be determined with higher accuracy, if the particle image appears more distinct with respect to the background.

For several reasons astigmatic imaging offers a larger measurement volume depth than defocusing, simply by introducing a cylindrical lens in the light path. First, the areas close to the focal planes can be employed for the measurement. While one of the axis lengths is changing only slightly over z in that region, the other axis length function has a large slope. Thus, the geometry change of the elliptical particle image is still significant enough

to allow for an accurate particle depth location determination.

Additionally, the cylindrical lens breaks the symmetry of the optical system. Using defocusing, it is not possible to measure particle depth locations on both sides of the focal planes, since the diameter only depends on the distance from the focal plane, not on which side the particle is located. With the appearance of a second focal plane, the entire z range between the focal planes can be employed for the measurement, since the z location of the particle is coded in the unique shape of the elliptical particle image, its axis lengths a_X and a_Y.

The increase of the measurement depth is certainly the biggest advantage of astigmatic over defocusing imaging. Furthermore, the focal plane distance and therefore the measurement depth can be adjusted by the amount of astigmatism introduced in the optical system. This amount is actually denoted by the deviation of the wave front shape to the ideal spherical wave front. A cylindrical lens with a smaller focal length leads to stronger deviations from the ideal spherical wave front, resulting in a larger focal plane distance. However, instead of replacing the lens, it is feasible to move the position of the cylindrical lens (fixed focal length) along the optical light path. The closer the lens is placed to the volume, the less the wave front is distorted and the smaller the focal plane distance. The advantage of the latter set-up is that the focal plane distance can be adjusted continuously.

Today, APTV is well-established in microfluidics, where it was first introduced by Kao & Verkman (1994) to track single fluorescent particles in artificial solutions and living cells. In this first application of APTV, a very small volume depth of 12 µm was measured. The particle image axis lengths were determined by the derivative of the intensity along the horizontal and the vertical sensor coordinate of the particle image. For the calibration, a relation between the ratio of the horizontal and vertical particle image axis lengths and the respective particle z location was established. Since the achievable measurement depth was rather small, it was necessary to move the microscope stage along the optical access according to the movement of the particle. This procedure allowed for the tracking of single particles through a larger volume.

Other applications in microfluidics include a backward-facing step flow measurement by Chen et al. (2009); the analysis of an electrothermal microvortex by Kumar et al. (2010); tracking of nanoparticles inside living tissue by Spille et al. (2012); the vortex structure analysis of electroosmotic flows by Liu et al. (2013); the investigation of evaporating droplets by Marin et al. (2015); the volumetric motion analysis of particle under ultrasound-induced acoustophoresis by Muller et al. (2013); a steady streaming vortex flow from microbubbles investigation by Rallabandi et al. (2015); and also multi-physics measurements with a combined flow velocity and temperature estimation using thermo liquid crystals by Segura et al. (2015).

APTV has not been applied as extensively for macroscopic domains, since some additional challenges occur. However, Buchmann et al. (2014) proved the feasibility of APTV for the macroscopic measurement of particle-laden supersonic impinging jets.

1.1.2 Holographic imaging

Holography is an intriguing imaging concept, allowing for accurate volumetric flow velocity measurements. The hologram, an interference pattern containing the amplitude and the phase information of light, is recorded on a photographic plate by superimposing the object wave with a coherent reference wave (Pu et al. (2000)). Later, the spatial particle distribution can be reconstructed by illuminating the hologram with a replica of the reference beam, where Pu & Meng (2000) retrieved 92000 particle pairs. Naturally, the photographic approach is rather cumbersome and time consuming and therefore strongly limits the applicability of holography for particle imaging (Barnhart et al. (1994) and Katz & Sheng (2010)).

In practice, it is advantageous to directly record the holograms on a digital camera, as outlined by Schnars & Jüptner (1994) and Meng et al. (2004). However, the available imaging hardware is the limiting factor of the digital approach. The current relatively large pixel sizes of the camera sensors does not allow for imaging the small tracer particles by means of the favourable off-axis holographic imaging set-up, as outlined by Hinsch (2002). Furthermore, the resolution of photographic plates exceeds that of a sensor by far, such that it is rather challenging to resolve the spatial frequencies of the imaged particles digitally.

Nowadays, holographic particle imaging has significant disadvantages compared with other 3D flow measurement techniques. Therefore, it is seldom applied for flow measurements. Nevertheless, in future, holography has the potential to become a powerful measurement method with the availability of more sophisticated imaging hardware. Altogether, single camera techniques offer some unique capabilities, opening new fields of application for 3D flow velocimetry.

1.1.3 Tomographic imaging

Multi-camera techniques have the ability to measure the three velocity components in three dimensions (3D3C measurements) with similar accuracy, if the angles between the cameras are larger than 60°. This ability is attributed to the fact that the measurement volume is imaged from multiple views, whereas single camera, or more precisely, single view approaches yield significantly higher uncertainties in depth direction, i.e. along the optical axis.

The tomographic PIV method, introduced by Elsinga et al. (2006), is a capable velocimetry technique. Optical tomography is used to reconstruct the seeded measurement volume, yielding a spatial intensity distribution, discretized on a voxel grid. So far the multiplicative algebraic reconstruction technique (MART), proposed by Herman & Lent (1976), is the most common volumetric reconstruction technique. Another common reconstruction approach is the multiplicative line of sight (MLOS) reconstruction, which is much faster but less accurate, yielding more reconstruction ambiguities. Following the volume reconstruction, the velocity field is determined by means of a 3D cross-correlation

of the reconstructed voxel space.

The coordinate mapping, from physical to image space, can be performed by means of third-order polynomials, as applied by Soloff et al. (1997) and Willert (1997) for stereoscopic PIV. Tsai (1987) introduced the so-called camera-pinhole model, which is feasible for calibrating the optical system. Tomographic imaging systems are very sensitive towards misalignments of the cameras, which can occur due to vibrations, for instance. Therefore, the reconstruction quality is improved significantly or even only possible, if applying a self-calibration to the recordings. Wieneke (2008) developed a self-calibration procedure for volumetric measurements.

More recently, Schanz et al. (2013) introduced tomographic reconstruction enhancements by means of non-linear optical transfer functions, accounting for optical aberrations. Other improvements focused on the reduction of the fraction of ghost particles, such as the motion tracking enhanced (MTE) MART reconstruction by Novara et al. (2010) and Novara & Scarano (2012).

Tomographic PIV has been applied extensively for the analysis of complex flows. Hain et al. (2008) investigated the flow around a finite cylinder mounted on a flat plate and compared the tomographic PIV results with time-resolved PIV results. Buchmann et al. (2011) analyzed the flow through a modeled human carotid artery bifurcation. A large-scale flow was measured by Kühn et al. (2010), using helium-filled soap bubbles as tracer particles in a 750×450×165 mm^3 sized measurement volume. Klinner & Willert (2012) employed tomographic reconstruction to determine a volumetric spray distribution.

The feasibility of time-resolved tomographic PIV measurements is reported by Schröder et al. (2007) and Schröder et al. (2011). Lynch & Scarano (2013) introduced a processing approach, yielding an improved dynamic range and better accuracy using continuum deformation. Furthermore, the MTE-MART approach was refined for time-resolved data by Lynch & Scarano (2015), yielding an improved computational efficiency.

However, the appearance of ghost particles, defined as intensity peaks, which are not corresponding to a real particle, can alter the estimated flow field significantly using tomographic PIV (Atkinson et al. (2010)). These intensity peaks appear, if non-corresponding lines of sight intersect in the volume. A comprehensive description on the formation of ghost particles can be found in Elsinga et al. (2011).

Spatial averaging, due to the cross-correlation, limits the applicability of tomographic PIV for resolving strong velocity gradients, as shown by Elsinga et al. (2011). To improve the spatial resolution, tomographic reconstruction can be used to determine the spatial intensity distribution of the particles. Instead of cross-correlating the data, the individual particles locations can be determined with sub-voxel accuracy by means of a 3D Gaussian fit, for instance. A tracking algorithm is then applied to retrieve the velocity data. This paradigm was used by Schröder et al. (2011) to measure a turbulent boundary layer flow. Using this approach, the theoretical achievable particle image density lies in the range of $N_{\mathrm{ppp}} = 0.03 - 0.05$, as shown by Elsinga & Tokgoz (2014).

1.1.4 3D-PTV and Shake-The-Box

In three-dimensional particle tracking velocimetry (3D-PTV), the spatial particle locations are triangulated using two or more corresponding particle images from different views of the measurement volume (Sheu et al. (1982), Maas et al. (1993)). This principle is illustrated in Fig. 1.4(a), where $\boldsymbol{x}$ denotes the spatial particle location and $\boldsymbol{X}_1$ and $\boldsymbol{X}_2$ the sensor coordinates of the corresponding particles images. Triangulation in the 3D-PTV context means that particle location $\boldsymbol{x}$ represents the intersection of the lines of sight (LOS) of the two particle images in space. However, since uncertainties arise in the determination of the particle image sensor coordinates and in the calibration function due to optical aberrations and other distortions, the LOS do not actually intersect. Thus, the particle location $\boldsymbol{x}$ is situated halfway between the shortest Euclidean distance of the LOS. Unlike in tomography, the particle locations are not stored in terms of a reconstructed intensity distribution on a voxel grid. Instead, only the three spatial coordinates of a particle need to be stored, requiring much less storage space compared to the voxel grid. Employing the spatial particle coordinates, the flow velocities can be estimated by tracking the individual particle between two or more time steps.

Prior to the triangulation, the corresponding particle images need to be determined. To do that, originating from a particle image on sensor #1, located at $\boldsymbol{X}_1 = (X_1, Y_1)$, the epipolar line, denoting a projection of a LOS of a certain sensor coordinate on another sensor, on sensor #2 is calculated, where the length of the search area depends on the measurement depth d_z (see Fig. 1.4(a)). Possible particle image matches are searched for in the proximity of the epipolar line, while the maximum distance to the line is restricted by a preset search width, as illustrated in Fig. 1.4(b).

However, at increasing seeding concentrations it is difficult to find corresponding particle images on the different sensors, since ambiguities in the matching arise. It is obvious that with more particle images in the search area it might not be clear, which is the corresponding one. Furthermore, larger measurement depths, $d_{z_2} > d_{z_1}$, yield a larger search area and therefore more possible matches even at a constant particle image density, as indicated by the dashed extension of the epipolar line in Figs. 1.4(a) and 1.4(b). Ambiguities are also present in tomographic imaging systems, where they are referred to as ghost particles. In general, increasing the number of cameras helps to resolve these ambiguities, while this is only possible to a certain extent. A time-series of recordings is another way to provide further information to solve the ambiguities using the particle trajectories (Malik et al. (1993)). Applications of time-resolved 3D-PTV include the investigation of a wake flow behind a cylinder by Kieft et al. (2002), an impinging jet by Hwang et al. (2005), and a flow with quasi-homogeneous isotropic turbulence by Lüthi et al. (2005).

To date, the research activities in 3D-PTV were marginal compared with tomographic PIV. However, only recently, due to its unique capabilities, 3D-PTV gained increasing interest from the tomographic PIV community, resulting in a new iterative reconstruction technique, introduced by Wieneke (2013). In particular, approaches combining 3D-PTV and tomographic reconstruction are of interest, since the advantages of both techniques,

i.e. high seeding densities impaired with Lagrangian properties, can be utilized, as outlined by Novara & Scarano (2013). For near-wall flow measurements, or generally in the presence of strong velocity gradients, the use of particle tracking is advantageous over cross-correlation methods, where the correlation windows limit the spatial resolution, as analyzed by Kähler et al. (2012a) and Kähler et al. (2012b).

Schanz et al. (2016) introduced a powerful time-resolved 3D-PTV approach, the so-called "Shake-The-Box" (STB) approach, allowing for large seeding concentrations. This triangulation approach is strongly iterative and uses multiple time steps, in order to avoid the reconstruction of ghost particles. In the experimental case, an open jet water flow with particle image densities in the range of $N_{ppp} \approx 0.035$, was measured. Furthermore, STB was applied to measure the flow over periodic hills by Schröder et al. (2015). However, the requirement of a time-series of recordings strictly limits the applicability of the STB method to rather low flow velocities and low magnification, except for the use of a four-pulse STB scheme, as proposed by Novara et al. (2016). The multi-pulse scheme, however, cannot reach the performance of the time-resolved STB scheme in terms of accuracy and seeding density. Furthermore, the mapping of the two tomographic imaging systems to a single coordinate system is very difficult and introduces errors. In addition to that, each multi-frame recording requires a tomographic PIV processing step to get an initial displacement field prediction.

The requirement of a time-series of recordings is a major drawback for applied aerodynamics. Furthermore, the experimental set-up is rather costly due to the sophisticated hardware. Therefore, the research presented in this thesis focuses on the analysis of double-frame recordings, where sophisticated tracking approaches, as introduced by Cierpka et al. (2013), help to determine the flow field.

1.2 Thesis outline

The purpose of this thesis is the development of volumetric measurement techniques for applications, where particle imaging techniques have not been used for flow velocimetry, due to specific challenges, including limited optical access and vibrations, for instance. However, the use of a particular velocimetry method also depends on the required accuracies, costs, measurement time, and hardware availability, to name a few. Therefore, this thesis outlines volumetric flow velocimetry techniques, ranging from single camera approaches for designated purposes, such as measurement environments with strong vibrations along with the measurement in domains with small depths dimensions, with strong velocity gradients in depth direction, which need to be resolved, to multi-camera methods. These more complex multi-camera techniques provide a higher accuracy in the particle depth location determination and due to higher seeding densities also an increased spatial resolution, to capture instantaneous flow structures.

First, the single camera techniques are introduced in chapter 2. The focus lies on the

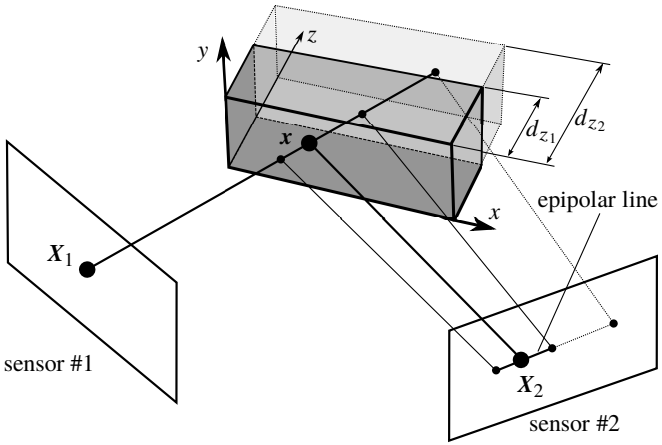

(a) Triangulation principle

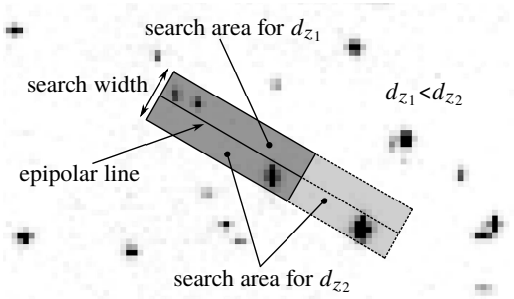

(b) Search area for corresponding particle images on the second sensor

Figure 1.4: 3D-PTV principle

astigmatism particle tracking velocimetry approach, which is described comprehensively in section 2.1. This includes a description of the appearance of the particle images, where theoretical models are compared to experimental images. Furthermore, the imaging set-up is described in detail, along with the calibration procedure, the image processing procedures, and a quantitative measurement uncertainty analysis. An *in situ* calibrated defocusing PTV (DPTV) measurement approach is outlined and compared to a tomographic PTV approach in terms of its performance in section 2.2.

While the single camera approaches are very capable velocimetry approaches for specific applications, multi-camera techniques offer advantages, if a more accurate measurement of the velocity z component and a better spatial resolution in z direction is required, as outlined in chapter 3. For keeping the complexity as low as possible and to minimize the required optical access, a 3D-PTV approach is introduced in section 3.1, employing only two cameras. This stereoscopic 3D-PTV approach allows for highly accurate flow measurements at relatively low seeding densities, to avoid ambiguous particle image matching. The stereoscopic 3D-PTV approach was applied for the measurement of a Tesla turbine rotor flow, as introduced in section 3.2. For this measurement, a non-intrusive calibration approach was employed, outlined subsection 3.2.2. Furthermore, a combined APTV and stereoscopic 3D-PTV scheme is outlined in section 3.3, which uses astigmatic imaging as a predictor, to avoid ambiguous particle image matching.

To fully capture all flow scales of complex flows, such as turbulent boundary layer flows, it is desirable to increase the seeding density as much as possible, to enhance the spatial resolution. Therefore, it is also necessary to employ a particle tracking approach to resolve strong velocity gradients without the spatial averaging of cross-correlation approaches. The greatest challenge for these kind of measurements is the correct matching of corresponding particle images on the different camera sensors. A time-series of recordings can help to perform this matching with the spatio-temporal information.

However, for applications in aerodynamics, it is usually not possible to conduct time-resolved measurements, due to hardware constraints. Therefore, it is the object of the combined tomographic and 3D-PTV approach presented in section 3.4, to provide a measurement scheme, allowing for high seeding densities for double-frame imaging. Here, tomographic reconstruction is used as a predictor to match the particle images on the different camera sensors. This tomographic 3D-PTV approach is assessed by analyzing a synthetic data set and a turbulent boundary layer flow.

2 Single camera techniques

There is considerable interest to employ single camera flow measurement techniques and their unique capabilities for the measurement of macroscopic flows. They have significant advantages over multi-camera approaches due to the nature of their simple and robust set-up. Since only a single camera is required for volumetric flow velocimetry, these techniques are best suited for applications with limited optical access. Furthermore, when vibrations are present, single camera approaches are much less affected by camera misalignments. For compressor, turbine, combustion, and engine research, the insensitivity to vibrations is a crucial feature. Moreover, in the latter applications it is difficult to provide a sufficient and homogeneous amount of seeding. Since single camera approaches work better at low seeding concentrations, where also the contamination of the test facilities is minimized, these techniques are well suited in such case. Furthermore, in industrial applications the knowledge of the mean velocity field is sufficient, favoring the use of a less complex measurement technique.

In the first part of this chapter, in section 2.1, the astigmatism particle tracking velocimetry (APTV) method for macroscopic applications is described in detail. A theoretical and experimental image formation study is presented. Furthermore, the particle image geometry determination as well as the calibration procedure are outlined. Parts of section 2.1 were published in Fuchs et al. (2013), Fuchs et al. (2014a), Fuchs et al. (2014b), and Fuchs et al. (2014c). Figures and text are adjusted to fit the format of this thesis and to improve readability.

The second part of this chapter, section 2.2, introduces an *in situ* calibrated defocusing particle tracking velocimetry (defocusing PTV) approach for wall-bounded measurement volumes. Parts of section 2.2 were published in Fuchs et al. (2015), Fuchs et al. (2016c), and Fuchs et al. (2016d). Figures and text are adjusted to fit the format of this thesis.

2.1 Astigmatism PTV

In the last years spatial particle location using astigmatic aberrations was applied increasingly to measure 3D flow fields in microfluidics, as indicated by the review article of Cierpka & Kähler (2012). In principle, APTV makes use of out of focus imaging to determine the particle depth locations. Astigmatism, induced by a cylindrical lens in the optical light path, elongates the particle images, such that they have a distinct elliptical shape, depending on the particle location. The z coordinate of a particle is therefore coded in the vertical and horizontal axis dimensions, a_X and a_Y, of its particle image. Further details on the principle can be found in the introduction.

The focus of this research text lies on the description and assessment of an APTV measurement approach for macroscopic systems. Compared to microfluidics some specific challenges occur in macroscopic set-ups, which will be addressed throughout this section. The following subsection gives an overview of the particle image formation in diffraction limited astigmatic imaging systems.

2.1.1 Particle image formation

This image formation study provides a qualitative description of particle image shapes in the presence of astigmatism. In macroscopic APTV set-ups astigmatic aberrations, induced by a cylindrical lens placed in front of the camera sensor, can be considered as large aberrations. I.e. the deviation of the actual wavefront from the ideal, spherical wavefront is large. In this case, geometrical optics describe the image formation relatively accurate. Nonetheless, for a comprehensive analysis of the image formation, the influence of diffraction on image formation has to be accounted for.

According to the Huygens-Fresnel principle, the diffraction integral for the complex amplitude of the disturbance U at a point P in image space, in the presence of aberrations, is given by

$$U(P) = -\frac{i}{\lambda}\frac{Ae^{-ikR}}{R}\int\int\frac{e^{ik[\Phi+s]}}{s}dS \tag{2.1}$$

where λ is the wavelength of the light, k is the wavenumber, A is the magnitude of the disturbance at Q (point on Gaussian reference sphere), R is the radius of the Gaussian reference sphere, s is the distance between Q and P, S is the wavefront surface, and Φ denotes the aberration function (Born & Wolf (1997)). This aberration function describes the deviation of wavefronts from ideal, spherical wavefronts at the exit pupil. If $\Phi = 0$, i.e. no aberrations in the optical system are present, the solution of Eq. (2.1) is the Airy-pattern. In the case of astigmatism, Nijboer (1943) give the aberration function by

$$\Phi_{\text{ast}} = \beta_{\text{ast}}\, r^2 \cos(2\varphi) \tag{2.2}$$

where β_{ast} denotes the quantitative deviation of the aberrated wavefront from the ideal wavefront, and r and φ are polar-coordinates of Q. According to Nijboer (1943), for spherical aberrations, the aberration function is

$$\Phi_{\text{sph}} = \beta_{\text{sph}}\, r^4 \tag{2.3}$$

where the amount of spherical aberration is denoted by β_{sph}. By introducing the coordinates p (along the optical axis) and the polar-coordinates q and ψ for P in image space, Van Kampen (1949) formulates the diffraction integral in the presence of astigmatic and spherical aberration as

$$\begin{aligned} U(P) = C \cdot \int_0^{2\pi}\int_0^{a} \exp\Big[i\big(r^2 p + rq\cos(\varphi-\psi) - \\ -\beta_{\text{ast}} r^2\cos(2\varphi) - \beta_{\text{sph}} r^4\big)\Big] r\, dr\, d\varphi \end{aligned} \tag{2.4}$$

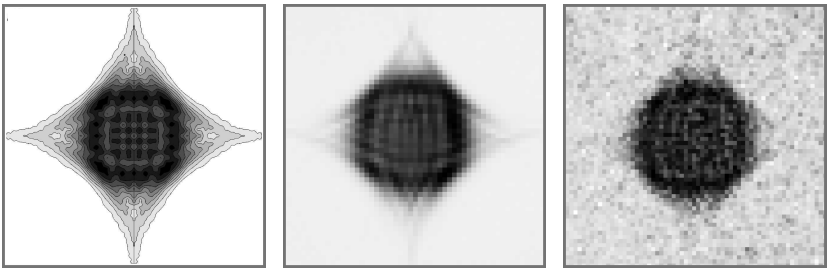

(a) simulated image (b) image of a 5 µm pinhole (c) image of a 1 µm pinhole

Figure 2.1: Intensity coded pinhole/particle images in the central plane. Note that the intensity is inverted and that the intensity scaling differs between the images. Particle/pinhole images show an asteroid shaped diffraction pattern, a high SNR provided.

where a is the exit pupil radius and C is described by

$$C = i\frac{kA}{2\pi R}e^{-ikR}. \tag{2.5}$$

For small aberrations, i.e. the deviation of the actual wavefront from the ideal wavefront being less than λ, Nijboer (1947) calculate the diffraction image by expanding the aberration function in a series of circular polynomials. An experimental verification of this treatment is given by Nienhuis & Nijboer (1949). If aberrations are somewhat larger, i.e. the deviation is several times λ, an asymptotic expansion of the diffraction integral can be applied to calculate the diffraction image, as shown by Van Kampen (1950). For the presented analysis, *Matlab* is used to solve Eq. (2.4) numerically, since the approximated analytical solutions are much less accurate and are only suitable for certain parameters. The resulting intensity at P is then calculated as

$$I(P) = |U(P)|^2. \tag{2.6}$$

In the presence of astigmatism, the location of the plane of least distortion, i.e. midway between the focal planes, is at $p = 0$. Here, particle images show asteroid shapes with a circular ring of higher intensity (see Fig. 2.1 and Towers et al. (2006), Van Kampen (1949), and Born & Wolf (1997)). The image of the backside illuminated pinhole with a diameter of 5 µm (see Fig. 2.1(b)) matches very well with the simulated image in Fig. 2.1(a). The asteroid shape can hardly be observed with a lower SNR, as illustrated by the image of the backside illuminated 1 µm pinhole in Fig. 2.1(c). In this case, the particle image has a circular shape of almost equi-distributed intensity with a less distinct outer ring. The geometrical theory of aberrations predicts a circular image of constant intensity

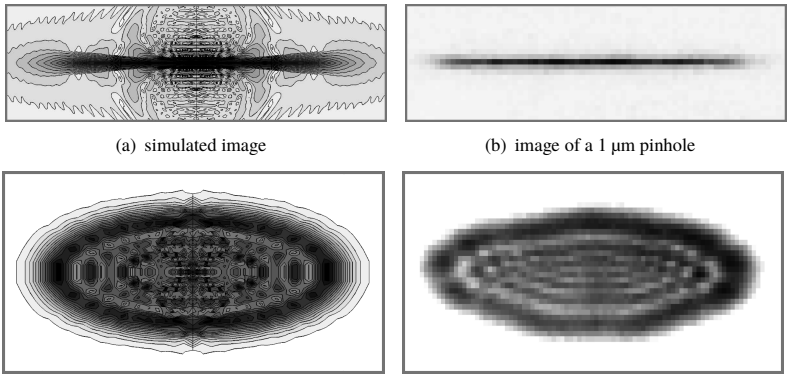

(a) simulated image

(b) image of a 1 µm pinhole

(c) simulated image

(d) image of a 5 µm pinhole

Figure 2.2: Intensity coded pinhole/particle images in the focal plane and well beyond. Note that the intensity is inverted and that the intensity scaling differs between the images. Near the focal planes, the particle images form thin lines. Beyond the focal planes, the axis lengths increase in both directions.

in the central plane, quite similar to the image analyzed in Fig. 2.1(c).

The distance of the two focal planes is determined by the amount of astigmatism. Their location is denoted by $p = \pm\beta_{\text{ast}}$ along the optical axis. Particle images at the focal planes form thin lines of high intensity, as seen in Figs. 2.2(a) and 2.2(b), whereas geometrical optics predicts one axis length to be zero, provided ideal lenses are present (see Nienhuis & Nijboer (1949)):

$$a_X = 2a\,|p + \beta_{\text{ast}}| \tag{2.7}$$

$$a_Y = 2a\,|p - \beta_{\text{ast}}|\,. \tag{2.8}$$

Beyond the focal planes, i.e. $p > \beta_{\text{ast}}$ or $p < -\beta_{\text{ast}}$, both axes grow with a bright outer ring and less accentuated rings in the particle image center (Figs. 2.2(c) and 2.2(d)).

Spherical aberrations have only limited influence on image formation in macroscopic domains, since the amount of spherical aberrations is small compared to the induced astigmatic aberration ($\beta_{\text{ast}} >> \beta_{\text{sph}}$). Therefore, spherical aberrations can be neglected for the image formation analysis in macroscopic domains. In microscopic domains the influence of spherical aberrations on the image formation is significant, as the focal plane distances are small ($\beta_{\text{ast}} \approx \beta_{\text{sph}}$). In macroscopic domains, the appearance of particle images can be considered to be symmetric with respect to $p = 0$, but rotated by 90°. In microscopic domains, particle images beyond one focal plane ($p > \beta_{\text{ast}}$) have a bright outer ring and beyond the other focal plane ($p < -\beta_{\text{ast}}$) they have a bright central spot with

decreasing intensity towards the particle image edge. With a sufficiently small amount of astigmatism, the asteroid shaped diffraction pattern cannot be observed anymore. Instead particle images have cross-shaped central spots in the center. In this case the location of the focal planes cannot be determined as easily, as particle images do not form thin lines anymore.

However, for macroscopic air flow measurements, employing the APTV technique, di-ethyl-hexyl-sebacate (DEHS) seeding particles with a diameter of 1 µm are used (Kähler et al. (2002)). The resulting SNR of the particle images is rather low, due to these small seeding particles. Therefore, the preprocessing of the recordings is a crucial procedure for performing accurate flow measurements.

2.1.2 Image preprocessing

A careful preprocessing of the recordings is very important to be able to accurately determine the particle image geometry. Thus, it is the goal of the image preprocessing procedure to yield an initial estimation of the particle image properties, i.e. the pixel area, the axis lengths a_X and a_Y, the sensor location $\boldsymbol{X} = (X, Y)$, the mean intensity, and the maximum intensity.

The first step of the preprocessing is the subtraction of an intensity averaged image of all recordings from each recording, to eliminate light reflections, scratches on surfaces, and other imperfections as good as possible. Then, if the SNR of the particle images is sufficiently high, a binarization by means of an intensity threshold can directly be applied to detect the individual particle images. Likely, for macroscopic APTV measurements, it is necessary to perform some additional preprocessing steps. An intensity normalization is helpful, when the SNR ratio of the particle images is unevenly distributed over the image. To better distinguish particle images with low SNRs from the background, non-linear filters, such as the subtraction of the local minimum intensity, or a minimum/maximum filter with kernel sizes in the range of the particle image diameter, are suitable. The commercially available software *DaVis* from *LaVision* is a powerful and efficient tool to conduct these preprocessing procedures. The last step is again to apply an intensity threshold to detect the individual particle images. An overview of the procedure is given in Fig. 2.3.

Following the preprocessing of the recordings and the detection of the particle images, their geometry, i.e. the axis lengths a_X and a_Y and the particle image center locations are determined with sub-pixel accuracy. For this geometry determination, the background subtracted images are used.

2.1.3 Particle image geometry determination

The accurate determination of the particle image dimensions has a strong influence on the measurement uncertainty, since the spatial particle locations are derived from the

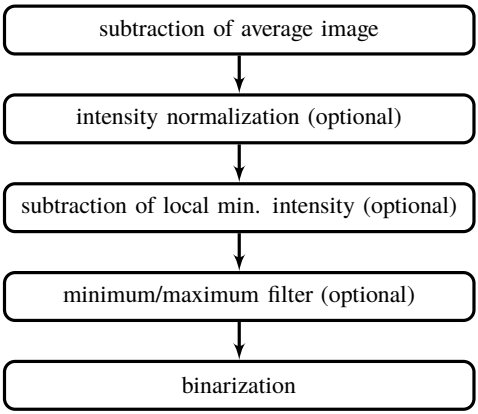

Figure 2.3: Overview of the image preprocessing steps

particle image axis lengths and the center locations. To account for particle image shapes as observed in macroscopic APTV set-ups, outlined in subsection 2.1.1, a suitable image processing algorithm is established.

In a first step, the local intensity distributions at the four vertices of the elliptical particle images are analyzed, as illustrated in Fig. 2.4. After the initial detection of the particle images from a binarized image, the intensities in a 11×5 pixel kernel at each vertex, where the intensities are averaged column-wise for the left and right vertex, yielding the intensities $\bar{I}_1, \bar{I}_2 ... \bar{I}_{11}$. For the upper and lower vertex, the intensity is averaged row-wise, respectively. These averaged intensities are then normalized by the mean intensity of the particle image. This normalization minimizes the impact of differing illumination intensities and distributions on the geometry determination, increasing the robustness. The intensity values are then fitted by means of a thin-plate spline fit at each vertex, where a global intensity threshold denotes the actual sub-pixel locations of the particle image edges.

Thus, the horizontal particle image length, a_X, is denoted by the distance between the left and the right edge, whereas the vertical axis length, a_Y, is denoted by the distance of the upper and lower edge. Since in macroscopic APTV set-ups the particle images do not have an intensity peak in the particle image center, but rather a constant intensity, the particle image center cannot be determined using a Gaussian fit. Instead, the particle image center is computed from the edge locations and therefore lies halfway between the horizontal and vertical edge of the particle image.

The image formation study has proven that in macroscopic APTV set-ups image formation is dominated by astigmatism, leading to similar shaped particle images. As a consequence, the macroscopic APTV processing and calibration procedures are applica-

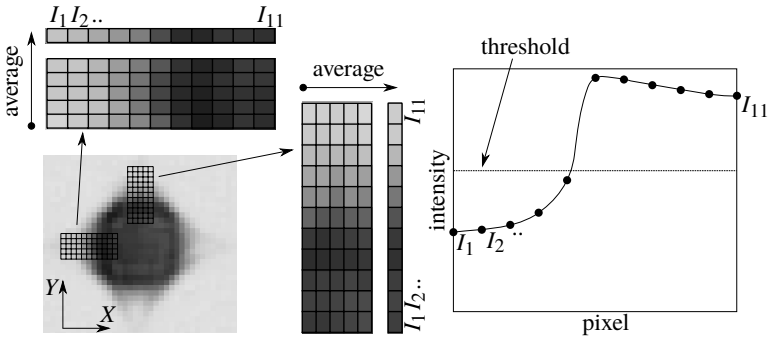

Figure 2.4: Principle of APTV particle image edge location determination

ble independently of the measurement set-up. Since for APTV systems, the spatial particle locations are coded in the particle image geometry, a mathematical relation between the geometry and the location needs to be established for calibration.

2.1.4 Calibration and particle location determination

Finding a mathematical description of the relation between the image information and the physical space is the object of the calibration procedure. For APTV, the particle depth (z) location, along the optical axis, is estimated from the particle image geometry, more specifically the axis lengths a_X and a_Y. However, it is difficult, if not impossible, to place particles at known locations within the measurement volume to derive the calibration information. An elegant way to overcome this drawback is to use a backlight illuminated pinhole matrix, as shown in Fig. 2.5. According to Babinet's principle, pinholes have the same light emission behavior as particles of the same diameter. Therefore, these pinholes are well suited for the calibration of macroscopic APTV systems, since the locations of the pinholes within the measurement volume are known, relative to a reference point, and the particle image geometries can be related directly to the pinhole image geometries.

The geometry of a particle image does not only depend on the particle z location, but also on its x and y location, since the focal planes are curved, due to the so-called Petzval field curvature. In addition, distortions in the optical path have to be accounted for. Hence, it is necessary to establish a calibration function depending on the geometry of a particle image and the spatial coordinates of the corresponding particle. Therefore, the first step of the macroscopic APTV calibration procedure is to determine a function for the particle z location, depending on the sensor location $\boldsymbol{X} = (X, Y)$ and the particle

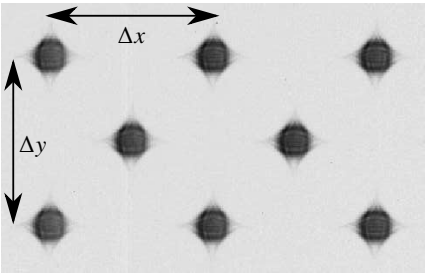

Figure 2.5: Intensity inverted grey-scale image of a pinhole matrix section with known distances, Δx and Δy, between the pinholes

image axis ratio a_X/a_Y

$$z = f(\boldsymbol{X}, a_X/a_Y)\,. \tag{2.9}$$

In a second step, a mathematical description, mapping the particle z location and the particle image sensor coordinates $\boldsymbol{X}$ to physical coordinates $\boldsymbol{x} = (x, y, z)$ needs to be determined, since the reproduction scale changes with distance from the camera. This yields a function of the type

$$\boldsymbol{x} = f(\boldsymbol{X}, z)\,. \tag{2.10}$$

The procedure to determine function (2.9) is the following: The pinhole matrix is moved through the measurement volume along the optical axis in steps of around 1% of the focal plane distance Δz_{fp}. At each z location, the backlight illuminated pinhole matrix is imaged multiple times, to eliminate influences of changing illumination conditions. These images are then intensity averaged and preprocessed as outlined in subsection 2.1.2. The geometries of the pinhole images are determined according to the description in subsection 2.1.3. Surface spline fits are then applied to the axis ratio values of the pinhole images detected on the averaged recordings at every z location, as illustrated on the left side of Fig. 2.6. Now, for any sensor location a unique calibration function can be determined by means of a line spline fit, as shown qualitatively by the solid and the dashed on the right side of Fig. 2.6.

With these unique calibration functions, the z locations of particles are approximated by their particle image axis ratio and the sensor location. When measuring beyond focal planes, the calibration functions become ambiguous, as seen in Fig. 2.7, showing an actual calibration function of macroscopic APTV set-up for a specific sensor location. These ambiguities can be overcome by analyzing the axis lengths of the particle images. Whereas axis ratios have a minimum or maximum at focal planes, the larger axis of a particle image changes linearly near the corresponding focal plane, as shown by Rossi & Kähler (2014). Thus, the length of the larger particle image axis determines whether the

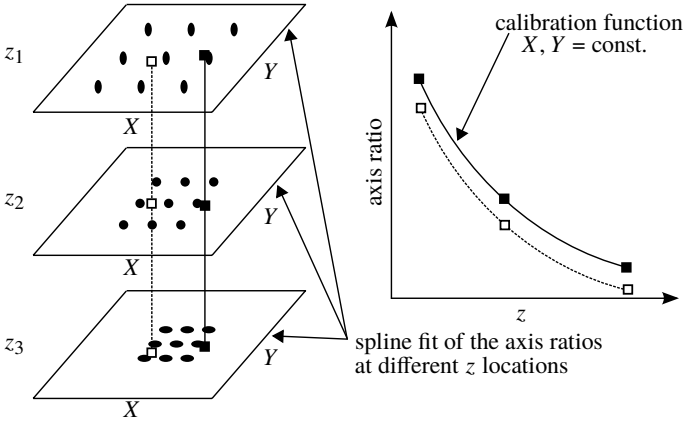

Figure 2.6: Macroscopic APTV calibration principle: First, the axis ratio values are fitted with surface splines at every z location. Second, a calibration curve for the $\boldsymbol{X} = (X, Y)$ sensor location of a pinhole image is established, using a line spline fit, where the z location is denoted by the axis ratio, a_X/a_Y, of the particle image.

particle location is within or beyond the focal planes.

So far, only the particle z locations can be determined. The second step of the calibration procedure needs to find a relation between particle image sensor location $\boldsymbol{X}$, the particle z location and the x and y coordinate of the spatial particle location, as indicated by Eq. (2.10). For macroscopic APTV, fifth order polynomials are used for mapping the coordinates, here exemplary for the x coordinate,

$$x = \sum_{i,j,k} c_{i,j,k}\, X^i\, Y^j\, z^k, \quad i + j + k \leq 5 \tag{2.11}$$

where $c_{i,j,k}$ denotes the coefficients of the polynomial. For the y coordinate, the polynomial function is formulated accordingly, whereas the z location is already determined. However, before being able to compute the spatial particle locations using these polynomial mapping functions their coefficients need to be determined. A dotted calibration target can be used to derive the required information, i.e.
the calibration points with known sensor locations $\boldsymbol{X}$ and their corresponding physical coordinates $\boldsymbol{x}$, for determining $c_{i,j,k}$. But, since the pinhole matrix is moved through the measurement volume for the particle/pinhole image geometry calibration, the known spatial locations of the pinholes and the sensor coordinates of their pinhole image center locations can be utilized.

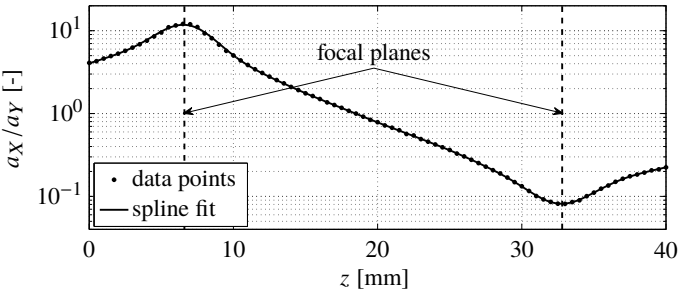

Figure 2.7: Calibration function for a specific $\boldsymbol{X} = (X, Y)$ sensor location. Both the minimum and maximum values of the axis ratio, a_X/a_Y, denote focal planes. The focal plane distance is $\Delta z_{\mathrm{fp}} \approx 25$ mm.

In practice, the coefficients are estimated by solving following set of equations in the least squares sense, in this particular case, the coefficients $\boldsymbol{c}_x$ for the x coordinate

$$\left(S^{\mathrm{T}} S\right) \boldsymbol{c}_x = S^{\mathrm{T}} \boldsymbol{x}_n \tag{2.12}$$

where $\boldsymbol{x}_n$ is a $n\times1$ vector containing the x locations of n pinholes. The coefficients $\boldsymbol{c}_y$ are estimated accordingly. In Eq. (2.12), S denotes a $n\times55$ matrix, of the n pinhole images. The 55 entries represent the right side of Eq. (2.11), where X, Y, and z are the sensor coordinates and the depth locations of the nth pinhole. Typically, at each z location of the pinhole matrix, several hundred pinhole images are processed, such that the total number of pinholes exceeds 10000 by far.

To summarize, the particle location determination requires two steps. First, the depth location of the particle is determined from the particle image axis ratio and its sensor location. In a second step, the particle x and y coordinate is estimated by means of a polynomial mapping function from its z location and its particle image sensor center location $\boldsymbol{X}$. The calibration functions are derived using a pinhole matrix as a calibration target, for both the geometry calibration and the coordinate mapping. Hence, employing a pinhole matrix enables a simultaneous calibration of both processing steps, saving measurement and processing time. Additionally, an error-prone alignment of different calibration targets is avoided.

Using the particle locations, the flow velocities are estimated by means of particle tracking algorithms, either for double-frame, multi-frame, or a time-series of recordings. These algorithms include straightforward nearest-neighbor solutions, or more advanced approaches, as introduced by Ohmi & Li (2000) and Cierpka et al. (2013). To prove the feasibility of APTV for macroscopic flow measurements, a quantitative uncertainty analysis is presented in the following.

2.1.5 Measurement uncertainty

The measurement uncertainty is the most important measure to assess the suitability of a technique for an accurate flow velocity estimation. A quantitative analysis of the particle location determination as well as the particle displacement uncertainty reveals, if a measurement approach can measure flows with strong velocity gradients and which spatial resolution can be achieved. The first part of the uncertainty analysis estimates the particle z location using the known physical locations of the pinholes. In the second part, the particle displacement uncertainty is estimated by means of a "motionless" flow.

Particle *z* location uncertainty

The object of this uncertainty analysis is to give a quantitative measure of the particle location determination error of a macroscopic APTV set-up with a measurement volume size of 20×20×40 mm^3. The analysis is conducted with state-of-the-art PIV recording and illumination equipment. Since the particle z location has the largest error, the study focuses on the depth location determination. For the systematic investigation, particles are simulated by pinholes, where the pinhole diameter is $d_{\text{pin}} = 1.1 \pm 0.1$ µm and the vertical and horizontal pinhole displacement is 4 mm. The matrix is backlight-illuminated by an *Innolas SpitLight 400* PIV laser with a maximum pulse energy of 240 mJ and moved through the measurement volume depth of 40 mm in steps of $\Delta z_{\text{s}} = 0.5 \pm 0.006$ mm. At every z location, 20 images are recorded, using a *PCO edge* sCMOS camera. The cylindrical lens is placed in front of the camera sensor to induce astigmatism. It has a focal length of $f_{\text{cyl}} = 1000$ mm, leading to a focal plane distance of $\Delta z_{\text{fp}} \approx 25$ mm. The experiments are conducted at a working distance of 290 mm, measured from the camera sensor to the central plane of the measurement volume.

The images are processed as described in subsection 2.1.2, 2.1.3, and 2.1.4. To compute the particle z location determination uncertainty, the absolute deviations, Δz, of the estimated locations compared to the actual locations are analyzed, as illustrated in Fig. 2.8. Thus, the uncertainty at every z location is calculated by

$$E_z = \sqrt{\frac{\sum_{i=1}^{n} (\Delta z)^2}{n-1}} \tag{2.13}$$

where n denotes the number of analyzed pinholes. For each z location a data set of about 300 particle images is analyzed. Figure 2.9(a) shows the distribution of E_z along z, at a measurement depth of 40 mm. At both focal planes (approximate z locations: 8 and 32 mm), E_z has peaks even though the SNRs are large. This can be explained by the calibration function which has a maximum or minimum at the respective focal planes (see Fig. 2.7). Generally, E_z increases with decreasing slopes of the calibration functions. Lower SNRs yield higher E_z values as well. The average error is $\overline{E}_z = 0.133$ mm, which is equivalent to 0.33% of the measurement volume depth. An adjustment

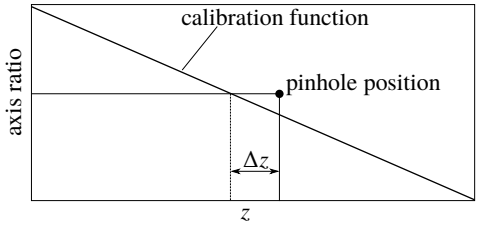

Figure 2.8: Principle of uncertainty estimation

of the processing parameters improves the E_z values for the area between the vertical dashed lines, i.e. only the area between the focal planes is considered. Large particle images with low SNRs located beyond the focal planes cannot be processed with these parameters. The distribution of E_z is then relatively uniform and follows the slope of the calibration function, as shown in Fig. 2.9(b). For a resulting measurement depth of 23.5 mm the uncertainty yields $\overline{E}_z = 0.075$ mm, which equals 0.32% of the measurement volume depth. Note that the uncertainty scales with the focal plane distance, resulting in constant relative E_z values.

Particle displacement uncertainty

In addition to the particle z location determination analysis, an analysis of the statistical measurement uncertainty is carried out. This displacement uncertainty analysis is performed by means of the measurement of a "motionless" flow, using standard DEHS seeding particles. The double-frame recordings of the illuminated particles have a time separation of $\Delta t = 0.5$ µs. Since there is no driven flow, the displacement of the particles between the light pulses approaches zero ($\Delta \boldsymbol{x} \rightarrow 0$). However, processing the particle images, a displacement $\Delta \boldsymbol{x} \neq 0$ is likely estimated, resulting from external influences, such as misalignments of the laser light volume illumination, image noise, and light reflections. The statistical measurement uncertainty, σ, is calculated by the standard deviation of the displacements $\Delta \boldsymbol{x} = (\Delta x, \Delta y, \Delta z)$ of the particles between the two light pulses.

The measurements are conducted using a *PCO edge* sCMOS camera with a 50 mm *Zeiss* macro objective lens. The reproduction scale in the volume center is 35 µm/pixel, at $M = 0.185$. The measurement volume was illuminated using an *Innolas SpitLight Compact 200* PIV laser with a maximum pulse energy of 140 mJ. A cylindrical with a focal length of $f_{\mathrm{cyl}} = 500$ mm in front of the camera sensor yields a focal plane distance of $\Delta z_{\mathrm{fp}} \approx 50$ mm. The resulting measurement volume size is 20×20×45 mm^3.

For the x and y coordinate the displacement uncertainty yields $\sigma_{x,y} \approx 0.2$ pixel, which

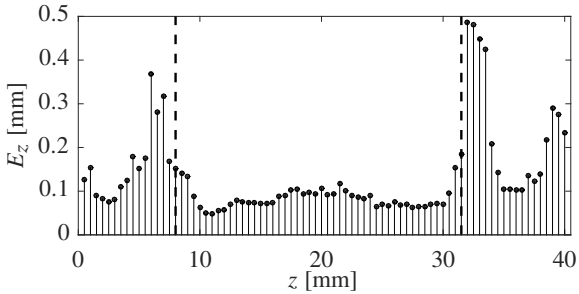

(a) uncertainty for the entire measurement volume

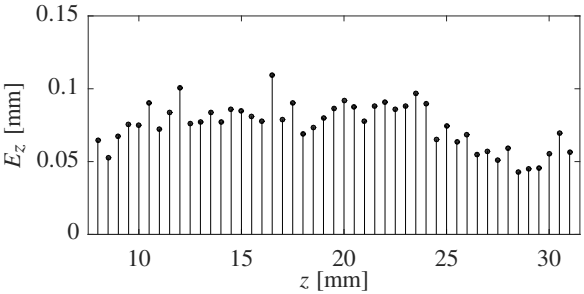

(b) uncertainty for the volume between the focal planes

Figure 2.9: Particle z location uncertainty

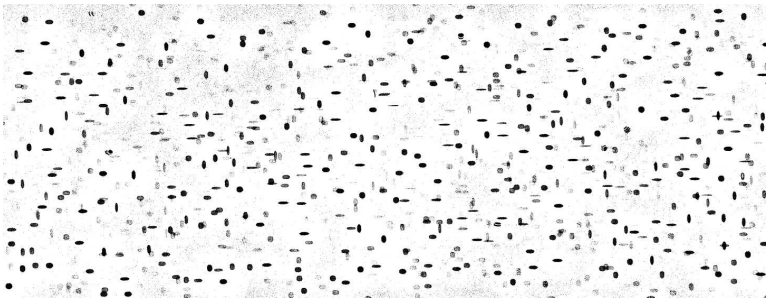

Figure 2.10: Intensity inverted, color-coded grey scale image of astigmatic particle images as seen in the "motionless" flow analysis

equals 7 µm for this set-up. The uncertainty in the z direction is somewhat larger with σ_z = 140 µm. This corresponds to 4 pixel if the physical uncertainty is normalized with reproduction scale. The larger uncertainty of the z location results from the fact that the particle image axis lengths determination is more influenced by changing illumination conditions and changing physical properties of the individual particles, compared to the center location determination. Thus, the particle depth location determination is more error-prone.

Note, that this "motionless" flow analysis provides a true measure of the APTV measurement uncertainty, since the experiments are conducted under realistic measurement conditions. Altogether, the uncertainty analysis reveals that macroscopic APTV set-ups provide a spatial resolution, being significantly better than typical light sheet thicknesses in planar PIV set-ups, which yield around 1 mm or more. Using APTV, the in-plane flow velocities can be estimated with uncertainties comparable to these of planar PIV techniques, along with the capability of resolving strong velocity gradients in depth direction. With a rather large uncertainty in the measurement of the velocity in z direction, macroscopic APTV can be considered as a volumetric two-component (3D2C) flow velocimetry technique.

It was mentioned in the beginning of this chapter that APTV is advantageous over DPTV, since the distribution of the SNR is homogenous along the measurement depth. However, for small measurement depths this is not a severe problem, such that defocusing imaging can be combined with an *in situ* calibration, as described in the following section.

2.2 *In situ* calibrated defocusing PTV for wall-bounded measurement volumes

In many situations, 3D velocity measurements in thin (~1 mm) but wide (~100×100 mm^2) flow channels is an important task. These wall-bounded domains with small depths cannot be measured by standard 2D measurement techniques, since they fail to resolve strong velocity gradients and small-scale flow features in depth direction due to the integration over the light sheet thickness. Thus, volumetric velocimetry approaches are required for these environments.

However, 3D velocimetry techniques require an accurate calibration procedure to achieve reliable results. Normally, calibration targets with dots or other geometrical patterns are placed within the measurement volume to derive the calibration points. In small-scale environments it is not always possible to place targets, since they do not fit into these confined volumes. Moreover, the measurement domain might not be accessible at all without a major disassembly of the test facility, which is very likely in turbomachinery or combustion applications. Moving the optical equipment can make a calibration procedure unusable, because of misalignments in the assembly. Hence, conducting flow measurements in these domains is very challenging.

To overcome these drawbacks, in this section an *in situ* calibrated defocusing PTV

approach for wall-bounded measurement domains with depth dimensions on the order of 10^0 mm is introduced. This includes a comprehensive description of the technique, along with an uncertainty analysis, where a tomographic PTV procedure serves as benchmark for the defocusing approach.

This particular defocusing approach employs the diameter of the first diffraction ring to determine the particle depth location. Further details concerning the principle can be found in the introduction. While defocusing imaging is not capable of measuring over large depths, due to some specific drawbacks, the method is suitable for small z dimensions, as in the present case. Figure 2.11 shows a representation of the appearance of defocused particle images and the corresponding depth locations of the particles.

2.2.1 Image preprocessing

For accurately determining the particle image geometry, a careful preprocessing of the recordings is very important. Thus, it is the goal of the image preprocessing procedure to yield an initial estimation of the particle image properties, i.e. pixel area, particle image diameter, sensor location, and intensity.

The first step of the preprocessing is usually the subtraction of an intensity averaged image of all recordings from each image. Stationary light reflections, scratches on surfaces, and other imperfections are largely eliminated using this background subtraction procedure. Then, if the signal to noise ratio (SNR) of the particle images is sufficiently high, a binarization by means of an intensity threshold can be directly applied to detect the individual particle images. However, most likely for defocusing particle imaging it is necessary to perform some additional preprocessing steps. An intensity normalization is helpful, when the SNR of the particle images is unevenly distributed over the image. To better distinguish particle images with low SNRs from the background, non-linear filters, such as the subtraction of the local minimum intensity, or a minimum/maximum filter over roughly the particle image size in pixels, are suitable. The final step is to apply an intensity threshold to detect the individual particle images, allowing for a diameter determination with sub-pixel accuracy, as outlined in the following.

2.2.2 Particle image diameter determination

The particle z location is uniquely related to the diameter of the first diffraction ring of the particle image. To determine this diameter, the intensity distributions at the vertical and horizontal extrema of the diffraction ring, i.e.
at the minimum/maximum X and Y sensor coordinates of the particle image, are analyzed. The intensities are averaged row-wise or column-wise, respectively, in a 11×5 pixel^2 kernel at each of the four extrema locations. A thin-plate spline approximates the intensity distribution along the diffraction ring. This edge location determination scheme is illustrated in Fig. 2.12. For defocused particles images, an intensity peaks appears and

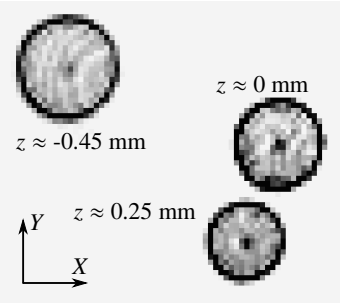

Figure 2.11: Defocused particle images and their approximated z locations in a channel with a depth of 1 mm

then the intensity drops again. At first, it appears logical to employ the maximum of this intensity distribution as the particle image edge location. However, the maximum location is strongly affected by peak locking, as illustrated in Fig. 2.13(a), since the width of the diffraction ring is very small and large parts of the diffraction ring intensity gather in a single pixel. Peak locking means that the fitted sub-pixel coordinates are biased towards integer values, if, like in this case, the intensity peak is not wide enough.

Thus, instead of the local intensity maximum, the particle image edge location is denoted by an intensity threshold of the local intensity distribution, such that no pixel-locking is present (see Fig. 2.13(b)). This adaptive threshold is the intensity average of a 5×5 pixel^2 kernel around the extrema locations of the particle image. Without this adaption, the particle depth location would have a strong dependency on the intensity of its particle image, since the particle image diameter increases with its brightness at a constant intensity threshold, as it is illustrated in Fig. 2.14. Differing particle image intensities (SNRs) can occur from differing physical diameters of the seeding particles and changing illumination intensities of the laser beam profile.

Using the diffraction ring position, the diameter, a_{XY}, of the particle image is denoted by the average diameter along the X and the Y axis of the first diffraction ring

$$a_{XY} = \frac{a_X + a_Y}{2}. \tag{2.14}$$

With increasing particle image diameters the intensity peak in the particle image center becomes less distinct and eventually disappears. Therefore, the particle image center locations are not determined by fitting this peak. Instead, the center is located halfway between the approximated vertical and horizontal diffraction ring positions.

Unlike in tomographic imaging, there are no ghost particles present in defocusing PTV, since no ambiguities can arise due to the single viewing direction. Instead, particle image overlaps can appear, which do not allow for an accurate particle location determination

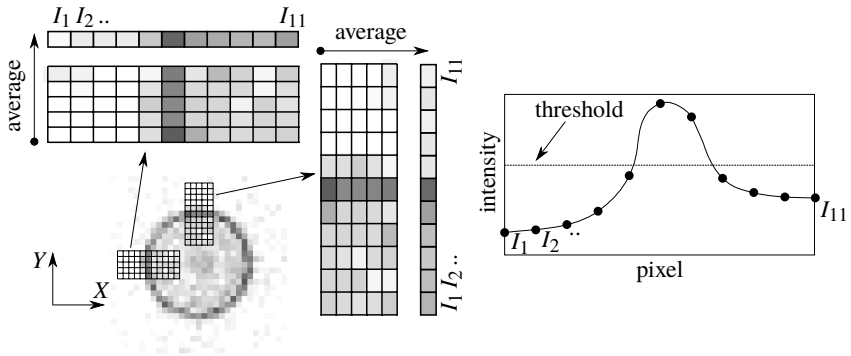

Figure 2.12: Defocusing PTV particle image edge determination scheme

anymore. To minimize the number of overlapping particle images, the seeding concentration needs to be rather low. Nevertheless, also at lower seeding densities overlaps are present and therefore need to be detected. To do so, the particle image shapes are analyzed in terms of their roundness, their size, and their aspect ratio to distinguish valid from invalid particle images. Remaining overlaps, which are not detected can lead to outliers in the measured velocities, if they are not eliminated in the tracking step. In the following, the procedure to calibrate the defocusing system using the measurement data together with the particle location determination is outlined.

2.2.3 *In situ* calibration and particle location determination

For the calibration of the defocusing system, a relation between the particle image diameter and the particle z location has to be established. It was outlined before that it is not always possible to place a calibration target within the measurement volume, if the thin measurement plane is close to a surface. Furthermore, the measurement domain might not be accessible at all without a major disassembly of the test facility. Finally, moving the optical equipment can make a calibration procedure unusable, because of misalignments during the assembly. Therefore, an *in situ* calibration is very important to overcome these problems.

The possibility of an *in situ* calibration is based on a strictly linear change of the particle image diameter along the optical axis, i.e. in z direction. Figure 2.15 shows this linear behavior of the particle image diameter over several millimeters in depth, measured using a pinhole with a diameter of 5 µm. With the knowledge of the measurement domain dimensions and the particle image diameters at the upper and lower measurement domain

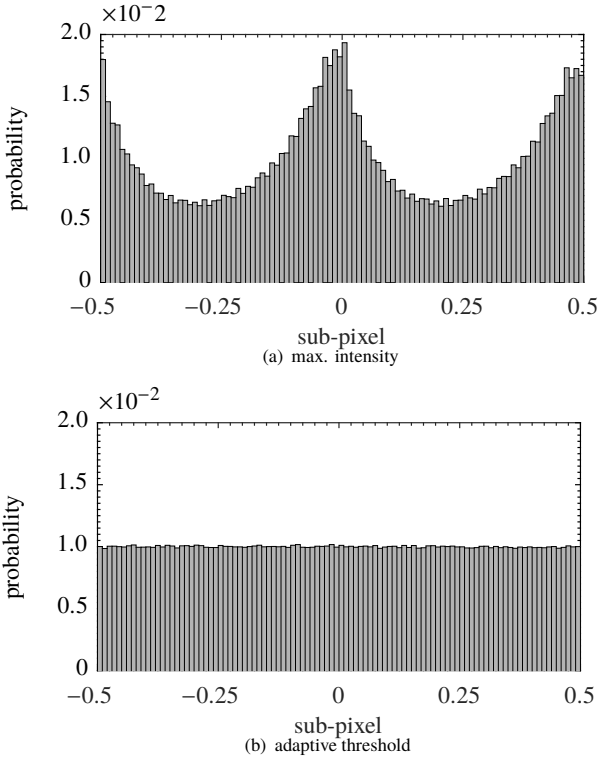

Figure 2.13: Peak locking analysis for using the maximum intensity as the particle image edge (a) and with an adaptive intensity threshold (b)

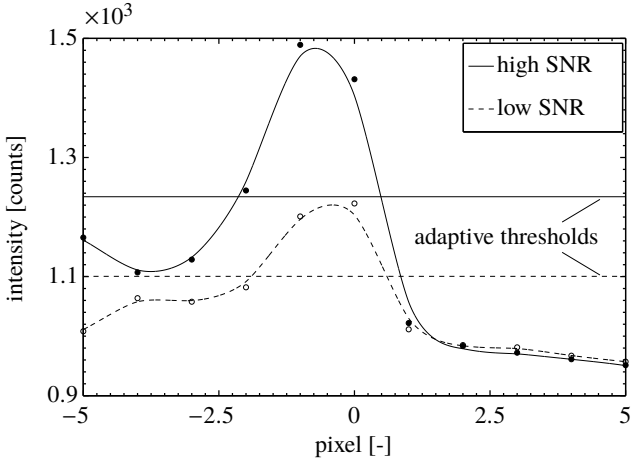

Figure 2.14: Working principle of the adaptive threshold for the particle image edge location determination: the solid lines denote the thin-plate spline fit and the adaptive threshold SNR with and without adaptive threshold.

boundary, the particle z location can be determined by

$$z = \frac{a_{XY} - a_{XY,\min}}{a_{XY,\max} - a_{XY,\min}} d_z \tag{2.15}$$

where $a_{XY,\min}$ is the minimum diameter of the particle image at the wall, $a_{XY,\max}$ is the maximum particle image diameter at the other wall, and d_z denotes the measurement volume depth. Equation (2.15) applies if the wall at the minimum diameter is set to $z = 0$.

In practice, the in-situ calibration procedure is conducted as follows. Having determined the particle image diameters and their sensor locations, the particle image displacements between two frames are estimated by means of particle tracking algorithms. While the z location of the particle is not yet determined, the particle image diameter a_{XY} serves as third displacement component, along with the displacement on the sensor, ΔX and ΔY. Spurious particle image displacements are filtered out by confining the allowed diameter change. The initial tracking step yields a velocity distribution over the particle image diameter, as shown in Fig. 2.16. Since the displacement at the wall approaches zero, it is the next step to determine the particle image wall diameters, $a_{XY,\min}$ and $a_{XY,\max}$, by means of a linear fit of the displacement data near to the walls, as shown in Figure 2.17. To account for misalignments of the camera and optical aberrations, this wall diameter determination is not conducted for the entire set of displacements. Instead, the measurement volume is divided into several hundred squared sensor sections, in each of which these wall diameters are determined. Likely, spurious wall diameter

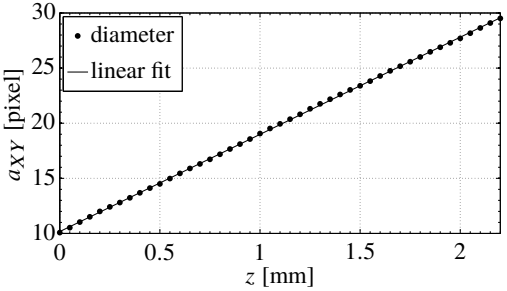

Figure 2.15: Particle image diameter over z

estimations occur, maybe due to light reflections on the wall yielding erroneous particle image displacements or other distortions. Thus, the wall diameters are smoothed by means of a spline fit for the two walls as it is illustrated in Figure 2.18. This, yields a unique calibration function for the particle z location, depending on the sensor location $\boldsymbol{X}$ of the particle image, where the particle z location can be computed from the particle image diameter using Eq. (2.15). Figure 2.19 gives an overview of the *in situ* calibration procedure.

Since this approach is targeting at wall-bounded measurement domains with small measurement depths, the x and y location of a particle can be deduced directly from its sensor coordinate by a simple scaling. The scaling can be done by employing two markers on the window or distinct points of the measurement domain geometry.

2.2.4 Benchmark measurement: Tomographic PTV

This tomographic PTV approach serves as an uncertainty benchmark for the *in situ* calibrated defocusing approach and it is therefore introduced briefly. Tomographic reconstruction, from multiple views of illuminated particles, yields a 3D intensity distribution of the measurement volume, discretized on a voxel grid (Scarano (2013)). For this study, *LaVision*'s software *DaVis 8.1.5* is used for imaging, calibration, and reconstruction. Prior to the volume reconstruction, the raw images are preprocessed with the following steps. First, the average image of all recordings is subtracted from each individual recording to remove background reflections. Additionally, a local minimum intensity subtraction is applied to the images, as well as an intensity normalization using local averages. All frames are intensity normalized with respect to the first frame. In a last preprocessing

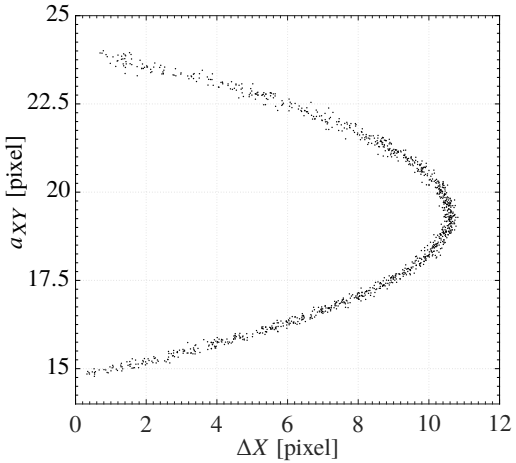

Figure 2.16: Particle image diameter over displacement

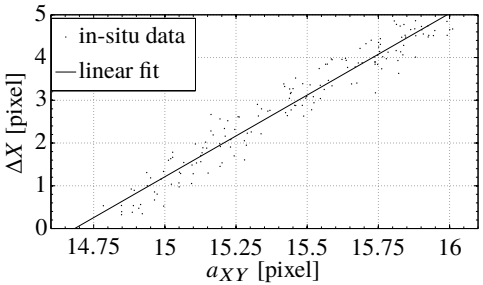

Figure 2.17: Wall particle image diameter determination

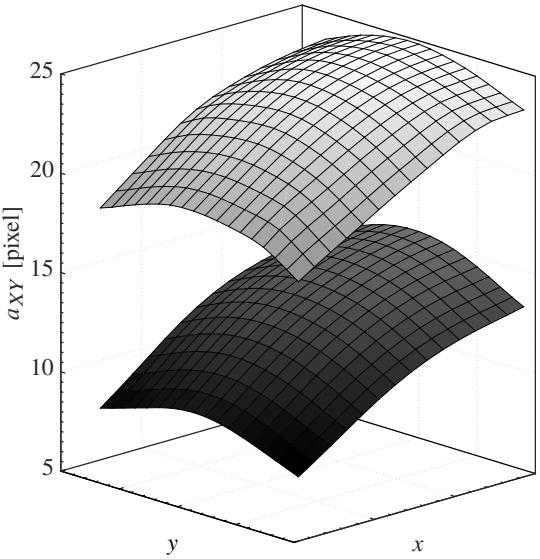

Figure 2.18: Wall particle image diameter surface fit

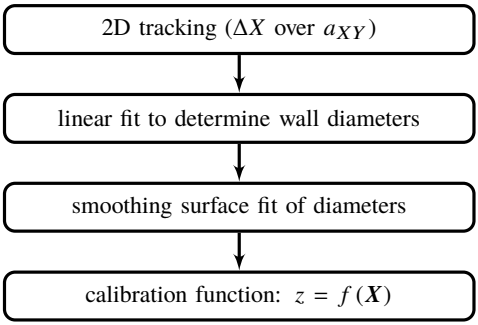

Figure 2.19: Overview of *in situ* calibration steps

step, a Gaussian smoothing is applied to the recordings, using a 3×3 pixel^2 kernel. The volume reconstruction is conducted by means of the multiplicative algebraic reconstruction technique (MART). To enhance the accuracy of the reconstructed particle intensity distribution, a self-calibration procedure is applied to the data (Wieneke (2008)). A third order polynomial serves as mapping function.

In this tomographic PTV approach, the flow velocity is derived from the displacement of the individual particles between two frames. To estimate the sub-voxel particle locations, the reconstructed volume is first binarized by means of an intensity threshold, to detect the individual particles. The size of the individual binarized particle images determine the size of the kernel, which is used for fitting the location. Since the reconstructed particles are slightly elongated in z direction, the average kernel size in z direction is 6.77 voxel, whereas it is 6.10 and 5.92 voxel in x and y direction, respectively. The sub-voxel particle location is denoted by a least squares approximation of a 3D Gaussian intensity distribution (Raffel et al. (2007))

$$I(x,y,z) = I_0 \cdot \exp\Big[-8 \cdot \Big(\frac{(x-x_0)^2}{d_{\tau_x}^2} + \frac{(y-y_0)^2}{d_{\tau_y}^2} + \frac{(z-z_0)^2}{d_{\tau_z}^2}\Big)\Big] \tag{2.16}$$

where the coefficients x_0, y_0, and z_0 denote the particle center location, I_0 denotes the intensity at peak height, and d_{τ_x}, d_{τ_y}, and d_{τ_z} denote the Gaussian peak width in the respective direction. The average peak width values of the fitted particles are $\overline{d_{\tau_x}} = 3.87$ voxel, $\overline{d_{\tau_y}} = 3.74$ voxel, and $\overline{d_{\tau_z}} = 4.47$ voxel. The average intensity is $\overline{I_0} = 3.615$ counts being significantly larger than the background intensity of 0.0003 counts. Therefore, the reconstruction quality can be considered as very high, which is also owed to the low particle image density, yielding $N_{\mathrm{ppp}} < 0.004$. With so few particles per pixel, ghost particles should not be present in the reconstructions.

2.2.5 Measurement uncertainty

Flow velocimetry in wall-bounded domains with small depth dimensions requires a 3D measurement technique, capable of resolving strong velocity gradients in depth direction. To assess the capability of the *in situ* calibrated defocusing PTV approach to measure flows in such domains, a planar Poiseuille air flow is investigated. In this analysis, a tomographic PTV measurement serves as an uncertainty benchmark.

Experiment

A sketch of the air flow experiment with a small measurement depth is shown in Fig. 2.20. It consists of two parallel glass plates with a length of 300 mm and a height of 75 mm. The distance between the glass plates and therefore the measurement depth is $d_z = 1$ mm. The flow is seeded with standard DEHS particles with a diameter of around 1 µm Kähler et al. (2002). For the illumination of the measurement volume, through the outlet of the

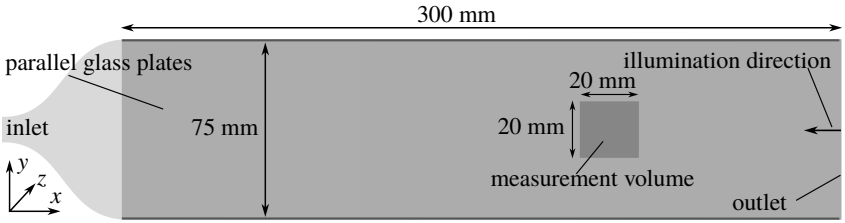

Figure 2.20: Flow experiment for the measurement uncertainty determination: two parallel glass plates with a distance of 1 mm.

channel, a double-pulse Nd:YAG laser with a maximum pulse energy of 2×40 mJ is used.

The defocusing PTV set-up is identical to that of planar PIV (see Figure 2.21). Except that out of focus particles are imaged. Therefore, the focal plane is located outside of the measurement volume. A *PCO edge* sCMOS camera is equipped with a *Zeiss* f = 50 mm macro objective lens at an aperture of $f_\# = 2$, to provide a small depth of focus, such that the particle image diameter increases significantly along the optical axis. The measurements are conducted with a magnification of $M = 0.47$ and with a reproduction scale of 13.94 µm/pixel. Altogether, two thousand double-frame recordings were analyzed with a field of view (FOV) of 20×20 mm^2. The resulting particle per pixel value is $N_{\text{ppp}} \approx 0.0001$, while the share of invalid particle images, e.g. due to overlaps, reflections on the glass plates, among others, yields around 15 %. This yields an average number of 190 tracks per double-frame recording.

The benchmark tomographic PTV set-up employs four cameras in a cross-like configuration, at an angle of $\beta = 60°$, as illustrated in Fig. 2.22. The particles are imaged with four *PCO 4000* cameras, equipped with *Zeiss* f = 50 mm macro objective lenses at a aperture number of $f_\# = 5.6$ and Scheimpflug adapters. For the calibration a dotted, dual plane target, with an offset of 1 mm between the planes, is employed. The resulting magnification is $M = 0.30$ and the reproduction scale is 30.0 µm/pixel in the image center.

Theoretical flow field

With the measurement domain's aspect ratio (width to height) of 75 and a distance of the measurement volume of 200 mm from the inlet and 100 mm from the outlet, a planar Poiseuille flow within the measurement domain can be expected. The maximum Reynolds number of the measurements is well below critical, $Re_{\text{max}} \approx 2000 < Re_c \approx 7000$ (see Karnitz et al. (1974) and Nishioka et al. (1975)), yielding a parabolic flow velocity

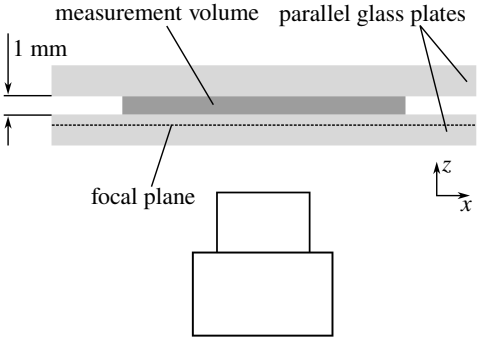

Figure 2.21: Defocusing PTV set-up

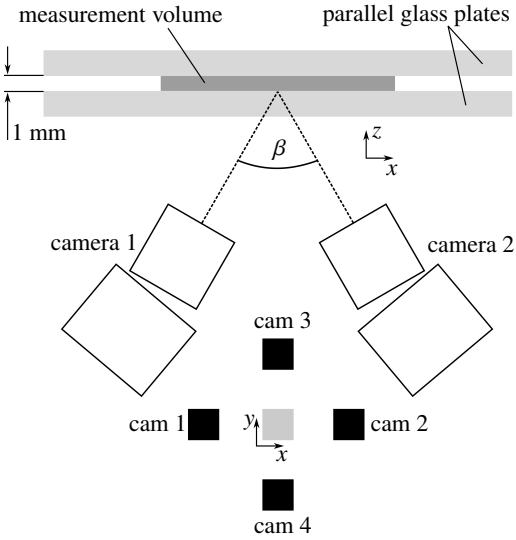

Figure 2.22: Tomographic PTV set-up

distribution

$$u_{\mathrm{p}}(z) = u_{\max}\left(1 - 4\frac{z^2}{d_z^2}\right) \tag{2.17}$$

where $u(z)$ is the local velocity at z, and d_z is the channel height. The maximum flow velocity at $z = 0$ at the channel center, is denoted by $u_{\max}$. The Reynolds number is calculated as follows: $Re = \bar{u}\, d_h/\nu$, with the hydraulic diameter, $d_h = 4A/U$, where A is the area of the cross section of the channel, U is the circumference of the cross section, and ν is the kinematic viscosity. The mean flow velocity is calculated as $\overline{u} = \frac{2}{3}u_{\max}$. In the following, velocities are normalized with respect to $u_{\max}$. Depth locations are normalized with the channel height d_z, such that the upper wall is closer to the camera at $z = 0.5$ and the lower wall is at $z = -0.5$. This normalization enables a straightforward comparison of the measurement results.

Measured flow field

Figure 2.23 gives an overview of the measured flow profiles for a single 2×2×1 mm^3 section of the measurement domain, where the scattered dots denote the measured velocities and their corresponding z locations. The solid lines denote the parabolic fit of the data, using Eq. (2.17). A good qualitative agreement between experiment and the theoretical solution can be observed for both measurement techniques. Defocusing PTV shows a stronger scattering of the data points, especially towards the lower wall at $z = -0.5$, as seen in Fig. 2.23(a)). This is due to the decreasing SNR of the particles images, since the particle image diameter increases by roughly 10 pixel from wall to wall. Thus, the same light intensity is distributed over a larger area on the sensor, yielding a lower signal, which decreases the accuracy of the particle image geometry determination. Exemplary, Fig. 2.24 provides three intensity distributions of cuts through particle images with different diameters. Tomographic PTV does not have a z dependency of the SNR, since all particles are in focus for this small measurement depth.

Altogether, tomographic PTV performs better, since it employs four views of the measurement volume from different angles. In particular, the particle z locations are determined with lower uncertainty, while the single camera technique make use of the defocused particle image geometry to derive the depth information. The latter procedure is more affected by low SNRs or changing illumination conditions between the two light pulses. A quantitative analysis of these observations is given in the subsequent section.

Uncertainty of *u*

First, the uncertainty of the main flow velocity, i.e. in x direction, is estimated. Therefore, the measured and then normalized velocities u are compared to their ideal values u_{p} of the parabolic flow profile. In other words, for a certain data point with a normalized

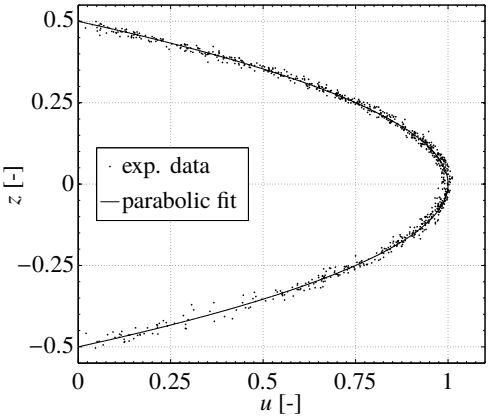

(a) defocusing PTV

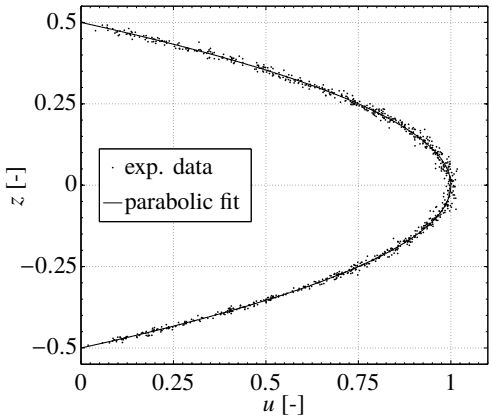

(b) tomographic PTV

Figure 2.23: Measured velocity profiles in a 2×2×1 mm^3 section of the measurement volume for defocusing PTV (a) and tomographic PTV (b)

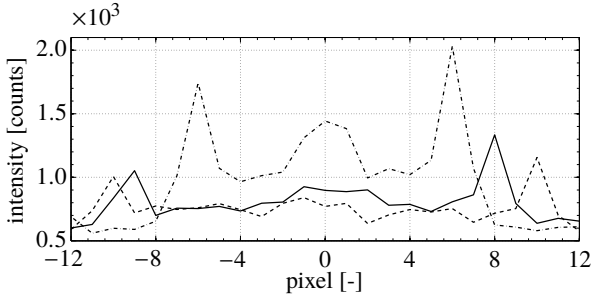

Figure 2.24: Intensity distributions of cuts through three defocused particle images with different diameters

depth location z, the ideal velocity is calculated by Eq. (2.17), which yields a deviation Δu, denoting the absolute difference between the ideal and the measured velocity at this z location. If the measured z location is either larger than $z = 0.5$ or lower than $z = -0.5$, the ideal velocity value is set to zero. Following this paradigm, for n data points, the velocity uncertainty is calculated by

$$E_u = \sqrt{\frac{\sum_{i=1}^{n} \left(u_\mathrm{p}(z_i) - u_i\right)^2}{n-1}} \tag{2.18}$$

where tomographic PTV yields an uncertainty of $E_u = 0.0159$ and an average deviation of $\overline{|\Delta u|} = 0.0119$. As expected, the single camera defocusing PTV technique has a larger uncertainty with $E_u = 0.0243$ and an average deviation of $\overline{|\Delta u|} = 0.0170$. However, it should be noted that the multi-camera technique uses four times more the information to lower the uncertainty by only a factor of 3/2.

Figure 2.25 provides a closer look at the z dependency of E_u. Therefore, the data points are binned in z direction in 21 equally spaced bins, where E_u is calculated for each bin separately. The location of the lowest velocity uncertainty is in the channel center at $z = 0$, where the errors lie in the range of $E_u = 0.011 - 0.015$. At a maximum displacement of 10 pixels, an error of $E_u = 0.011$ corresponds to a displacement uncertainty of 0.11 pixel. Thus, compared with typical PIV uncertainties, these 3D techniques perform very well (Piirto et al. (2005)).

It has to be noted, that 3D imaging has more sources of error, such as the systematic calibration error, the misalignments of cameras due to vibrations, and for multi-camera techniques a less advantageous viewing angle of the measurement volume. The accuracy of the particle image center location determination is constant, such that E_u increases relative to the maximum normalized velocity for particles further away from $z = 0$. For the tomographic approach, the error distribution along z is relatively symmetric with respect to $z = 0$. Slight differences might appear due to aberrations, caused by the imaging optics

and the relatively large glass plate thickness of 20 mm. The calibration function can only account for these influences to a certain extent. Tomographic PTV yields uncertainties of up to $E_u = 0.035$ near to the wall.

Unlike tomographic PTV, defocusing PTV shows a non-symmetric uncertainty distribution E_u along the measurement depth. Towards the wall further away from the camera, at $z = -0.5$, the uncertainty yields up to $E_u = 0.061$, while at the opposite wall, the uncertainty increases to only $E_u = 0.036$. It was mentioned before, that the SNR of the particle images decreases with the square of the particle image radius, further away from the camera, such that the particle image diameter determination is more error-prone and less accurate. This directly affects the uncertainty of the velocity measurement, since the particle z locations are scattered stronger, which yields larger Δu values, especially in regions with large velocity gradients.

Uncertainty of the displacements in *y* and *z* direction

For a planar Poiseuille flow, the velocities in y and z direction are supposed to be zero. Thus, the displacement uncertainties in the respective directions can be directly calculated by the standard deviations of the measured displacements ΔY and ΔZ. Figure 2.26 gives an overview of this standard deviation for defocusing and tomographic PTV, where the uncertainty σ is expressed as a pixel value at different z locations. Thus, for the z component of the displacement, the physical displacement Δz [µm] is normalized with the reproduction scale [µm/pixel] of the two optical set-ups, yielding ΔZ [pixel]. Tomographic PTV yields uncertainties around $\sigma_{\Delta Z} \approx 0.12 - 0.18$ pixel and defocusing in the range of $\sigma_{\Delta Z} \approx 0.56 - 0.73$ pixel. Again, the increasing SNR of the particle images towards $z = 0.5$ results in lower uncertainties in the displacement determination.

For $\sigma_{\Delta Y}$, the uncertainty of defocusing PTV is much lower, with values slightly above 0.05 pixel. The ΔY uncertainties are comparable to those of 2D PIV, since the optical set-up is similar. Apparently, the particle image center location determination is much less affected by low SNRs and changing illumination conditions between the two frames, compared with the diameter estimation. A slight improved of the uncertainty towards $z = 0.5$ is visible. For tomographic PTV, $\sigma_{\Delta Y}$ is lower than $\sigma_{\Delta Z}$ due to the viewing angle of $\beta = 60°$, which favors the y direction. At $\beta = 90°$ the uncertainties are supposed to be equal. The uncertainty yields values around $\sigma_{\Delta Y} \approx 0.09 - 0.13$ pixel.

The uncertainty estimation of E_u on the one side and $\sigma_{\Delta Y}$ and $\sigma_{\Delta Z}$ on the other side is of a different nature. The latter two provide a measure of the actual displacement determination uncertainty, which then can be transferred into a velocity uncertainty with the reproduction scale. In x direction, the displacement uncertainty is covered by $\sigma_{\Delta Y}$, since these axes could be switched without changing the set-up.

However, the uncertainty E_u not only contains the uncertainty of the displacement, but in addition it accounts for the uncertainty of the z location determination of this displacement, since it compares the measured data to the theoretical solution. Thus, the latter analysis provides a more realistic measure of the measurement uncertainty of flow

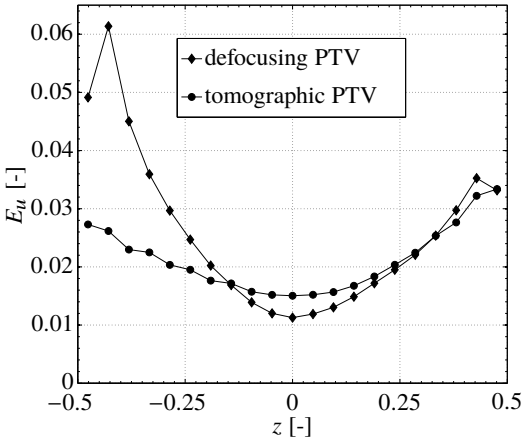

Figure 2.25: Measurement uncertainty of the main flow velocity u, in x direction

fields in wall-bounded domains with small measurement depths, where strong velocity gradients in z direction are present.

For defocusing PTV, the minimum uncertainty values at $z = 0$ yield around $E_u = 0.011$, corresponding to a value of 0.11 pixel, at a maximum displacement of 10 pixels. This is a higher value than the pure in-plane displacement uncertainty of $\sigma_{\Delta Y} \approx 0.06$ pixel. Hence, the lower $\sigma_{\Delta Y}$ values cannot be achieved for the actual velocity field determination, where the location of the measured velocity is a factor as well. Negative influences on E_u might also be the result of a fluctuating pressure at the inlet and a non-ideal velocity profile, since both are causing deviations from the theoretical flow solution. Note that E_u only applies for 3D measurement techniques. In a 2D analysis there is no z coordinate, and such $\sigma_{\Delta Y}$, or $\sigma_{\Delta X}$ respectively, is both, the uncertainty of the displacement as well as the uncertainty of where this track is located in the measurement plane.

Altogether, defocusing PTV and tomographic PTV are capable of measuring a planar Poiseuille flow with uncertainties below 2.5%, relative to the maximum velocity, while the uncertainty analyses emphasizes the necessity of both, measuring the displacement and determining the location of this displacement very accurately. The four-camera technique outperforms the single camera defocusing PTV technique in the accuracy of the particle location determination.

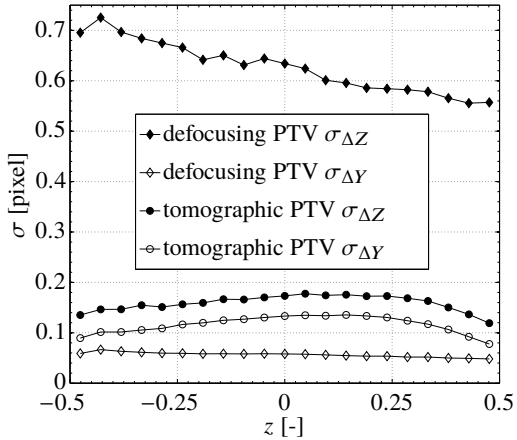

Figure 2.26: For a planar Poiseuille flow the velocities in y and z direction are supposed to be zero. Thus, the standard deviations of the measured displacements in these directions provide a measure for the displacement uncertainty.

2.3 Concluding remarks

In this chapter, single camera volumetric flow velocimetry approaches were introduced. They offer the capability of measuring flows in the presence of vibrations and with a limited optical access. The APTV measurement technique is a more versatile technique compared to the defocusing PTV approach, since the measurement depth can be larger. Using APTV, the resolution in depth direction is significantly better than typical light sheet thicknesses ($\sim$ 1 mm) of 2D PIV measurements, even for measurement depths around 50 mm. It allows for measuring flows with strong velocity gradients in z direction, with uncertainties of the measured velocities comparable to those in PIV.

While defocusing PTV is limited to measurement depths in the low millimeter range, it offers the possibility of an *in situ* calibration, enabling flow measurements in domains, where no target can be placed. Compared to the more complex tomographic PTV technique, the measurement uncertainty is only around 50% larger, while employing only one camera and not four.

Both techniques, APTV and DPTV, with their complementary features, open new fields of application for particle imaging. In particular, this applies to fields where particle imaging has not been employed to a great extent.

3 Multi-camera techniques

Multi-camera techniques for optical flow measurements are significantly more complex than single camera approaches. They are sensitive to misalignments of the cameras, induced by vibrations, for instance. Furthermore, the optical access requirements are much higher and they generate a significantly larger hardware utilization. Nonetheless, multi-camera techniques offer some capabilities, making them the desired choice for 3D flow measurements, besides their drawbacks. Compared to single camera techniques, the uncertainty of the particle z location determination is significantly better, due to viewing the measurement volume from different angles. With an increased seeding density, multi-camera techniques allow for capturing complex flow structures in three dimensions.

This chapter focuses on measurement approaches for applications, where multi-camera techniques have not been employed to a great extent. In the first part of this chapter, in section 3.1, a stereoscopic 3D-PTV approach is introduced, which is suitable for applications with small measurement depths. An application for the measurement of a Tesla turbine rotor flow, using a non-intrusive calibration procedure, is given in section 3.2. Parts of section 3.1 and 3.2 were published in Fuchs et al. (2016d) and Schosser et al. (2016a). Figures and text are adjusted to fit the format of this thesis and to improve the readability.

Section 3.3 introduces a combined astigmatic 3D-PTV approach. Astigmatic imaging is used as a predictor to match corresponding particle images on the different camera sensors. Unlike the stereoscopic 3D-PTV approach, the combined technique is better suited for larger measurement depths, where the search area for corresponding particle images on the other sensor is significantly larger. Parts of section 3.3 were published in Fuchs et al. (2014a) and Fuchs et al. (2014c). Figures and text are adjusted to fit the format of this thesis.

Section 3.4 introduces a volumetric tracking approach, allowing for the measurement of densely seeded flows with high spatial resolution. This approach follows the idea of the astigmatic 3D-PTV method, only that here a tomographic predictor is used to match corresponding particle images. I.e. the tomographically reconstructed volume is used to match corresponding particle images on at least four camera sensors, such that the particle location can be triangulated. This combined tomographic 3D-PTV approach is tested by means of a synthetic data set and applied for the measurement of a turbulent boundary layer flow, outlined in section 3.5. Parts of section 3.4 and 3.5 were published in Fuchs et al. (2016a) and Fuchs et al. (2016b). Again, figures and text are adjusted to fit the format of this thesis.

3.1 Stereoscopic 3D-PTV

The tracking of particles in a volume is not a new concept. In fact, it was introduced by Sheu et al. (1982) in the early 1980's as a stereoscopic set-up. Chang et al. (1984) took on the volumetric tracking idea and implemented an automated, digital image processing procedure. Later implementations of 3D-PTV, using more than two cameras, include the work of Maas et al. (1993), Malik et al. (1993), Suzuki & Kasagi (2000), and Lüthi et al. (2005). All these applications are based on a time-resolved measurement of water flows. However, in many fluid mechanical applications it is not feasible to record a time-series, especially at larger flow velocities. For water flows, the feasibility of double-frame 3D-PTV measurements is proven by Nishino et al. (1989).

Generally, tracking yields a better spatial resolution than cross-correlation approaches, due to the spatial averaging by the interrogation windows used in cross-correlation (Kähler et al. (2012a)). Tomographic PIV, for instance, is not very suitable for the measurement of turbulent boundary layers flows, where a strong velocity gradient near the wall is present (see Atkinson et al. (2010), Elsinga et al. (2011), and Rafati & Ghaemi (2016)). This stereoscopic 3D-PTV approach focuses on double-frame measurements, where the measurement depth is small compared to the x and y dimensions of the measurement volume.

The limited measurement depth is owed to employing only two views of the measurement volume. With a large depth, the search area for the corresponding particle images on the other sensor is too large, yielding ambiguities. Rochlitz et al. (2015) utilized this 3D-PTV approach for the measurement of a turbulent water flow in a high aspect ratio cooling duct used for miscellaneous cooling purposes, such as in rocket propulsion. The measurement depth and therefore the duct depth was 6 mm. The stereoscopic 3D-PTV techniques ability for resolving strong velocity gradients in air flows is proven by the measurement of a Tesla turbine rotor flow with a gap height of only 0.5 mm, including a non-intrusive calibration approach.

In 3D-PTV, the particle location is triangulated from at least two corresponding particle images on different cameras, viewing the measurement volume from different angles. As described in more detail in the introduction, larger seeding concentrations and larger measurement depths make it increasingly difficult to find corresponding particle images, since the matching becomes ambiguous. However, for small measurement depths, a stereoscopic imaging system is sufficient for volumetric flow measurements, due to the relatively small search area for a corresponding particle image on the other camera sensor. In the following, a detailed description of the calibration of a stereoscopic 3D-PTV system is given.

3.1.1 Calibration and particle location determination

The calibration of the 3D-PTV system requires a set of calibration points, which can be derived from a calibration target with dots, grid intersections, or any other geometrical shape at known physical locations $\boldsymbol{x} = (x, y, z)$. After imaging the calibration target, the

center locations $\boldsymbol{X}_i = (X_i, Y_i)$ of these shapes are estimated for i cameras, completing the required calibration information. According to Hartley & Zisserman (2004), the fundamental matrix F of the stereoscopic system is calculated from the corresponding calibration points, such that it satisfies

$$\boldsymbol{X}_1^{\mathrm{T}} F \boldsymbol{X}_2 = 0. \tag{3.1}$$

The fundamental matrix is estimated in two steps. First, an initial linear solution of F is calculated using the normalized 8-point-algorithm, introduced by Longuet-Higgins (1981). In a second step the camera matrices, P_1 and P_2, are determined. If P_1 is defined as a 3×4 identity matrix, P_2 is computed from the epipolar line and F. Using P_2, the sensor position $\hat{\boldsymbol{X}}$ of the known points is estimated. To optimize P_2, the function

$$\sum_{j=1}^{n} d\left(\boldsymbol{X}_{1j}, \hat{\boldsymbol{X}}_{1j}\right)^2 + d\left(\boldsymbol{X}_{2j}, \hat{\boldsymbol{X}}_{2j}\right)^2 \tag{3.2}$$

describing the geometric distance between a point $(\boldsymbol{X}_1, \boldsymbol{X}_2)$ and its estimation $\left(\hat{\boldsymbol{X}}_1, \hat{\boldsymbol{X}}_2\right)$, is minimized by means of a non-linear Levenberg-Marquardt algorithm. Having determined the camera parameters, the spatial particle locations can be triangulated.

These resulting non-metric coordinates $\boldsymbol{x}_v$ need to be transferred to physical coordinates $\boldsymbol{x}$, where polynomials serve as mapping functions, here exemplary for the x coordinate

$$x = \sum_{i,j,k} c_{i,j,k}\, x_v^i\, y_v^j\, z_v^k, \quad i + j + k \leq t \tag{3.3}$$

where $c_{i,j,k}$ denotes the coefficients of the polynomial. For the y coordinate and the z coordinate, the polynomial function is formulated accordingly. Depending on the amount of optical aberrations and other distortions, the order, t, of the polynomial can be adjusted. The determination of the coefficients of the polynomials is conducted according to the procedure for the APTV mapping functions, described in section 2.1.4.

However, the so-called camera pinhole model, introduced by Tsai (1987), offers an alternative, more straightforward calibration procedure. Using the latter approach, the camera matrices P_1 and P_2 are estimated such that it is possible to directly triangulate the spatial particle locations from corresponding particle images. For small measurement depths this approach is sufficient.

Before being able to perform the triangulation, the sensor locations of the particle images have to be estimated and corresponding particle images on the two sensors need to be determined. To do so, the recordings are first preprocessed, with a subtraction of an average image of all recordings as the first step, to eliminate background reflections. Depending on the image quality, a intensity threshold can then be applied to the images, to detect the individual particle images. If still strong reflections are present or the SNR is distributed non-homogeneously over the image, additional preprocessing steps might be necessary. These include an intensity normalization, subtraction of local minimum intensities to better distinguish particle images from background, among other steps. Here

also, the final step is an intensity threshold to detect the particle images.

After the detection, the sub-pixel particle image locations are estimated by a least squares approximation of a 2D Gaussian intensity distribution (Raffel et al. (2007))

$$I(X,Y) = I_0 \cdot \exp\Big[-8 \cdot \Big(\frac{(X-X_0)^2}{d_{\tau_X}^2} + \frac{(Y-Y_0)^2}{d_{\tau_Y}^2}\Big)\Big] \tag{3.4}$$

where the coefficients X_0 and Y_0 denote the particle center location, I_0 denotes the intensity at peak height, and d_{τ_X} and d_{τ_Y} denote the Gaussian peak width in the respective direction. Using the sensor locations, corresponding particle images are matched by means of epipolar geometry. Therefore, the next step is to calculate the epipolar line, i.e. the slope and the y intercept, on the second sensor for each individual particle image on the first sensor:

$$E = F\boldsymbol{X}. \tag{3.5}$$

Possible particle image correspondences are searched for in the proximity of the epipolar line, as illustrated in Fig. 1.4(b). The length of the search area is confined by the measurement depth.

When a uniquely matching particle image is found in the search area, the spatial particle location is triangulated by means of the so-called optimal triangulation method, introduced by Hartley & Sturm (1997). Finally, the velocities are estimated from the spatial particle locations by means of volumetric particle tracking algorithms from double-frame, multi-frame, or time-resolved data sets. If vibrations and movement of the camera occurs during measurements, this can be corrected for each frame by point correspondences derived from particles in the flow, which is comparable to the self-calibration used in tomographic PIV (Wieneke (2008)). However, it has to be pointed out that a self-calibration procedure can only correct for the alignment of the cameras with respect to each other. The misalignment of the cameras with respect to the calibration target and therefore the location in the measurement domain cannot be corrected for. As outlined in the following, the 3D-PTV velocimetry approach allows for very accurate flow measurements.

3.1.2 Measurement uncertainty

To prove the feasibility of the stereoscopic 3D-PTV approach for accurate flow measurements at small measurement depth, a planar Poiseuille flow between two parallel glass plates with a distance of 1 mm is investigated, where the measured velocities are compared to the theoretical solution. In addition, the influence of the particle image SNRs is analyzed.

Experimental set-up

For this uncertainty analysis, the same experiment as introduced for the defocusing PTV approach is used. Thus, for further information on the experiment and the theoretical flow

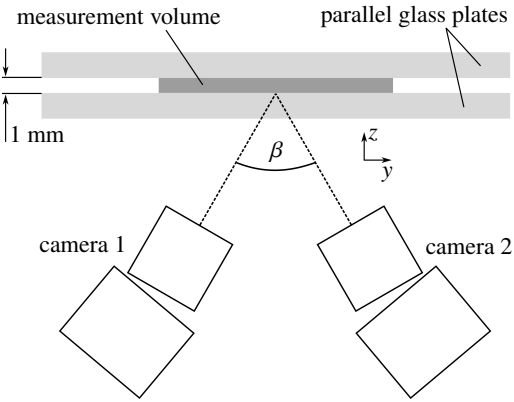

Figure 3.1: Stereoscopic 3D-PTV set-up

field it is referred to subsection 2.2.5.

The 3D-PTV imaging set-up is illustrated in Fig. 3.1. The angle between the two cameras, equipped with f = 50 mm *Zeiss* macro objective lenses at aperture number of $f_\#$ = 5.6 and Scheimpflug adapters, is $\beta = 60°$. The point correspondences, required for the calibration, are derived from a dotted dual-plane target. For this stereoscopic 3D-PTV analysis, two different data sets are analyzed. Configuration A employs two *PCO 4000* cameras with an analog digital conversion factor of 3.3 electrons per count and with a random mean square (RMS) of the read out noise of 14 electrons. The resulting particle image SNR is 106 at a magnification of $M = 0.30$ and a reproduction scale of 30.0 µm/pixel in the image center.

Configuration B employs *PCO edge* sCMOS cameras to record the illuminated particles. The 16 bit camera has an analog digital conversion factor of 0.46 electrons per count and the RMS of the read out noise is 2.5 electrons. The SNR of the particle images is 478 for configuration B, at a magnification of $M = 0.23$ and a reproduction scale of 27.7 µm/pixel in the image center.

Measured velocity field

Figure 3.2 gives an overview of the measured normalized flow profiles for a single 2×2×1 mm^3 section of the measurement domain, where the scattered dots denote the measured velocities and their corresponding z locations. The solid lines denote the parabolic fit of the data, using Eq. (2.17). A good qualitative agreement between experiment and the theoretical solution can be observed for both data sets.

There does not seem to be a large difference between the two data sets in terms of the

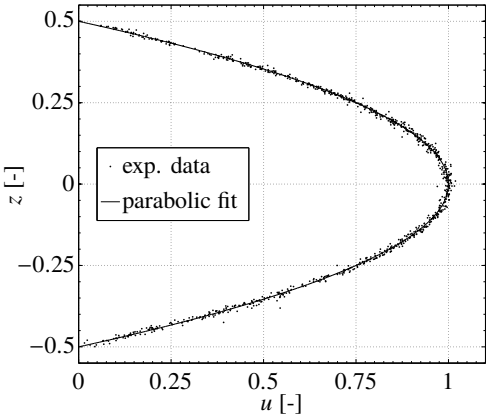

(a) configuration A – *PCO 4000*

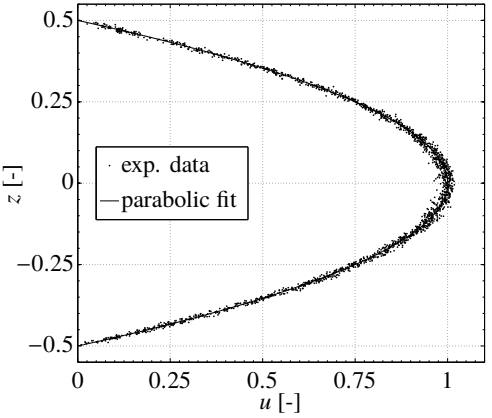

(b) configuration B – *PCO edge* sCMOS

Figure 3.2: Measured velocity profiles in a 2×2×1 mm^3 section of the measurement volume using 3D-PTV.

scattering of the data points. However, a closer look at the actual quantitative uncertainties is given in the following.

Uncertainty of *u*

First, the uncertainty of the main flow velocity u in x direction is estimated. Therefore, the measured and normalized velocities u are compared to their ideal values of the parabolic flow profile u_p. In other words, for a certain data point with a normalized depth location z, the ideal velocity is calculated by Eq. (2.17), which yields a deviation Δu, denoting the absolute difference between the ideal and the measured velocity at this z location. If the measured z location is either larger than 0.5 or lower than -0.5, the ideal velocity value is set to zero. Following this paradigm, for n data points, the velocity uncertainty is calculated by Eq. (2.18).

The uncertainty of 3D-PTV configuration A yields $E_u = 0.0149$ at an average deviation of $\overline{|\Delta u|} = 0.0108$. Configuration B performs better with an uncertainty of $E_u = 0.0125$ and an average absolute deviation of $\overline{|\Delta u|} = 0.0099$. Figure 3.3 provides a closer look at the z dependency of E_u. The location of the lowest velocity uncertainty is in the center at $z = 0$, where the errors lie in the range of $E_u \approx 0.010$. At a maximum displacement of 10 pixels, an error of $E_u = 0.010$ corresponds to a displacement uncertainty of 0.1 pixel. Thus, compared with typical PIV uncertainties, as outlined by Piirto et al. (2005), the 3D techniques perform very well. It has to be noted, that 3D imaging has more sources of error, such as the systematic calibration error, the misalignments of cameras due to vibrations, and most often a less advantageous viewing angle of the measurement volume.

Since the accuracy of the particle image center location determination is constant, E_u increases relative to the maximum normalized velocity for particles further away from the channel center due to the velocity gradient. The error distribution along z is relatively symmetric with respect to $z = 0$. Slight differences might appear due to aberrations, caused by the imaging optics and the relatively large thickness of the glass plate of 20 mm. The calibration function can only account for these influences to a certain extent. Configuration A yields an uncertainty of up to $E_u = 0.036$ near to the wall, whereas the uncertainties of configuration B are somewhat smaller, with values up to $E_u = 0.018$.

Altogether, 3D-PTV configuration B shows a significantly better performance at a similar reproduction scale. This is mainly due to a better image quality in terms of the particle image SNR. For the *PCO 4000* camera, the illumination intensity is limited, since blooming occurs due to scratches in the glass plates. The blooming can damage the camera sensor. The *PCO edge* sCMOS camera allows for much higher illumination intensities, since the camera is not affected by blooming. The *PCO edge* data, with a SNR of 478 shows lower uncertainties than the *PCO 4000* data, with a SNR of only 106.

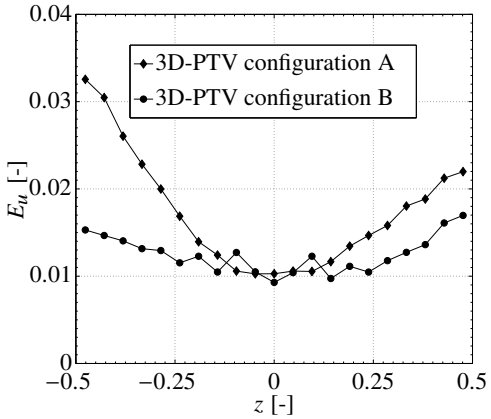

Figure 3.3: Measurement uncertainty of the main flow velocity u in x direction

Uncertainty of the displacements in *y* and *z* direction

In a second analysis, the out-of-plane motion uncertainty and the uncertainty of the motion vertical to the main flow direction is estimated. This is a straightforward procedure, since the displacement in z direction is supposed to be zero within the measurement volume, where a planar Poiseuille flow is expected. The same applies for the velocity in y direction. Thus, the error is directly calculated by the standard deviation of the displacements ΔY, and ΔZ of each track. Figure 3.4 gives an overview of this standard deviation for the two 3D-PTV configurations, where the uncertainty σ is expressed as a pixel value at different z locations. For the z component of the displacement, the physical displacement Δz [µm] is normalized with the reproduction scale [µm/pixel] of the different optical set-ups, yielding ΔZ [pixel]. Again, configuration B performs better with $\sigma_{\Delta Z}$ values slightly above 0.05 pixel. Configuration A, yields uncertainties around 0.15 to 0.25 pixel.

The uncertainty in y direction is lower than for the z direction, since the measurement domain is imaged at angles of $\beta = 60°$, which favors the y direction. At $\beta = 90°$ the uncertainties are supposed to be equal. The uncertainty $\sigma_{\Delta Y}$ yields values as low as 0.03 pixel for 3D-PTV configuration B. Note, that the particle image quality is very good. Along with a high SNR, the particle image diameter was around 4 pixel, which allows for an accurate 2D Gaussian fit of the particle image center location. Furthermore, the seeding density was low, such that particle image overlaps seldom occurred. Measurements in a less generic environment, where vibrations, reflections, lower SNRs, among other negative influences are present, certainly will not allow for such low uncertainties. Configuration A with lower SNRs yields uncertainties around 0.10 to 0.14 pixel in y direction.

Again the characteristics of the two different uncertainty analyses are discussed in more detail. The uncertainties $\sigma_{\Delta Y}$ and $\sigma_{\Delta Z}$ provide a measure of the actual displacement determination uncertainty, which then can be transferred into a velocity uncertainty.

The procedure to determine the uncertainty E_u, i.e. the uncertainty of the measurement of the main flow velocity, in x direction, is of a different nature. This analysis not only contains the uncertainty of the displacement, but in addition it accounts for the uncertainty of the z location determination of this displacement, since it compares the measured data to the theoretical solution. Thus, the latter analysis provides a more realistic measure of the measurement uncertainty of flow fields in domains with small measurement depths, where strong velocity gradients in z direction are present. The minimum uncertainty values at the channel center yield around $E_u = 0.01$ and more, which corresponds to a value of 0.1 pixel, at a maximum displacement of 10 pixels. The lower $\sigma_{\Delta Y}$ values, around 0.03 pixel, cannot be achieved for the actual velocity field determination. Larger E_u values might also be the result of a fluctuating pressure at the inlet and a non-ideal velocity profile, since both are causing deviations from the theoretical flow solution. Note that E_u only applies for 3D measurement techniques. In a 2D analysis there is no z coordinate, and such $\sigma_{\Delta Y}$, or $\sigma_{\Delta X}$ respectively, is both, the uncertainty of the displacement as well as the uncertainty of where this track is located in the measurement plane.

Altogether, both 3D-PTV configurations are capable of measuring flows in domains with small depths with uncertainties below 1.6%, relative to the maximum velocity, while the uncertainty analyses emphasizes the necessity of both, measuring the displacement, and determining the location of this displacement very accurately. The benefit of high SNRs is clearly visible in the uncertainty values.

It has to be noted, that the presented uncertainty estimations only apply for small measurement depths. At larger measurement depths, more ambiguities arise, due to the larger search area on the sensor. These ambiguities cannot be resolved entirely, especially at higher seeding densities, leading to increased uncertainties. For larger measurement depths, it is referred to section 3.3, where astigmatic imaging is used to resolve these ambiguities to allow for stereoscopic 3D-PTV measurements.

In the following section, an application of 3D-PTV for the measurement of a Tesla turbine rotor flow is outlined.

3.2 Measurement of Tesla turbine rotor flow

The measurement environment of the Tesla turbine perfectly suits the stereoscopic 3D-PTV approach presented in the previous section. First, the optical access is limited, allowing for the use of two cameras only. Second, the measurement depth is small with 0.5 mm, whereas the extension in x direction is large in comparison, with 12 mm. Third, the strong velocity gradient in z direction requires a high spatial resolution, which favors tracking techniques. However, the main focus of this section lies on the description of a

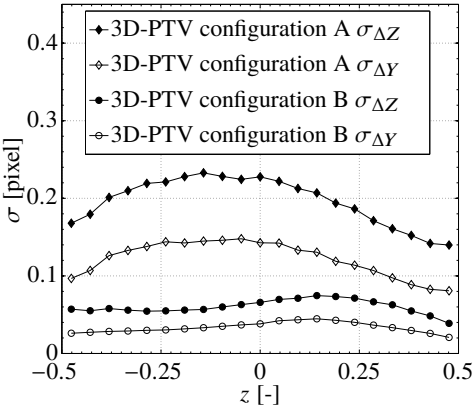

Figure 3.4: For a planar Poiseuille flow the velocities in y and z direction are supposed to be zero. Thus, the standard deviations of the measured displacements in these directions provide a measure for the respective displacement uncertainty.

non-intrusive calibration procedure. This procedure is necessary, since it is not possible to place a calibration target within the measurement volume.

Tesla turbines are friction-type turbines, where the momentum exchange between fluid and rotor generates torque (Schosser et al. (2014)). The rotor, characterized by its simple and robust design, consists of several circular, parallel, flat, and equidistant co-rotating disks with gap heights in the sub-millimeter range and an outlet in the hollow rotor shaft. The flow, delivered by guide vanes, takes a spiral path towards the outlet. So far, theoretical, numerical, and analytical investigations of the Tesla turbine rotor flow were conducted, while these analyses only apply for incompressible laminar flows (see Romanin & Carey (2011) and Guha & Sengupta (2014)). However, they lack experimental validation. Previous experimental studies analyzed the turbine performance and efficiency, but not the flow (Lemma et al. (2008)).

3.2.1 Experimental set-up

Figure 3.5 gives an overview of the generic Tesla turbine test facility, which is described in detail in Schosser (2016), and the optical set-up. The purpose of this test facility is the study of the flow in Tesla turbine rotors at different operational points. The rotor consists of two parallel, co-rotating disks with a gap height of 0.5 mm and a diameter of 125 mm. The cameras have to look through two windows to image the particles within the measurement domain. The pressurized turbine housing features a rectangular optical

access window with a thickness of 8 mm, as shown in Fig. 3.6. The second circular optical access window is directly integrated into the rotor, extending from the radii 41 mm to 114 mm. The circular window is integrated in both the upper and the lower rotor disk, where the actual measurement domain is located between these windows. These windows have a thickness of 8 mm as well.

Two *PCO 2000* cameras with 60 mm objective lenses, each combined with a 2× magnifying teleconverter, were used for imaging. To account for astigmatic aberrations caused by the angled view through the two optical access windows, the aperture is set to $f_\# = 16$, yielding a larger depth of focus. The reproduction scale in the image center yields 11 µm/pixel at a magnification of $M = 0.67$. The measurement volume, sized 12×4×0.5 mm^3, is illuminated through the rotor shaft with a double-pulse Nd:YAG laser with a maximum energy of 2×30 mJ. The flow was seeded with standard DEHS particles, while the seeding concentration is relatively limited, due to the rather large particle images. They yield diameters around 8 pixel, due to the angled view through the relatively thick optical access windows and the high magnification. However, a low seeding concentration leads to fewer ambiguous particle image matches, which is beneficial for this stereoscopic 3D-PTV application.

The pulsed laser beam is deflected by a fixed, rotating mirror, mounted at the center of rotation at the rotor outlet. Despite the low seeding density, the mirror contaminates quickly and is therefore cleaned after each run. Due to the limited available space, it is not possible to use any optics to set up a light sheet for the illumination of the gap. Instead, the unmodified laser beam, with a diameter of roughly 4 mm, illuminates the measurement volume.

3.2.2 Non-intrusive calibration

Volumetric velocimetry techniques rely on a proper calibration procedure to measure the flow velocities with high resolution and accuracy. It is the standard procedure to image a calibration target with specific geometrical shapes within the measurement volume to derive the required calibration information. For 3D techniques, the target needs to be imaged at a minimum of two depth locations, unless a dual-plane target is used. However, it is not always feasible to place a calibration target within the measurement volume, since the dimensions might be too small for the target. Furthermore, the measurement domain might be inaccessible without a major disassembly of the test facility. Moving the optical equipment can make a calibration procedure unusable, because of misalignments in the assembly. Typically, these challenges occur in fields like turbomachinery and combustion research and also in the case of this Tesla turbine measurement.

Therefore, a non-intrusive calibration was developed for calibrating 3D imaging systems. It is the intent of this calibration scheme to allow for 3D flow measurements in domains with small depths dimensions, where targets do not fit. This calibration approach utilizes light reflections of a continuous wave (cw) laser at the boundaries of the

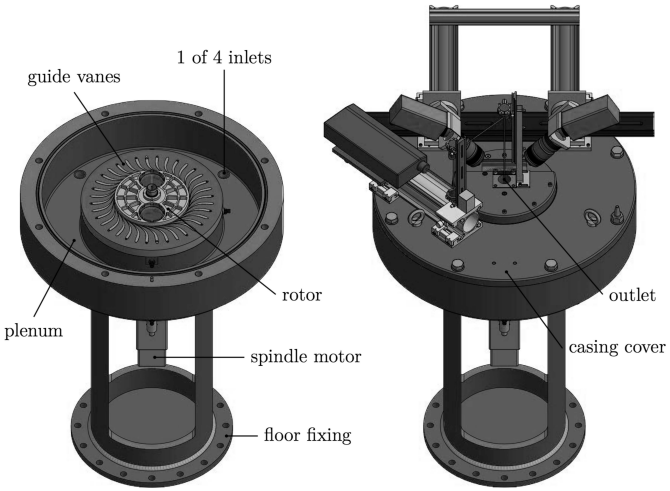

Figure 3.5: Experimental set-up of Tesla turbine rotor flow measurements

measurement volume, as described in the following.

Principle

The calibration of a multi-camera optical system requires a set of calibration points. To determine the calibration points, the following procedure, utilizing light reflections on surfaces, is applied. A cw-laser with a focused beam, perpendicular aligned to the optical access window, illuminates the measurement volume at a certain x and y location with respect to a known reference position, as illustrated in Fig. 3.7(a). Whenever the laser beam impacts a surface, it induces light reflections, which can be imaged with the cameras, as shown in Fig. 3.7(b), yielding an intensity distribution as plotted in Fig. 3.7(c). The two reflections at the locations (x, y, z_0) and (x, y, z_1) in the image center denote the measurement volume boundaries, i.e. the upper and lower wall position along the z direction. When the laser is translated in the xy plane, as illustrated in Fig. 3.8, a set of calibration points is derived, comprising physical coordinates $\boldsymbol{x} = (x, y, z)$ and the respective sensor locations of their reflections $\boldsymbol{X} = (X, Y)$ on the different cameras. Unlike for a regular calibration target, this non-intrusive optical calibration procedure allows for a fully variable number of calibration points, ensuring a sufficient number of points for differing magnifications and fields of view.

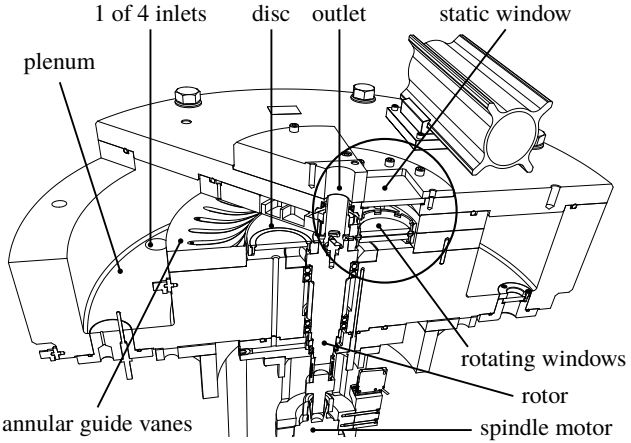

Figure 3.6: Test rig for flow field measurements in a Tesla rotor

However, the light reflections are influenced by imperfect beam profiles, scratches on the optical access windows, material inhomogeneities of the window, among others. Since the sensor locations of the reflections need to be fitted, these imperfections can lead to an inaccurate calibration function. To avoid this effect, a slight rotation of the rotor during the exposure was performed to average out these imperfections.

It is obvious that the fabrication tolerances determine the accuracy of the calibration, since the z coordinates of the calibration points coincide with the measurement domain boundaries. However, the quality of experiments in confined geometries is usually very high, such that a well-known geometrical measure of the experiment (distance between the walls) is well-suited to replace a calibration target. Furthermore, when the windows are curved, the laser beam is deflected. With knowledge of the curvature of the window this deflection can be estimated and such, the corrected coordinates within the measurement volume can be calculated. Moreover, if the back wall is made of an opaque material, e.g. metal, the outlined calibration approach is still feasible.

Practical implementation

The cw-laser used for the calibration can be translated in x and y direction with an accuracy of better than ± 0.01 mm. To focus the laser beam, two spherical lenses with focal lengths of $f = -50$ mm and of $f = +50$ mm, respectively, were used. The resulting beam diameter is approximately 0.1 mm. Altogether, 192 laser positions are approached, yielding 24 rows in y direction and 8 columns in x direction with a spacing of $\Delta x = \Delta y = 0.5$ mm. For each x and y position, five images are acquired at an exposure time of one second

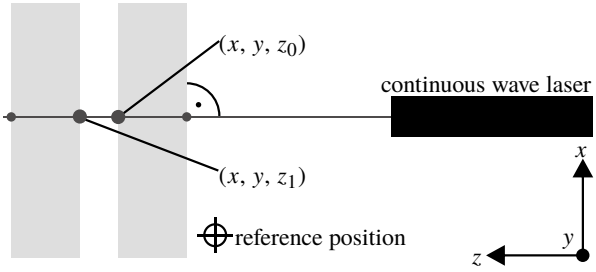

(a) Spatial calibration point coordinates are defined by laser position

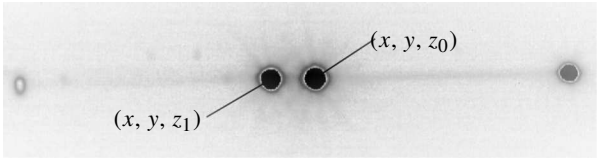

(b) Inverted grayscale image of light reflections

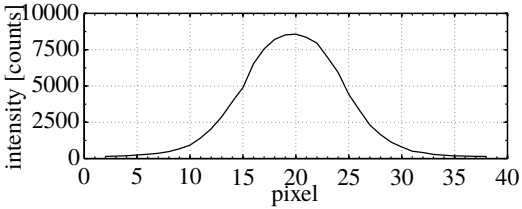

(c) Intensity distribution of a cut through a light reflection

Figure 3.7: Non-intrusive calibration principle

and then averaged. However, an average variation of only 0.1 pixel between the estimated center locations of multiple images appeared, such that a single image at each position would be sufficient. The total calibration time was 15 minutes, including the imaging and the laser translation. The image acquisition in combination with the traverse movement is fully automated and controlled by a personal computer. From this procedure, the physical coordinates (x_i, y_i, z_0) and (x_i, y_i, z_1) and the corresponding sensor coordinates (X_0, Y_0) and (X_1, Y_1) on the two camera sensor are derived.

To estimate the sensor locations of the reflections, first, all intensity values below a threshold of 500 counts are set to zero. Then, the sensor coordinates of the reflections are approximated with sub-pixel accuracy by means of a 2D Gaussian fit. For the fully automated calibration process, spurious reflections have to be eliminated. Thus, the

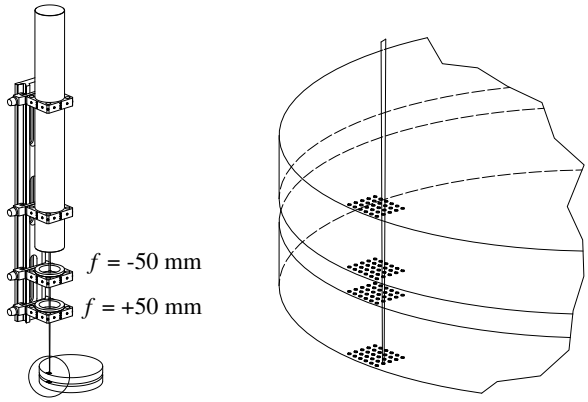

Figure 3.8: Non-intrusive calibration target

algorithm determines the two inner reflections by computing a distance matrix of all reflections found on the sensor. The expected pixel distance within a tolerance range between the reflections in the different z planes is analyzed. Images yielding more than two calibration points, after the outlier detection procedure, are visually inspected by the experimenter. However, this seldom happens.

Uncertainty of the calibration fit

To quantify the calibration fit error, the physical location of the calibration points are mapped back to sensor coordinates. These estimated sensor coordinates are then compared to their sensor locations derived from the calibration images of the reflections. The average absolute residual yields $\overline{R_{\Delta XY}}$ = 0.36 pixel for sensor 1. The second sensor shows a better performance with an average absolute residual of $\overline{R_{\Delta XY}}$ = 0.30. Vice versa, the sensor coordinates, derived from the calibration images, can be triangulated to physical locations. The resulting residual of the known physical calibration coordinates compared to the triangulated locations yield an average absolute residual of $\overline{R_{\Delta xyz}}$ = 3.36 µm. Considering the reproduction scale of 11 µm/pixel in the image center and the average residual on the sensors of roughly 0.3 pixel, this yields a deviation of 3.3 µm expressed with physical coordinates. This is in good agreement with $\overline{R_{\Delta xyz}}$ value.

However, according to the manufacturer, the accuracy of the stage is ±0.01 mm, which is larger than the estimated residual. Therefore, the residual values are plotted with respect to their sensor location on sensor 1 in Fig. 3.9 for plane z = 0 mm and z = 0.5 mm separately. The distribution of the residual values does not show any systematic deviation, which could be attributed to the stage accuracy. Single locations with significantly larger

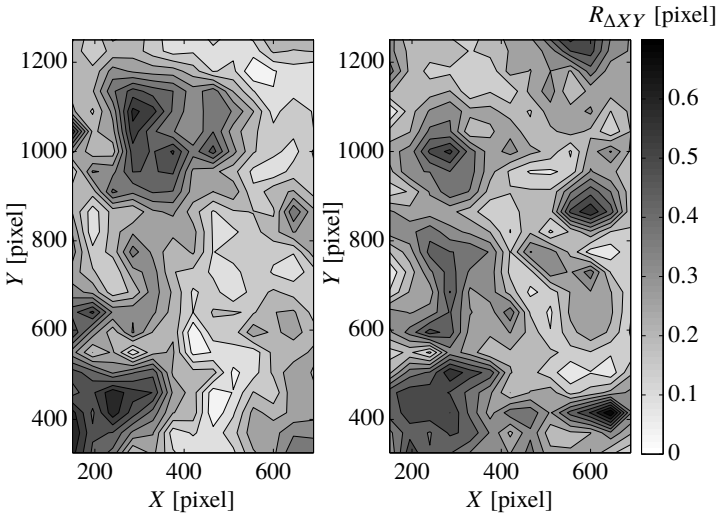

Figure 3.9: Residual of calibration fit error for camera 1, (left) plane z_0 = 0 mm, (right) plane z_1 = 1 mm

deviations might be a result of distortion due to imperfect windows and contamination of the windows. This gives rise to the assumption, that the stage accuracy is somewhat better than denoted by the manufacturer. Otherwise the residuals would be larger.

3.2.3 Flow field

For each operating point, one thousand double-frame recordings are processed as outlined in section 3.1. However, to account for vibrations of the facility, a self-calibration procedure is applied to each single recording. Due to the small measurement depth of only 0.5 mm and the low seeding density, a single correction value is used for the entire image. This correction value is denoted by the maximum value of the triangulation error distribution of all possible triangulations. The standard deviation of the correction values lie in the range of $\delta_{\Delta XY} \approx 0.25$ pixel, while the operating point of the turbine does not show a significant influence. The self-calibration is not performed in the sense of a correction of the calibration function. Instead, the particle image sensor locations are corrected according to the correction value, following the triangulation with the new coordinates. The flow velocities are estimated by means of a probabilistic tracking algorithm (see Ohmi & Li (2000) and Cierpka et al. (2013)).

Since the calibration target provides cartesian coordinates, the velocity field is converted to cylindrical coordinates. This conversion is done by using the well-known reference point and the test rig geometry. Thus the measured velocities only depend on the radial position r and the z location. Exemplary, Figure 3.10(a) shows the measured radial velocity profile for a single operating point at 1000 rpm and a mass flow rate of $\dot{m}$ = 3.5 g/s, at the radial location r = 52.125±0.125 mm. Under these conditions, the profile is laminar and shows a symmetric distribution along the gap height. However, a slight fluctuation of the measured velocities is visible, which is a result of velocity fluctuations at the inlet of the rotor, according to Schosser et al. (2016b).

For a higher mass flow rate of $\dot{m}$ = 16.0 g/s at 5000 rpm, the profile clearly indicates a turbulent profile with steeper gradients near to the wall, as shown in Fig. 3.10(b). The velocity z component reveals information of whether the flow is laminar or turbulent, and also on the turbulence level. The higher turbulence level of the n = 5000 rpm data is nicely visible in Fig. 3.11. Furthemore, if the flow for the n = 1000 rpm case is indeed laminar, $\sigma_{\Delta z}$ gives a measure of the displacement uncertainty, yielding around 2 µm. Normalized with the reproduction scale, this latter value would correspond to an uncertainty of 0.2 pixel, which seems to be realistic, when compared to the uncertainty analysis presented in subsection 3.1.2.

Altogether the measurement results prove the feasibility of the stereoscopic to accurately measure flows with strong velocity gradients under realistic and therefore challenging conditions.

3.3 Astigmatic 3D-PTV

The motivation to combine astigmatic imaging with stereoscopic 3D-PTV is two-sided. It was outlined in section 3.1 that the measurement depth is limited for a stereoscopic 3D-PTV approach, due to arising ambiguities. With an initial estimation of the particle locations by means of astigmatic imaging, corresponding particle images can be matched directly using this information. Thus, from a 3D-PTV point of view, the measurement depth can be increased significantly using a combined approach. Furthermore, APTV locates particles very accurately in the x, and y direction, but the particle z coordinates, i.e. along the optical axis, have larger uncertainties (see section 2.1). Hence, for highly three-dimensional flows, where a precise measurement of the velocity in the z direction is important, it is desirable to extent the single-camera APTV measurement technique.

3.3.1 Principle

Using astigmatic 3D-PTV the three spatial coordinates can be measured with similar accuracy, as illustrated qualitatively in Fig. 3.12. Particles are located by mapping the sensor coordinates of corresponding particle images to physical space by means of third

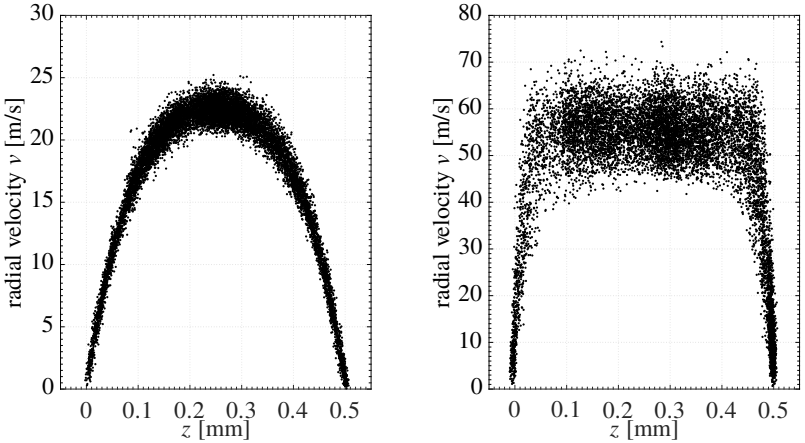

(a) n = 1000 rpm, $\dot{m}$ = 3.5 g/s (b) n = 5000 rpm, $\dot{m}$ = 16.0 g/s

Figure 3.10: Radial velocity distribution at the radius r = 52.125±0.125 mm.

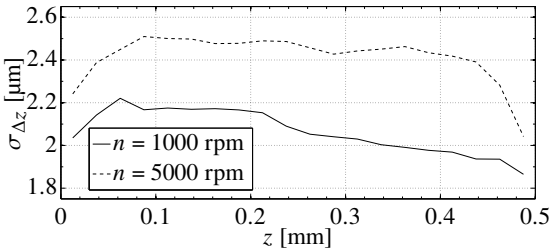

Figure 3.11: standard deviation of the displacement in z direction

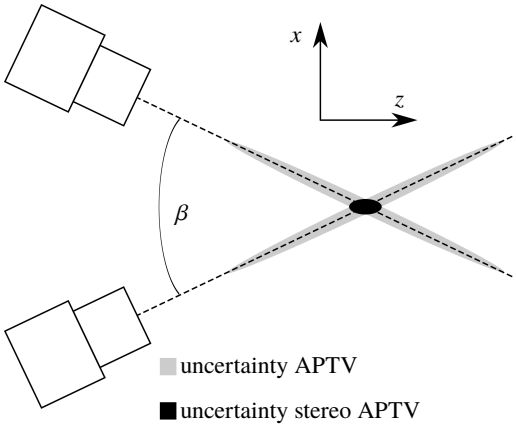

Figure 3.12: Sketch of the qualitative accuracy improvement of the particle z location estimation using astigmatic 3D-PTV compared to single camera APTV. At $\beta = 90°$, the uncertainty is equal for x and z.

order polynomials, or by triangulation, as shown in Fig. 3.13. To uniquely match corresponding particle images on the sensors, astigmatic 3D-PTV utilizes an initial estimation of particle locations by means of single camera APTV processing. Astigmatic 3D-PTV is a redundant measurement technique. Overlapping particle images on one sensor are unlikely to overlap on the second sensor. While coordinate mapping or triangulation is not feasible with overlaps, the particle can still be located from a single view with lower z accuracy. This is advantageous, especially for time-resolved measurements, since it is unlikely that particle tracks get lost.

3.3.2 Calibration and particle location determination

For this combined approached, both the astigmatic imaging system and the stereoscopic imaging system needs to be calibrated. This is best be done by employing a backlight-illuminated pinhole matrix. The calibration of the astigmatic system is outlined in section 2.1. Using triangulation to determine the spatial particle location it is referred to section 3.1. In the following, only the coordinate mapping approach is introduced.

Locating particles using coordinate mapping requires knowledge of the corresponding particle images of the two views of the stereoscopic imaging system. Thus, the input of the third order polynomial mapping functions are the particle image center locations on the two sensors $\boldsymbol{X}_1 = (X_1, Y_1)$ and $\boldsymbol{X}_2 = (X_2, Y_2)$, whereas the output is the particle location

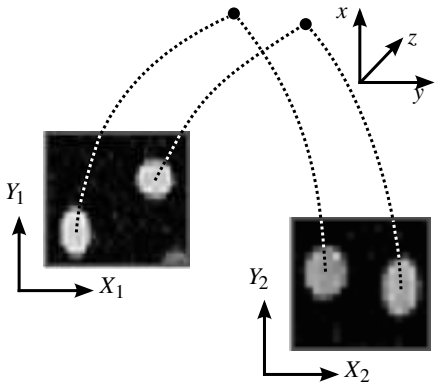

Figure 3.13: From the sensor locations $\boldsymbol{X}_1 = (X_1, Y_1)$ and $\boldsymbol{X}_2 = (X_2, Y_2)$ of the corresponding particle images, the particle locations, $\boldsymbol{x} = (x, y, z)$, are determined using third order polynomial mapping functions (capital letters denote image/sensor coordinates; lowercase letters denote physical coordinates).

in physical space: $\boldsymbol{x} = (x, y, z)$. Altogether the polynomials have 35 coefficients for every spatial coordinate, yielding the following equation for the x coordinate:

$$x = \sum_{i,j,k,l} c_{i,j,k,l}\, X_1^i\, Y_1^j\, X_2^k\, Y_2^l, \quad i+j+k+l \leq 3 \tag{3.6}$$

where $c_{i,j,k,l}$ denotes the coefficients. For the y and the z coordinates, the polynomial function is formulated accordingly. Before the determination of the particle locations by means of coordinate mapping, the coefficients of the polynomials have to be calculated from the calibration points, derived from the pinhole matrix.

A n×35 matrix, S, is established, where n denotes the number of processed pinhole images. Typically, at every z position of the calibration target (50-100 positions along the z axis), 400 pinholes are analyzed, so that n lies in the range of 20000 to 40000. The 35 entries represent the right side of Eq. (3.6), where X_1, Y_1, X_2, and Y_2 are the sensor coordinates of the pinhole images of the nth pinhole. The 35 coefficients $\mathbf{c}$ are estimated by solving the following set of equations in the least squares sense (in this particular case, the coefficients $\mathbf{c}_x$ for the x coordinate)

$$\left(S^{\mathrm{T}} S\right) \boldsymbol{c}_x = S^{\mathrm{T}} \boldsymbol{x} \tag{3.7}$$

where $\boldsymbol{x}$ is an n×1 vector containing the x locations of n pinholes (the coefficients $\boldsymbol{c}_y$ and $\boldsymbol{c}_z$ are determined accordingly).

It was outlined before that APTV is used for an initial estimation of the particle locations on both cameras. This is necessary in order to match corresponding particle images, since

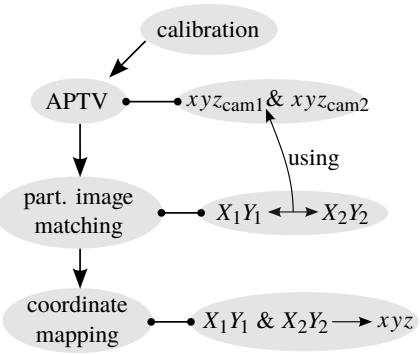

Figure 3.14: Particle location scheme using stereoscopic APTV. Single camera APTV gives an initial estimate of the particle locations for both cameras. Thus, particle images are matched using the location information with a search radius in space. Particles are then located more accurately employing the stereoscopic view.

the stereoscopic imaging system does not have this capability. The matching procedure establishes small search radii around the spatial particle locations to find intersecting and therefore matching particles, imaged by the two cameras. With the known particle intersections the corresponding particle images are determined. After the matching procedure, to locate the particles, again a $n\times35$ matrix, S, is set up. Now S contains the sensor locations $\boldsymbol{X}_1$ and $\boldsymbol{X}_2$ of n imaged particles in the measurement volume. With the knowledge of the coefficients, $\boldsymbol{c}$, the particles locations are determined by

$$\boldsymbol{x} = S\boldsymbol{c}_x \tag{3.8}$$

where $\boldsymbol{x}$ is a $n\times1$ vector containing the x location of the particles. The y and z locations are calculated accordingly. Figure 3.14 gives an overview of the outlined stereo APTV particle location scheme.

3.3.3 Measurement uncertainty

To prove the feasibility of stereo APTV for accurate three-dimensional particle location, a comprehensive accuracy analysis is introduced. In a first analysis, the pinhole locations are reconstructed using the stereo APTV processing algorithms. These estimated locations are then compared to the known locations of the pinholes, leading to the deviations $\Delta\mathbf{x}$ in a $40\times40\times25$ mm^3 measurement volume. From these deviations, the location determination

uncertainty

$$E = \sqrt{\frac{\sum_{i=1}^{n} \Delta \mathbf{x}^2}{n-1}} \tag{3.9}$$

is calculated at every z position of the pinhole matrix for the three spatial coordinates. The error E decreases slightly with distance to the camera for all coordinates, as shown in Fig. 3.15. The error, E_x, of the x coordinate yields values between 0.0025 and 0.005 mm, while E_z lies between 0.005 and 0.015 mm, showing the largest uncertainty for the z coordinate. This is due to the fact that the measurements were conducted at an angle of $\beta = 30°$ ($\beta < 90°$: $E_x < E_z$; $\beta = 90°$: $E_x = E_z$; $\beta > 90°$: $E_x > E_z$;). Consequently, $E_y = 0.0025$ mm is the smallest, since the cameras are aligned at an angle of 0° with respect to the y axis.

In addition to the pinhole location uncertainty analysis, the particle displacement determination uncertainty was determined for a 40×40×20 mm^3 measurement volume in air. This was performed by means of the measurement of a "motionless" flow, using standard DEHS particles with a diameter of around 1 µm. These particles were imaged in a glass tank at two instances, which were separated in time by 0.5 µs. Since there was no driven flow in the glass tank, the displacement of the particles between the light pulses approaches zero. However, processing the particle images, a non-zero displacement is likely estimated. This results from external influences, such as misalignments of the laser light volume illumination, image noise, and light reflections. The particle displacement determination uncertainty, σ, is calculated like E in Eq. (3.9), only that here, $\Delta \mathbf{x}$ is the displacement of a particle between the two light pulses. For the x coordinate, the uncertainty yields $\sigma_x = 0.012$ mm, while $\sigma_z = 0.025$ mm (the measurements were conducted at $\beta = 30°$). Again, the error of the y coordinate is the lowest with 0.005 mm. However, assuming a maximum particle image displacement of 10 pixels between the two frames, these uncertainties yield velocity errors in the range of 1−3 % for u, v, and w, relative to the maximum flow velocity, for every single particle track. Note, that the latter analysis provides a true measure of the stereo APTV uncertainty, since the experiments were conducted under realistic measurement conditions, i.e. same cameras, lasers, seeding particles, etc., except that the light pulses had a small separation in time.

It has to be noted that astigmatic 3D-PTV does increase the particle image density compared to regular 3D-PTV, since the elliptical particle images are significantly larger and therefore yield an increasing number of particle image overlaps. However, the measurement depth can be increased, as the matching of corresponding particle images is done with the help of the initial particle location estimation, resolving ambiguities.

3.4 3D-PTV using a tomographic predictor

So far, the outlined three-dimensional measurement approaches targeted on applications, where optical techniques have not been used extensively, due to the measurement en-

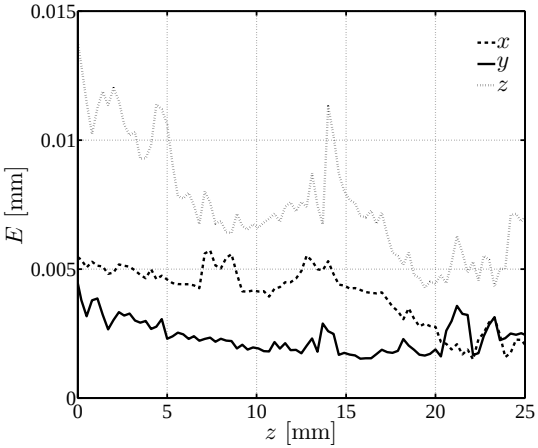

Figure 3.15: Error of the pinhole location reconstruction calculated at every pinhole matrix z position. For the y coordinate the location error is the lowest, while the z uncertainty is the highest (measurement volume size: 40×40×25 mm^3).

vironment. This tomographic 3D-PTV approach combines the well-known techniques tomographic reconstruction and 3D-PTV to measure densely seeded flows yielding high spatial resolution, a good optical access provided.

For the understanding of complex flows, but also for the efficient measurement at multiple locations, it is desirable to gain quantitative volumetric flow information. Tomographic PIV has become a powerful tool to capture volumetric flow fields Elsinga et al. (2006). The method has been widely applied to measure flows at high seeding concentrations. To achieve a good spatial resolution, high seeding concentrations are required, such that it is possible to capture small flow structures as well. However, in tomographic PIV the cross-correlation of the reconstructed measurement volume leads to a spatial averaging of the velocity data. Flows with strong velocity gradients, such as boundary layer flows, shear flows, wake flows, and jet flows, are biased due to this averaging (Kähler et al. (2012a)). PTV provides a means to overcome this drawback, since it tracks individual particles without using correlation volumes. Instead, sub-voxel/sub-pixel accuracy can be achieved. Employing the tomographic reconstruction, a straightforward approach is to determine the spatial particle locations by means of a 3D Gaussian fit of the voxel intensities, and to track these particle locations, as applied by Schröder et al. (2011). However, Elsinga & Tokgoz (2014) showed that with an increasing seeding concentration, a larger number of ghost particles appears in the reconstruction, which can only be eliminated thoroughly using a time-series of data.

In many fluid mechanical applications, though, it is not feasible to obtain time-resolved flow data. Reasons for this are limitations in the recording rate of the cameras and in the repetition rate of the lasers. To account for these drawbacks, the combined tomographic 3D-PTV approach offers the possibility of double-frame particle tracking at larger particle image densities than current 3D-PTV methods. The tomographic reconstruction is used to predict the sensor locations of the particle images on the different sensors and to identify non-corresponding particle image sets. Then, the spatial particle locations are triangulated from corresponding sets of particle images. A stand-alone use of the triangulation approach, known as 3D-PTV, would only work for very low particle images densities, due to ambiguous particle image correspondences. The detailed procedure of the combined tomographic 3D-PTV processing scheme is outlined in the following. It is applied to a synthetic and an experimental data set.

3.4.1 Principle

The first step of the processing scheme is the tomographic reconstruction. Both, the multiplicative algebraic reconstruction technique (MART) and the multiplicative line-of-sight (MLOS) reconstruction are suitable, while at larger particle image densities the MART algorithm is favorable, as will be outlined later. The reconstructed volumes are binarized using an intensity threshold, following the estimation of the spatial particle locations, $\boldsymbol{x} = (x, y, z)$, from their center of mass. Thus, it is not necessary to store the reconstructed volumes, since the information on the spatial particle locations is sufficient for the further processing steps. With the help of the camera matrices, P_i, the particle coordinates $\boldsymbol{x}$ are then mapped back to camera sensors by simple multiplication

$$\boldsymbol{X}_i = P_i \boldsymbol{x} \tag{3.10}$$

where $\boldsymbol{X}_i = (X_i, Y_i)$ denotes the predicted location of the originating particle image on camera sensor i (red crosses in Fig. 3.16). Now these predicted particle image locations need to be associated with actual particle images, which have to be detected first. To find the actual particle image locations, a 2D Gaussian fit with an adaptive kernel size is applied to the preprocessed recordings (red circles in Fig. 3.16). This is followed by matching the fitted particle image locations with the predicted sensor locations from the tomographic reconstruction. If a particle image is associated with multiple reconstructed particle locations it is rejected entirely and not considered for triangulation anymore (see case 2 in Fig. 3.16). Thus, the tomographic reconstruction also serves as a validator to identify non-corresponding sets of particle images. Triangulating a non-corresponding set of particles images would yield a non-existent particle location, a ghost particle. In the context of tomographic reconstruction, the term ghost particle refers to a reconstructed intensity peak in the volume, also originating from non-corresponding particle images.

To perform the triangulation for the particle location determination, it is necessary to find uniquely matching particle images on at least two sensors. If this is the case, the spatial particle location is determined by means of the so-called optimal triangulation

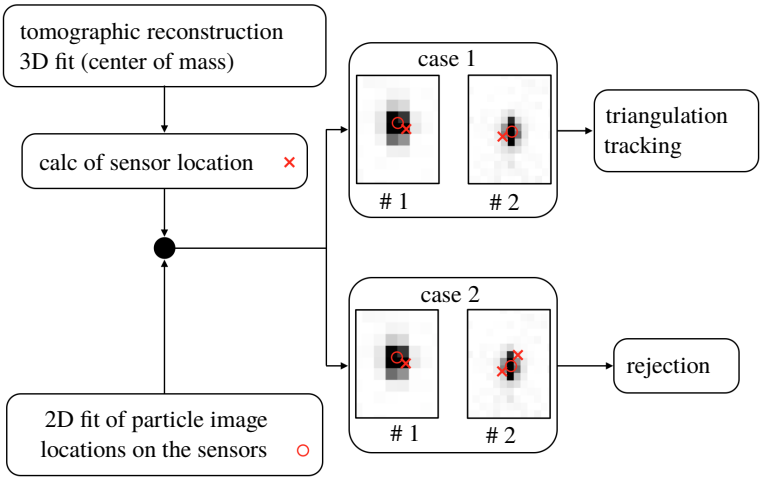

Figure 3.16: Principle of combined tomographic 3D-PTV. The tomographic reconstruction is used the predict the sensor locations of corresponding particle images and to detect ambiguities. Case 1 shows a unique particle image correspondence. In case 2 an ambiguity is shown, where a particle image is associated with two spatial particle coordinates.

method Hartley & Sturm (1997). It is essential to avoid the appearance of ghost particles, since they cause a systematic underestimation of velocity gradients for cross-correlation as well as tracking methods, as shown by Elsinga et al. (2011) and Elsinga & Tokgoz (2014).

The final step of the processing procedure is to apply a tracking algorithm to derive the velocity field. However, to eliminate remaining ghost particles as thoroughly as possible, a probabilistic tracking procedure is used, which takes the motion of surrounding particles into account Cierpka et al. (2013). At this point it is emphasized that the tracking step is an important part of the proposed processing procedure, since it is a powerful tool to minimize the number of remaining outliers.

3.4.2 Synthetic data set

To assess the performance of the combined tomographic 3D-PTV approach, two synthetic data sets, with different particle per pixel values, N_{ppp}, are processed according to the outlined procedure. The sets are generated using the *DaVis 8* software from *LaVision*, where the locations of the true particles are well-known. Set A has a volume size of

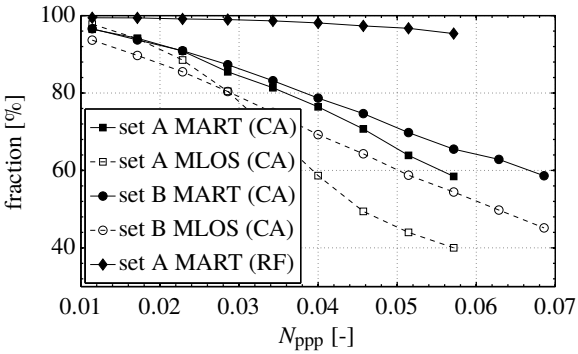

Figure 3.17: The fraction of correctly estimated particle locations, i.e. they are located within one voxel radius from the true particle locations (CA = combined tomographic 3D-PTV; RF = reference data)

800×800×300 voxel^3 and set B has a volume size of 800×800×50 voxel^3. The synthetic illumination has a Gaussian profile going down to e^{-1} at the edges of the volume. The synthetic particle images have an intensity of $I = 512 \pm 100$ counts and a diameter of $D = 2 \pm 0.5$ pixel.

A 3D Gaussian fit of the reconstructed volume, using MART, of set A serves as reference data, labeled as RF. Figure 3.17 provides an overview of the correct reconstructions, i.e. the fraction of estimated particle locations that lie within a distance of 1 voxel in space compared to the true particle locations. With increasing N_{ppp}, the fraction of correct reconstructions decreases for the combined tomographic 3D-PTV approach, labeled CA, while the thinner volume (set B), denoted by circles, yields higher values than the thicker volume (set A), denoted by squares. This is due to the larger number of ghost particles in the reconstructed thicker volume, since the lines of sight travel along a larger distance within the measurement volume, increasing the probability of intersections with other lines of sights from the different views. The correct reconstructions drop below 60 % at higher N_{ppp} values. The amount of correct reconstructions is also dependent on the tomographic reconstruction method used for the prediction. A MART prediction, as denoted by the filled markers and the solid lines, yields more correct reconstructions than a MLOS predictor, as denoted by the hollow markers and the dashed lines. Again, the reason for this difference is the larger share of ghost particles in the MLOS reconstruction, favoring ambiguities in the particle image matching. However, for the reference data, denoted by diamonds, the fraction of correct reconstructions stays on a high level, yielding values above 95%.

Since it is the goal of the outlined 3D particle imaging approach to reliably derive

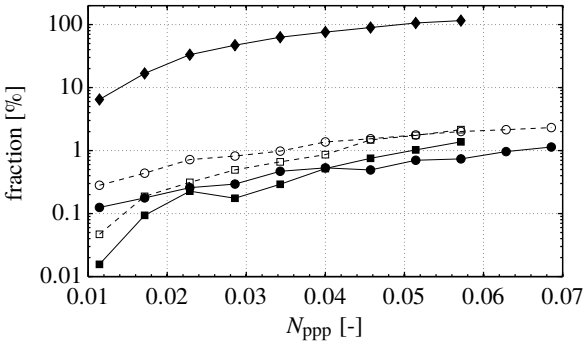

Figure 3.18: The fraction of ghost particles compared to the number of true particles (CA = combined tomographic 3D-PTV; RF = reference data)

velocity fields from double-frame recordings, the number of ghost particles has to be limited to a minimum. Figure 3.18 gives an overview of the fraction of ghosts, relative to the number of true particles. The reference data, i.e. a 3D Gaussian fit of the tomographic reconstruction of set A, yields a ghost particle percentage of larger than 100% for larger N_{ppp} values. Without a time-series of data, this large amount of ghost particles does not allow for an accurate particle tracking. However, when utilizing the tomographic reconstruction as a predictor for the combined approach, the percentage of ghost particles is decreased significantly, such that it yields below 1.5% for the MART reconstruction predictor, even at larger N_{ppp} values. The amount of ghost particles is larger for the MLOS predictor, namely up to 2.5% at $N_{ppp} \approx 0.07$. Along with sophisticated tracking and outlier detection algorithms, this small share of ghost particles allows for reliable and accurate flow field estimations from double-frame recordings.

Attaining large particle image densities is a major goal for particle imaging techniques, since a high spatial resolution and a high measurement efficiency is desired. However, one must bear in mind that increasing particle image densities yield more overlapping particle images, raising the uncertainty in estimating the displacement vector. This is illustrated in Fig. 3.19, where the uncertainty of the spatial particle location, i.e. the standard deviation, $\sigma_{\Delta \boldsymbol{x}}$, of the absolute voxel distance of the estimated from the true particle locations, is shown. With increasing N_{ppp} the uncertainty rises from values between $\sigma_{\Delta \boldsymbol{x}} = 0.1$–$0.2$ to $\sigma_{\Delta \boldsymbol{x}} > 0.4$ voxel at $N_{ppp} > 0.06$. Altogether, these values are in good agreement with a previous study by Wieneke (2013).

It is obvious that not all particles can be used for the flow velocity estimation using the combined tomographic 3D-PTV approach, as illustrated by the fraction of correct

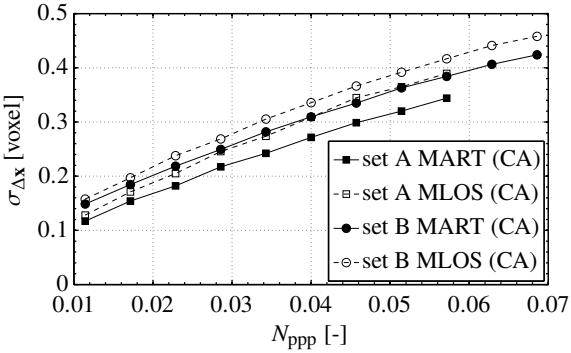

Figure 3.19: Uncertainty of the spatial particle location determination

reconstructions in Fig. 3.17. Therefore, Fig. 3.20 shows the effective particle per pixel values, $N_{ppp,eff}$, denoting the actual amount of particles that contribute to the velocity estimation. Using the MART predictor, values of $N_{ppp,eff} \approx 0.04$ can be reached for the thin volume, while for the thicker volume values yield up to $N_{ppp,eff} \approx 0.033$. The performance of the MLOS predictor is lower, yielding $N_{ppp,eff} \approx 0.031$ for the thin volume and $N_{ppp,eff} \approx 0.024$ for the thicker volume. At some point a maximum $N_{ppp,eff}$ is reached, where an increasing fraction of ghost particles does not allow for a reliable prediction anymore. Consequently, thicker volumes and less sophisticated reconstruction techniques lower $N_{ppp,eff}$.

3.5 Measurement of turbulent boundary layer flow

To prove the feasibility of the combined tomographic 3D-PTV approach for the measurement of real flows, it is applied for estimating the near-wall flow profile in an adverse pressure gradient region of a turbulent boundary layer experiment, which is introduced in detail in Reuther et al. (2015).

This study focuses on the feasibility of a near-wall 3D flow measurements, specifically if a double-frame tracking approach is also capable of resolving the flow field accurately. To assess the feasibility, this time-resolved data set is processed with a time-resolved tracking and a double-frame tracking approach, to compare the results.

3.5.1 Experimental set-up

The experimental set-up comprised four *PCO dimax* high speed cameras, each equipped with a 50 mm *Zeiss* macro objective lens and a 2× teleconverter, as illustrated in Fig.

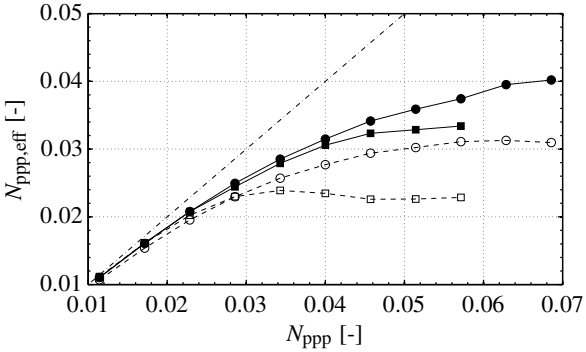

Figure 3.20: Effective amount of particles per pixel

3.5.1. The measurement volume, yielding a size of 8×5×2.5 mm^3, was illuminated using a *Quantronix* high speed laser in forward scattering configuration. A volume self-calibration procedure was applied to the recordings, see Wieneke (2008). In total, 30000 images in 3 subsets were recorded at a frequency of 10.2 kHz. With $N_{ppp} < 0.01$ a MLOS predictor was sufficient for the combined approach.

3.5.2 Flow fields – comparison between time-resolved and double-frame tracking

The availability of a time-series of recordings allows for comparing double-frame particle tracking (DF-PTV) with time-resolved particle tracking (TR-PTV). Figure 3.22 shows the averaged and binned near-wall velocity profile at a free stream velocity of $U_\infty \approx 10$ m/s, where the first velocity value is located 0.01 mm from the wall. The friction velocity yields $u_\tau \approx 0.2004$ m/s. For the mean flow profile, using the combined approach (CA), a good agreement between DF-PTV and TR-PTV is achieved. A reference (RF) DF-PTV analysis, limited to values with a maximum distance of 1.5 mm from the wall, of a 3D Gaussian fit of the reconstructed volumes, using MART, yields some deviations from the TR-PTV (CA) solution. The velocity is slightly underestimated due to the ghost particles, as observed by Elsinga & Tokgoz (2014). However, with the small particles per pixel value the fraction of ghost particles is rather low, such that the deviations are not very significant. With larger N_{ppp} values the deviations are supposed to increase.

The mean flow profile does not necessarily reveal if a method is suitable for accurate measurements. Therefore, Fig. 3.23 provides the measured Reynolds stresses for the combined approach, again comparing TR-PTV and DF-PTV. In the region close to the wall, i.e. $y^+ < 2$, the DF-PTV data has the strongest relative deviations from the TR-PTV

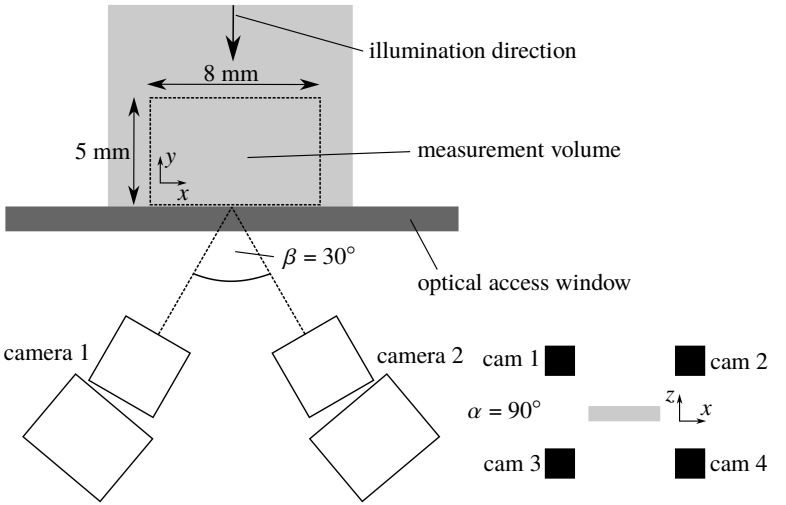

Figure 3.21: Schematic of the experimental set-up for the turbulent boundary layer measurement

data. Generally, the DF-PTV data overestimates the Reynolds stresses, while staying in a reasonable distance from the TR-PTV data. The span-wise component $\overline{ww}/u_\tau^2$ shows slightly larger deviations.

Altogether, the measurement results indicate that it is also possible to derive accurate flow fields, when only a double-frame data sets is available. Therefore, using the combined tomographic 3D-PTV, volumetric particle tracking at large flow velocities with good spatial resolution is enabled.

3.6 Concluding remarks

In this chapter, multi-camera volumetric flow velocimetry approaches were introduced. They are significantly more complex than single camera approaches in terms of processing and experimental set-up and require a larger optical access due to viewing the measurement domain from different angles. However, they offer a better measurement accuracy especially for the particle z location and the velocity w in that direction. For small measurement depths, 3D-PTV allows for accurate flow measurements with only two cameras, as it was proven by a comprehensive uncertainty analysis and the measurement of a Tesla turbine rotor flow. When the measurement depth increases, more ambiguities in

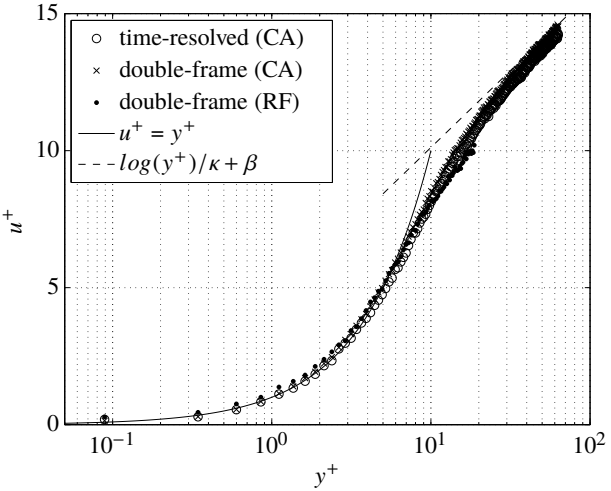

Figure 3.22: Mean flow velocities, binned in wall-normal direction with a bin width of 0.02 mm. Following constants are used: $\kappa = 0.41$ and $\beta = 5.0$.

the particle image matching arise. To overcome this problem, astigmatic imaging can be employed to estimate the particle location with a subsequent more accurate triangulation.

If the measurement environment allows it, i.e. when the optical access is large enough and vibrations are small, a combined tomographic 3D-PTV approach is feasible. This technique is capable of accurately measuring flows with strong velocity gradients from double-frame data sets with particle per pixel values up to $N_{\mathrm{ppp}} = 0.04$. Compared to time-resolved algorithms, the combined approach can measure flows at high flow velocities and in larger volumes.

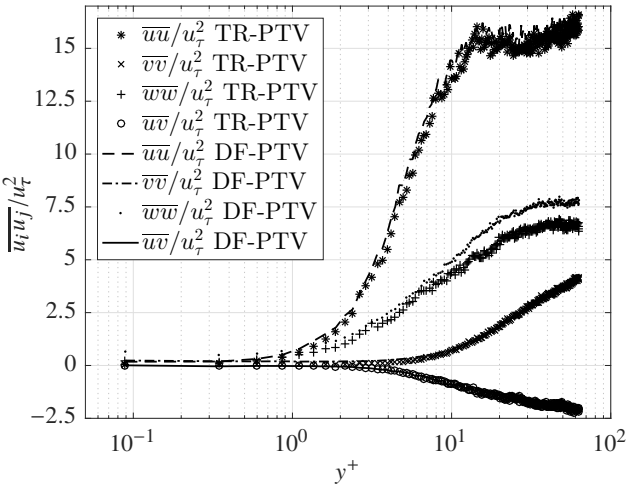

Figure 3.23: Reynolds stresses, binned in wall-normal direction with a bin width of 0.02 mm for the combined approach (TR-PTV = time-resolved PTV; DF-PTV = double-frame PTV).

4 Conclusion and Outlook

Volumetric particle imaging techniques can contribute to a better understanding of complex flows. Furthermore, some applications require a 3D measurement technique, since the flow features might be smaller than the light sheet thickness. In particular, particle tracking approaches can resolve flows with strong velocity gradients.

Nowadays, a variety of 3D velocimetry techniques is available, offering a broad spectrum of applications. Single camera approaches allow for measurements in environments, where the optical access is limited and vibrations occur, at relatively low costs. Among these approaches, astigmatism particle tracking velocimetry (APTV) has proven to yield spatial resolutions along the optical axis, which are significantly better than typical light sheet thicknesses, at measurement depths of up to 50 mm. In APTV, astigmatic aberrations cause the particle images to shape ellipses on the camera sensor, where the particle depth location is coded in the ratio of the vertical and horizontal axis length of its particle image. A continuous adjustment of the measurement depth is achieved by changing the position of the cylindrical lens, inducing the astigmatism, in front of the objective lens relative to the camera sensor. Due to offering a measurement uncertainty of the in-plane components of below 2%, relative to the maximum flow velocity, in conjunction with the insensitivity to vibrations and seeding density fluctuations, APTV certainly broadens the range of applications for volumetric velocimetry approaches. This is especially the case for fields like turbomachinery, combustion, and engine research, where particle imaging have not been applied to a great extent.

However, in the latter fields of application, some of the measurement domains of interest are not only difficult to access, but their dimensions can also be rather small. Likely it is not possible to fit a calibration target in these domains, when the upper and lower boundary of the measurement volume have a distance of only a few millimeters or less. For these kinds of domain, an *in situ* calibrated defocusing PTV approach is a powerful tool for flow measurements, when a linear change of the particle image diameter along the z direction is provided. In this approach, first the particle image displacements are determined by means of a tracking algorithm, yielding a distribution of the displacement over the particle image diameter. At the walls, the displacements are supposed to yield zero, such that a particle image diameter for the upper and lower wall can be determined by means of linear fit. Then the particle depth location can be simply scaled from its particle image diameter and the well-known distance of the boundaries of the measurement domain. This defocusing approach has a measurement uncertainty of less than 2.4%, relative to the maximum flow velocity, and is therefore capable of resolving strong velocity gradients in depth direction.

Altogether, the single camera approaches with their unique capabilities nicely complement the more complex multi-camera approaches. While employing more equipment and more extensive processing procedures, multiple views of the measurement volume yields a higher accuracy particle location determination, especially in z direction. Therefore, if the optical access allows for it, a multi-camera method can yield improved measurement uncertainties and also higher seeding concentrations compared to single camera approaches.

The 3D-PTV imaging concept is based on epipolar geometry and triangulation to estimate the spatial particle locations from at least two views. In a stereoscopic set-up, 3D-PTV is suitable to measure flows in domains with small measurement depths. Only then, correct particle image pairs on both sensor can be detected reliably, since the search area for corresponding particle images on the second sensor increases with the measurement depth, such that more possible matches appear. Once a corresponding particle image pair is found, the particle location can be triangulated from their sensor locations with high accuracy. Using 3D-PTV, the velocity can be determined with an uncertainty of less than 1.25%, relative to the maximum flow velocity, in a volume with a depth of 1 mm.

In practice, 3D-PTV was applied for the measurement of the flow in a Tesla turbine rotor at a gap height of only 0.5 mm. The flow field was measured for laminar and turbulent cases, and in each case showed a good resolution in depth direction, also at RPMs of up to 5000 1/min. For this Tesla turbine measurement, a non-intrusive calibration procedure was applied, where the calibration points were derived from light reflections of a continuous wave laser on the measurement volume boundaries.

If a larger measurement depth is required, the stereoscopic technique can be combined with astigmatic imaging. The APTV algorithms give an initial estimation of the spatial particle locations, such that corresponding particle images can be matched by this spatial location. In a second step, the triangulation can be performed to yield a better accuracy in the particle location determination.

Following the idea of using astigmatic imaging to match particle images on different sensors, a tomographic reconstruction can be used as a predictor as well. Such a combined tomographic 3D-PTV set-up consists of a minimum of four cameras, requiring a large optical access and only minor vibrations in the test facility to avoid camera misalignments. However, this approach can yield high particle image densities, up to $N_{\mathrm{ppp}} = 0.039$ for a large measurement volume depth and up to $N_{\mathrm{ppp}} = 0.045$ for a fat light sheet set-up. In this approach, the particle locations of the initial tomographic reconstruction are estimated by means of a center of mass fit. From the spatial locations, the originating sensor locations are calculated, which are then compared to the particle images detected on each camera sensor. If a predicted particle image location matches uniquely with a detected particle image on a least two sensors, the spatial particle location is triangulated from the corresponding particle images. Otherwise, a detected particle image can be associated with more than one predicted location, which gives rise to the assumption that at least one of the predicted locations results from a ghost particle or an overlapping particle image. This particle image is then rejected and not considered for triangulation.

Consequently, the combined tomographic 3D-PTV approach is highly effective in avoiding ghost particles, which is essential, since in a final step a tracking algorithm is applied to the data to determine the velocity from double-frame data. Without the availability of a time-series of data, it is not possible to distinguish ghost particles from true particles, if the fraction of ghost particles is large. The feasibility of the technique to resolve strong velocity gradients was proven by the measurement of a turbulent boundary layer flow, where the velocity profile could be measured close to the wall ($y^+ < 1$ at $Re_\theta > 3000$).

It is clear that there is still a large potential, which can be utilized to improve volumetric flow measurement techniques. Not only in terms of the measurement uncertainty, but also in terms of the processing performance, for instance by using parallel computing or graphics processing units. Concerning user friendliness, graphical user interfaces are a key to open processing techniques to more users.

A specific improvement or extension for the stereoscopic 3D-PTV technique could be a single-camera set-up, where the two different views can be achieved via a mirror system, such that the sensor is divided in two halves with different perspectives. Such a set-up is less affected by camera misalignments due to vibrations, since the mounts of camera and mirrors can be much more rigid. For the combined tomographic 3D-PTV approach, a subsequent standard 3D-PTV procedure of the images can be performed, since then the particle image density is much lower, without the initially matched particle images. With this procedure the effective particle image density can even be increased and more information can be derived from the recorded data. Besides the possibility of estimating particle tracks, the APTV concept can also be employed to track bubbles in a volume, which could be a nice and useful extension of the method. Furthermore, APTV allows for multi-physics measurements by employing functional particles. Additional measurable quantities include temperature, pressure, and potential of hydrogen (pH), which certainly opens further fields of application. The use of functional particles in a multi-camera set-up is normally not feasible due to the strong dependency of their light emission behavior on viewing as well as illumination angle.

LIST OF REFERENCES

Atkinson C, Coudert S, Foucaut JM, Stanislas M & Soria J (**2010**). *The accuracy of tomographic particle image velocimetry for measurements of a turbulent boundary layer*. Experiments in Fluids 50:1031–1056, DOI: 10.1007/s00348-010-1004-z

Barnhart DH, Adrian RJ & Papen GC (**1994**). *Phase-conjugate holographic system for high-resolution particle-image velocimetry*. Appl Opt 33:7159–7170, DOI: 10.1364/AO.33.007159

Born M & Wolf E (**1997**). Principles of optics: electromagnetic theory of propagation, interference and diffraction of light, 6th edn. Cambridge University Press, Cambridge

Buchmann NA, Atkinson C, Jeremy MC & Soria J (**2011**). *Tomographic particle image velocimetry investigation of the flow in a modeled human carotid artery bifurcation*. Experiments in Fluids 50:1131–1151, DOI: 10.1007/s00348-011-1042-1

Buchmann NA, Cierpka C, Kähler CJ & Soria J (**2014**). *Ultra-high-speed 3D astigmatic particle tracking velocimetry: application to particle-laden supersonic impinging jets*. Experiments in Fluids 55:1842, DOI: 10.1007/s00348-014-1842-1

Chang TP, Wilcox NA & Tatterson GB (**1984**). *Application Of Image Processing To The Analysis Of Three-Dimensional Flow Fields*. Optical Engineering 23:283, DOI: 10.1117/12.7973279

Chen S, Angarita-Jaimes N, Angarita-Jaimes D, Pelc B, Greenaway AH, Towers CE, Lin D & Towers DP (**2009**). *Wavefront sensing for three-component three-dimensional flow velocimetry in microfluidics*. Experiments in Fluids 47:849–863, DOI: 10.1007/s00348-009-0737-z

Cierpka C & Kähler CJ (**2012**). *Particle imaging techniques for volumetric three-component (3D3C) velocity measurements in microfluidics*. Journal of Visualization 15:1–31, DOI: 10.1007/s12650-011-0107-9

Cierpka C, Segura R, Hain R & Kähler CJ (**2010**). *A simple single camera 3C3D velocity measurement technique without errors due to depth of correlation and spatial averaging for microfluidics*. Measurement Science and Technology 21:045401, DOI: 10.1088/0957-0233/21/4/045401

Cierpka C, Lütke B & Kähler CJ (**2013**). *Higher order multi-frame particle tracking velocimetry*. Experiments in Fluids 54:1533, DOI: 10.1007/s00348-013-1533-3

Elsinga GE & Tokgoz S (**2014**). *Ghost hunting – an assessment of ghost particle detection and removal methods for tomographic-PIV*. Measurement Science and Technology 25:084004, DOI: 10.1088/0957-0233/25/8/084004

Elsinga GE, Scarano F, Wieneke B & Oudheusden BW (**2006**). *Tomographic particle image velocimetry*. Experiments in Fluids 41:933–947, DOI: 10.1007/s00348-006-0212-z

Elsinga GE, Westerweel J, Scarano F & Novara M (**2011**). *On the velocity of ghost particles and the bias errors in Tomographic-PIV*. Experiments in Fluids 50:825–838, DOI: 10.1007/s00348-010-0930-0

Fuchs T, Hain R & Kähler CJ (**2013**). *Astigmatism Particle Tracking Velocimetry for Macroscopic Flows*. In: 10th International Symposium on Particle Image Velocimetry, Delft, The Netherlands, July 1-3

Fuchs T, Hain R & Kähler CJ (**2014**a). *Macroscopic three-dimensional particle location using stereoscopic imaging and astigmatic aberrations*. Optics Letters 39:6863–6866, DOI: 10.1364/OL.39.006863

Fuchs T, Hain R & Kähler CJ (**2014**b). *Three-dimensional location of micrometer-sized particles in macroscopic domains using astigmatic aberrations*. Optics Letters 39:1298–1301, DOI: 10.1364/OL.39.001298

Fuchs T, Heinold M, Hain R & Kähler CJ (**2014**c). *Stereoscopic Astigmatism Particle Tracking Velocimetry for macroscopic 3D3C flow measurements in air*. In: 17th International Symposium on Applications of Laser Techniques to Fluid Mechanics Lisbon, Portugal, 07-10 July

Fuchs T, Hain R & Kähler CJ (**2015**). *Three-dimensional single-camera PTV air flow measurements in cavities using in-situ calibration - comparison with tomographic PTV*. In: 11th International Symposium on Particle Image Velocimetry, Santa Barbara, USA, September 14-16

Fuchs T, Hain R & Kähler CJ (**2016**a). *A three-dimensional velocimetry approach using a combination of tomographic reconstruction and triangulation for double-frame particle tracking*. In: 18th International Symposium on the Application of Laser and Imaging Techniques to Fluid Mechanics, Lisbon, Portugal, 04-07 July

Fuchs T, Hain R & Kähler CJ (**2016**b). *Double-frame 3D-PTV using a tomographic predictor*. Experiments in Fluids 57:174, DOI: 10.1007/s00348-016-2247-0

Fuchs T, Hain R & Kähler CJ (**2016**c). *In situ calibrated defocusing PTV for wall-bounded measurement volumes*. Measurement Science and Technology 27:084005, DOI: 10.1088/0957-0233/27/8/084005

Fuchs T, Hain R & Kähler CJ (**2016**d). *Uncertainty quantification of three-dimensional velocimetry techniques for small measurement depths*. Experiments in Fluids 57:73, DOI: 10.1007/s00348-016-2161-5

Grothe RL & Dabiri D (**2008**). *An improved three-dimensional characterization of defocusing digital particle image velocimetry (DDPIV) based on a new imaging volume definition*. Measurement Science and Technology 19:065402, DOI: 10.1088/0957-0233/19/6/065402

Guha A & Sengupta S (**2014**). *The fluid dynamics of work transfer in the non-uniform viscous rotating flow within a Tesla disc turbomachine*. Physics of Fluids 26:033601, DOI: 10.1063/1.4866263

Hain R & Kähler CJ (**2006**). *3D3C Time-Resolved Measurements with a Single Camera Using Optial Aberrations*. In: 13th International Symposium on Applications of Laser Techniques to Fluid Mechanics, Lisbon, Portugal, 26-29 June, Lisbon

Hain R, Kähler CJ & Michaelis D (**2008**). *Tomographic and time resolved PIV measurements on a finite cylinder mounted on a flat plate*. Experiments in Fluids 45:715–724, DOI: 10.1007/s00348-008-0553-x

Hartley R & Zisserman A (**2004**). Multiple view geometry in computer vision, 2nd edn. Cambridge University Press, Cambridge

Hartley RI & Sturm P (**1997**). *Triangulation*. Computer Vision and Image Understanding 68:146–157, DOI: 10.1006/cviu.1997.0547

Herman GT & Lent A (**1976**). *Iterative reconstruction algorithms*. Computers in Biology and Medicine 6:273–294, DOI: 10.1016/0010-4825(76)90066-4

Hinsch KD (**2002**). *Holographic particle image velocimetry*. Measurement Science and Technology 13:R61–R72, DOI: 10.1088/0957-0233/13/7/201

Hwang TG, Doh DH & Okamoto K (**2005**). *4D-PTV Measurements of an impinged jet with a dynamic 3D-PTV*. Journal of Visualization 8:245–252, DOI: 10.1007/BF03181502

Kähler CJ, Sammler B & Kompenhans J (**2002**). *Generation and control of tracer particles for optical flow investigations in air*. Experiments in Fluids 33:736–742, DOI: 10.1007/s00348-002-0492-x

Kähler CJ, Scharnowski S & Cierpka C (**2012**a). *On the resolution limit of digital particle image velocimetry*. Experiments in Fluids 52:1629–1639, DOI: 10.1007/s00348-012-1280-x

Kähler CJ, Scharnowski S & Cierpka C (**2012**b). *On the uncertainty of digital PIV and PTV near walls*. Experiments in Fluids 52:1641–1656, DOI: 10.1007/s00348-012-1307-3

Kajitani L & Dabiri D (**2005**). *A full three-dimensional characterization of defocusing digital particle image velocimetry*. Measurement Science and Technology 16:790–804, DOI: 10.1088/0957-0233/16/3/022

Kao HP & Verkman AS (**1994**). *Tracking of single fluorescent particles in three dimensions: use of cylindrical optics to encode particle position*. Biophysical Journal 67:1291–1300, DOI: 10.1016/S0006-3495(94)80601-0

Karnitz MA, Potter MC & Smith MC (**1974**). *An Experimental Investigation of Transition of a Plane Poiseuille Flow*. Journal of Fluids Engineering 96:384, DOI: 10.1115/1.3447174

Katz J & Sheng J (**2010**). *Applications of Holography in Fluid Mechanics and Particle Dynamics*. Annual Review of Fluid Mechanics 42:531–555, DOI: 10.1146/annurev-fluid-121108-145508

Kieft RN, Schreel KRAM, van der Plas GAJ & Rindt CCM (**2002**). *The application of a 3D PTV algorithm to a mixed convection flow*. Experiments in Fluids 33:603–611, DOI: 10.1007/s00348-002-0513-9

Klinner J & Willert C (**2012**). *Tomographic shadowgraphy for three-dimensional reconstruction of instantaneous spray distributions*. Experiments in Fluids 53:531–543, DOI: 10.1007/s00348-012-1308-2

Kühn M, Ehrenfried K, Bosbach J & Wagner C (**2010**). *Large-scale tomographic particle image velocimetry using helium-filled soap bubbles*. Experiments in Fluids 50:929–948, DOI: 10.1007/s00348-010-0947-4

Kumar A, Cierpka C, Williams SJ, Kähler CJ & Wereley ST (**2010**). *3D3C velocimetry measurements of an electrothermal microvortex using wavefront deformation PTV and a single camera*. Microfluidics and Nanofluidics 10:355–365, DOI: 10.1007/s10404-010-0674-4

Lemma E, Deam R, Toncich D & Collins R (**2008**). *Characterisation of a small viscous flow turbine*. Experimental Thermal and Fluid Science 33:96–105, DOI: 10.1016/j.expthermflusci.2008.07.009

Lin D, Angarita-Jaimes NC, Chen S, Greenaway AH, Towers CE & Towers DP (**2008**). *Three-dimensional particle imaging by defocusing method with an annular aperture*. Optics Letters 33:905, DOI: 10.1364/OL.33.000905

Liu Z, Speetjens MFM, Frijns AJH & van Steenhoven AA (**2013**). *Application of astigmatism μ-PTV to analyze the vortex structure of AC electroosmotic flows*. Microfluidics and Nanofluidics 16:553–569, DOI: 10.1007/s10404-013-1253-2

Longuet-Higgins HC (**1981**). *A computer algorithm for reconstructing a scene from two projections*. Nature 293:133–135, DOI: 10.1038/293133a0

Lüthi B, Tsinober A & Kinzelbach W (**2005**). *Lagrangian measurement of vorticity dynamics in turbulent flow*. Journal of Fluid Mechanics 528:87–118, DOI: 10.1017/S0022112004003283

Lynch KP & Scarano F (**2013**). *A high-order time-accurate interrogation method for time-resolved PIV*. Measurement Science and Technology 24:035305, DOI: 10.1088/0957-0233/24/3/035305

Lynch KP & Scarano F (**2015**). *An efficient and accurate approach to MTE-MART for time-resolved tomographic PIV*. Experiments in Fluids 56:66, DOI: 10.1007/s00348-015-1934-6

Maas H, Gruen A & Papantoniou D (**1993**). *Particle tracking velocimetry in three-dimensional flows*. Experiments in Fluids 15:133–146, DOI: 10.1007/BF00190953

Malik N, Dracos T & Papantoniou D (**1993**). *Particle tracking velocimetry in three-dimensional flows*. Experiments in Fluids 15:279–294, DOI: 10.1007/BF00223406

Marin A, Liepelt R, Rossi M & Kähler CJ (**2015**). *Surfactant-driven flow transitions in evaporating droplets*. Soft Matter 12:1593–1600, DOI: 10.1039/C5SM02354H

Meng H, Pan G, Pu Y & Woodward SH (**2004**). *Holographic particle image velocimetry: from film to digital recording*. Measurement Science and Technology 15:673–685, DOI: 10.1088/0957-0233/15/4/009

Muller PB, Rossi M, Marin AG, Barnkob R, Augustsson P, Laurell T, Kähler CJ & Bruus H (**2013**). *Ultrasound-induced acoustophoretic motion of microparticles in three dimensions*. Physical Review E 88:23006

Murata S & Kawamura M (**1999**). *Particle depth measurement based on depth-from-defocus*. Optics & Laser Technology 31:95–102, DOI: 10.1016/S0030-3992(99)00027-4

Nienhuis K & Nijboer B (**1949**). *The diffraction theory of optical aberrations: Part III: General formulae for small aberrations; experimental verification of the theoretical results*. Physica 14:590–608, DOI: 10.1016/0031-8914(49)90002-6

Nijboer B (**1943**). *The diffraction theory of optical aberrations: Part I: General discussion of the geometrical aberrations*. Physica 10:679–692, DOI: 10.1016/S0031-8914(43)80016-1

Nijboer B (**1947**). *The diffraction theory of optical aberrations: Part II: Diffraction pattern in the presence of small aberrations*. Physica 13:605–620, DOI: 10.1016/0031-8914(47)90052-9

Nishino K, Kasagi N & Hirata M (**1989**). *Three-Dimensional Particle Tracking Velocimetry Based on Automated Digital Image Processing*. Journal of Fluids Engineering 111:384, DOI: 10.1115/1.3243657

Nishioka M, A SI & Ichikawa Y (**1975**). *An experimental investigation of the stability of plane Poiseuille flow*. Journal of Fluid Mechanics 72:731–751

Novara M & Scarano F (**2012**). *Performances of motion tracking enhanced Tomo-PIV on turbulent shear flows.* Experiments in Fluidsluids 52:1027–1041, DOI: 10.1007/s00348-011-1187-y

Novara M & Scarano F (**2013**). *A particle-tracking approach for accurate material derivative measurements with tomographic PIV*. Experiments in Fluids 54:1584, DOI: 10.1007/s00348-013-1584-5

Novara M, Batenburg KJ & Scarano F (**2010**). *Motion tracking-enhanced MART for tomographic PIV*. Measurement Science and Technology 21:035401, DOI: 10.1088/0957-0233/21/3/035401

Novara M, Schanz D, Reuther N, Kähler CJ & Schröder A (**2016**). *Lagrangian 3D particle tracking in high-speed flows: Shake-The-Box for multi-pulse systems*. Experiments in Fluids 57:128, DOI: 10.1007/s00348-016-2216-7

Ohmi K & Li HY (**2000**). *Particle-tracking velocimetry with new algorithms*. Measurement Science and Technology 11:603–616, DOI: 10.1088/0957-0233/11/6/303

Pereira F & Gharib M (**2002**). *Defocusing digital particle image velocimetry and the three-dimensional characterization of two-phase flows*. Measurement Science and Technology 13:683–694, DOI: 10.1088/0957-0233/13/5/305

Pereira F, Gharib M, Dabiri D & Modarress D (**2000**). *Defocusing digital particle image velocimetry: a 3-component 3-dimensional DPIV measurement technique. Application to bubbly flows*. Experiments in Fluids 29:S078–S084, DOI: 10.1007/s003480070010

Pereira F, Lu J, Castaño-Graff E & Gharib M (**2007**). *Microscale 3D flow mapping with μDDPIV*. Experiments in Fluids 42:589–599, DOI: 10.1007/s00348-007-0267-5

Piirto M, Eloranta H, Saarenrinne P & Karvinen R (**2005**). *A comparative study of five different PIV interrogation algorithms*. Experiments in Fluids 39:573–590, DOI: 10.1007/s00348-005-0992-6

Prandtl L (**1936**). *Entstehung von Wirbeln bei Wasserströmungen - 1. Entstehung von Wirbeln und künstliche Beeinflussung der Wirbelbildung*. Film, Institut für wissenschaftlichen Film (IWF) Göttingen

Pu Y & Meng H (**2000**). *An advanced off-axis holographic particle image velocimetry (HPIV) system*. Experiments in Fluids 29:184–197, DOI: 10.1007/s003489900088

Pu Y, Song X & Meng H (**2000**). *Off-axis holographic particle image velocimetry for diagnosing particulate flows*. Experiments in Fluids 29:117–128, DOI: 10.1007/s003480070014

Rafati S & Ghaemi S (**2016**). *Evaluation of high magnification two and three dimensional particle image tracking/velocimetry in near wall turbulence*. In: 18th International Symposium on the Application of Laser and Imaging Techniques to Fluid Mechanics Lisbon, Portugal, 04-07 July

Raffel M, Willert CE, Wereley ST & Kompenhans J (**2007**). Particle Image Velocimetry, 2nd edn. Springer, Berlin & Heidelberg, DOI: 10.1007/978-3-540-73528-1

Rallabandi B, Marin A, Rossi M, Kähler C & Hilgenfeldt S (**2015**). *Three-dimensional streaming flow in confined geometries*. Journal of Fluid Mechanics 777:408–429, DOI: DOI:10.1017/jfm.2015.336

Reuther N, Scharnowski S, Hain R, Schanz D, Schröder A & Kähler CJ (**2015**). *Experimental investigation of adverse pressure gradient turbulent boundary layers by means of large-scale PIV*. In: 11th International Symposium on Particle Image Velocimetry, Santa Barbara, USA, September 14-16

Rochlitz H, Scholz P & Fuchs T (**2015**). *The flow field in a high aspect ratio cooling duct with and without one heated wall*. Experiments in Fluids 56:208, DOI: 10.1007/s00348-015-2071-y

Romanin VD & Carey VP (**2011**). *An integral perturbation model of flow and momentum transport in rotating microchannels with smooth or microstructured wall surfaces*. Physics of Fluids 23:082003, DOI: 10.1063/1.3624599

Rossi M & Kähler CJ (**2014**). *Optimization of astigmatic particle tracking velocimeters*. Experiments in Fluids 55:1809, DOI: 10.1007/s00348-014-1809-2

Scarano F (**2013**). *Tomographic PIV: principles and practice*. Measurement Science and Technology 24:012001, DOI: 10.1088/0957-0233/24/1/012001

Schanz D, Gesemann S, Schröder A, Wieneke B & Novara M (**2013**). *Non-uniform optical transfer functions in particle imaging: calibration and application to tomographic reconstruction*. Measurement Science and Technology 24:024009, DOI: 10.1088/0957-0233/24/2/024009

Schanz D, Gesemann S & Schröder A (**2016**). *Shake-The-Box: Lagrangian particle tracking at high particle image densities*. Experiments in Fluids 57:70, DOI: 10.1007/s00348-016-2157-1

Schnars U & Jüptner W (**1994**). *Direct recording of holograms by a CCD target and numerical reconstruction.* Applied Optics 33:179–181, DOI: 10.1364/AO.33.000179

Schosser C (**2016**). *Experimental and numerical investigations and optimisation of Tesla-radial Turbines*. PhD thesis, Universtität der Bundeswehr München

Schosser C, Lecheler S & Pfitzner M (**2014**). *A Test rig for the investigation of the performance and flow field of Tesla friction turbines*. In: Proceedings of the ASME Turbo Expo, Düsseldorf, Germany, June 16-20

Schosser C, Fuchs T, Hain R & Kähler CJ (**2016**a). *Non-intrusive calibration for three-dimensional particle imaging*. Experiments in Fluids 57:69, DOI: 10.1007/s00348-016-2167-z

Schosser C, Fuchs T, Hain R, Lecheler S & Kähler CJ (**2016**b). *Three-dimensional particle tracking velocimetry in a Tesla turbine rotor using a non-intrusive calibration method*. In: 18th International Symposium on the Application of Laser and Imaging Techniques to Fluid Mechanics, Lisbon, Portugal, 04-07 July

Schröder A, Geisler R, Elsinga GE, Scarano F & Dierksheide U (**2007**). *Investigation of a turbulent spot and a tripped turbulent boundary layer flow using time-resolved tomographic PIV*. Experiments in Fluids 44:305–316, DOI: 10.1007/s00348-007-0403-2

Schröder A, Geisler R, Staack K, Elsinga GE, Scarano F, Wieneke B, Henning A, Poelma C & Westerweel J (**2011**). *Eulerian and Lagrangian views of a turbulent*

boundary layer flow using time-resolved tomographic PIV. Experiments in Fluids 50:1071–1091, DOI: 10.1007/s00348-010-1014-x

Schröder A, Schanz D, Michaelis D, Cierpka C, Scharnowski S & Kähler CJ (**2015**). *Advances of PIV and 4D-PTV "Shake-The-Box" for Turbulent Flow Analysis – the Flow over Periodic Hills*. Flow Turbulence and Combustion 95:193–209, DOI: 10.1007/s10494-015-9616-2

Segura R (**2015**). *Thermo-Liquid Crystal (TLC) Thermography and Astigmatism Particle Tracking Velocimetry (APTV) for the simultaneous time-resolved 3D measurements of microscopic temperature and velocity flow fields*. Phd thesis, Universität der Bundeswehr München

Segura R, Rossi M, Cierpka C & Kähler CJ (**2015**). *Simultaneous three-dimensional temperature and velocity field measurements using astigmatic imaging of non-encapsulated thermo-liquid crystal (TLC) particles.* Lab on a chip 15:660–663, DOI: 10.1039/c4lc01268b

Sheu YH, Chang T, Tatterson G & Dickey D (**1982**). *A three-dimensional measurement technique for turbulent flows*. Chemical Engineering Communications 17:67–83, DOI: 10.1080/00986448208911615

Soloff SM, Adrian RJ & Liu ZC (**1997**). *Distortion compensation for generalized stereoscopic particle image velocimetry*. Measurement Science and Technology 8:1441–1454, DOI: 10.1088/0957-0233/8/12/008

Spille JH, Kaminski T, Königshoven HP & Kubitscheck U (**2012**). *Dynamic three-dimensional tracking of single fluorescent nanoparticles deep inside living tissue*. Optics Express 20:19697–707, DOI: 10.1364/OE.20.019697

Stolz W & Köhler J (**1994**). *In-plane determination of 3D-velocity vectors using particle tracking anemometry (PTA)*. Experiments in Fluids 17:105–109, DOI: 10.1007/BF02412811

Suzuki Y & Kasagi N (**2000**). *Turbulent Air-Flow Measurement with the Aid of 3-D Particle Tracking Velocimetry in a Curved Square Bend*. Flow Turbulence and Combustion 63:415–442, DOI: 10.1023/A:1009936304219

Tien WH, Kartes P, Yamasaki T & Dabiri D (**2008**). *A color-coded backlighted defocusing digital particle image velocimetry system*. Experiments in Fluids 44:1015–1026, DOI: 10.1007/s00348-007-0457-1

Tien WH, Dabiri D & Hove JR (**2014**). *Color-coded three-dimensional micro particle tracking velocimetry and application to micro backward-facing step flows*. Experiments in Fluids 55:1684, DOI: 10.1007/s00348-014-1684-x

Towers CE, Towers DP, Campbell HI, Zhang S & Greenaway AH (**2006**). *Three-dimensional particle imaging by wavefront sensing*. Optics Letters 31:1220, DOI: 10.1364/OL.31.001220

Tsai R (**1987**). *A versatile camera calibration technique for high-accuracy 3D machine vision metrology using off-the-shelf TV cameras and lenses*. IEEE Journal on Robotics and Automation 3:323–344

Van Kampen N (**1949**). *An asymptotic treatment of diffraction problems*. Physica 14:575–589, DOI: 10.1016/0031-8914(49)90001-4

Van Kampen N (**1950**). *An asymptotic treatment of diffraction problems. II*. Physica 16:817–821, DOI: 10.1016/0031-8914(50)90090-5

Wieneke B (**2008**). *Volume self-calibration for 3D particle image velocimetry*. Experiments in Fluids 45:549–556, DOI: 10.1007/s00348-008-0521-5

Wieneke B (**2013**). *Iterative reconstruction of volumetric particle distribution*. Measurement Science and Technology 24:024008, DOI: 10.1088/0957-0233/24/2/024008

Willert C (**1997**). *Stereoscopic digital particle image velocimetry for application in wind tunnel flows*. Measurement Science and Technology 8:1465–1479, DOI: 10.1088/0957-0233/8/12/010

Willert C & Gharib M (**1992**). *Three-dimensional particle imaging with a single camera*. Experiments in Fluids 12:353–358, DOI: 10.1007/BF00193880

Willert C & Kompenhans J (**2010**). *PIV Analysis of Ludwig Prandtl's Historic Flow Visualization Films*. In: 63rd Annual Meeting of the APS Division of Fluid Dynamics, November 21-23, Long Beach, USA

Yoon SY & Kim KC (**2006**). *3D particle position and 3D velocity field measurement in a microvolume via the defocusing concept*. Measurement Science and Technology 17:2897–2905, DOI: 10.1088/0957-0233/17/11/006